Study of nitrogen-enriched niobium and its influence on the performance on superconducting RF cavities

Dissertation

zur Erlangung des Doktorgrades
des Department Physik
der Universität Hamburg

vorgelegt von

Christopher Bate

aus Hamburg

Hamburg
2022

Gutachter/innen der Dissertation:	Prof. Dr. Brian Foster Dr. Hans Weise
Zusammensetzung der Prüfungskommission:	Prof. Dr. Brian Foster Dr. Hans Weise Prof. Dr. Daniela Pfannkuche Prof. Dr. Andreas Stierle Prof. Dr. Gudrid Moortgat-Pick
Vorsitzende/r der Prüfungskommission:	Prof. Dr. Daniela Pfannkuche
Datum der Disputation:	21.02.2022
Vorsitzender Fach-Promotionsausschusses PHYSIK:	Prof. Dr. Wolfgang Hansen
Leiter des Fachbereichs PHYSIK:	Prof. Dr. Günter H. W. Sigl
Dekan der Fakultät MIN:	Prof. Dr. Heinrich Graener

Eidesstattliche Versicherung / Declaration on oath

Hiermit versichere ich an Eides statt, die vorliegende Dissertationsschrift selbst verfasst und keine anderen als die angegebenen Hilfsmittel und Quellen benutzt zu haben.

Hamburg, den 09.03.2022 _____

Unterschrift

Abstract

The structure and composition of niobium, the current state-of-the-art material for superconducting radio-frequency (SRF) cavities, are of extreme importance in understanding the operation behaviour of cavities. In recent years, the use of nitrogen to improve this behaviour has been widely studied. However, the effects of nitrogen treatments on the niobium surface are still not fully understood. The new surface process called "nitrogen Infusion" produces a boost in performance of up to twice the Q_0 at 2 K for cavities with accelerating fields of > 35 MV/m compared to those treated in the standard way. Such nitrogen-treated cavities can also reach > 45 MV/m. In order to obtain an overview of the nitrogen infusion mechanism, it is necessary to reproduce the nitrogen recipe successfully. Various studies have been conducted in order to develop effective and efficient methods for nitrogen infusion. The goal of this thesis is to find a stable recipe for a successful nitrogen-infusion treatment and understand the underlying mechanisms. This work focused on the study of fine-grain niobium and large-grain niobium samples and involves the improvement of an existing ceramic-sample furnace. Various surface-sensitive techniques were utilized in order to obtain valuable information on the formation of new phases, as well as the behaviour of different RF parameters. Residual-resistivity-ratio (RRR) values on nitrogen-infusion samples with various parameters have shown new insights. Secondary-ion mass spectrometry (SIMS) on samples indicates that the grain boundaries play a vital role in the nitrogen infusion process. The conditions under which niobium carbides are formed have been studied in order to determine the particle line-of-sight protection necessary for successful nitrogen-infusion treatment. Superconducting quantum-interference devices (SQUIDs) are sensitive to many Niobium surface properties, especially those important in understanding nitrogen infusion. Utilizing a SQUID the surface nucleation field on nitrogen-infused samples has been measured.

Zusammenfassung

Die Struktur und Zusammensetzung von Niob, dem derzeit erfolgreichsten Material für supraleitende Hochfrequenz(SRF)-Kavitäten, sind von größter Bedeutung, um deren Auswirkungen im realen Betrieb zu verstehen. In den letzten Jahren wurde die Verwendung von Stickstoff auf dem Gebiet der thermischen Behandlung von SRF-Kavitäten umfassend untersucht. Die Auswirkungen von Stickstoffbehandlungen auf die Niob-Oberfläche waren jedoch noch nicht vollständig verstanden. Das neue Oberflächenverfahren namens "nitrogen Infusion" erzeugt eine Leistungssteigerung bis zum doppelten für Q_0 bei 2 K im Vergleich zu standardbehandelten Kavitäten mit Beschleunigungsfeldern von über $>$ 35 MV/m. Auch die Rekrod-Wert-Beschleunigungsfelder $>$ 45 MV/m werden erreicht. Um einen Überblick über den Stickstoffinfusionsmechanismus zu erhalten, ist es notwendig, die Stickstoffrezeptur stabil nachzubilden. Es wurden verschiedene Studien zur Stickstoffinfusion durchgeführt, um effektive und effiziente Methoden für dieses Verfahren zu entwickeln. Das Ziel dieser Arbeit war es, ein stabiles Rezept für eine erfolgreiche Stickstoffinfusionsbehandlung zu finden und die zugrunde liegenden Mechanismen zu verstehen. Diese Arbeit konzentrierte sich auf die Untersuchung von feinkörnigen Niob- und großkörnigen Niob-Proben und beinhaltet die Verbesserung eines bestehenden keramischen Probenofens. Um wertvolle Informationen über die Bildung neuer Phasen sowie das Verhalten verschiedener HF-Parameter zu erhalten, wurden verschiedene oberflächensensitive Techniken eingesetzt. Die Werte des Restwiderstandsverhältnisses (RRR) bei Stickstoffinfusionsproben mit verschiedenen Parametern haben neue Erkenntnisse erbracht. Ergebnisse der Sekundärionen-Massenspektrometrie (SIMS) an Proben zeigen, dass die Korngrenzen eine entscheidende Rolle im Stickstoffinfusionsprozess spielen. Die Bedingungen, unter denen Niobcarbide gebildet werden, wurden im Zusammenhang mit Abdeckungen gegen Teilchen, welche im Sichtfeld zur Kavitäten Innenoberfläche stehen untersucht. Es wurde herausgefunden, das für eine erfolgreiche Stickstoffinfusionsbehandlung eine Vermeidung von Niobcarbiden erforderlich ist. Supraleitende Quanteninterferenzeinheiten (SQUIDs) reagieren empfindlich auf viele Niob-Oberflächeneigenschaften, insbesondere auf diejenigen, die für das Verständnis der Stickstoffinfusion wichtig sind. Messungen an stickstoff infusionierten Proben wurden an einem SQUID durchgeführt.

Contents

1 SRF cavities and the demand for high gradients

1.1 Introduction

Electromagnetic cavities have now been operated for decades in many accelerators with a range of applications, such as high-energy particle physics, low-energy to medium-energy nuclear physics and free-electron lasers. They enable further progress and discoveries in a broad range of fields such as solid-state physics and material science. The power loss due to Joule heating on a cavity wall increases with the square of the accelerating voltage, which makes copper cavities not suitable for high-power long-pulse or continuous-wave (cw) operation. Accelerators in cw operation benefit from increased luminosity in the case of colliders or brilliance for light sources. The superconducting material niobium is currently the best choice for cavity performance. Superconducting cavities have an immense advantage for cw or long-pulse operation with high radiofrequency (RF) duty factors. The surface resistance of superconducting cavities is several orders of magnitude smaller than that of copper. SRF cavities also have large accelerating gradients (E_{acc}) [1]. X-ray free-electron lasers, such as the European X-ray Free-Electron Laser (European XFEL), the Linac Coherent Light Source (LCLS) II or Shanghai High repetition rate XFEL and Extreme light facility (SHINE) would benefit from even lower surface resistance (R_s) at higher gradient fields, since fewer cavities would be required to achieve a given energy. Furthermore, the lower R_s would mean less power dissipation in the cavity walls, translating into less generated heat, thus saving cryogenic costs.
The International Linear Collider (ILC) [2] has the potential to discover new physics beyond the Standard Model and improve our understanding of the universe's fundamental building blocks. Its size and hence high cost has raised various challenges in the design and construction of the facility. The key components of superconducting machines are niobium cavities. In the European XFEL, around 800 niobium cavities were installed in the accelerator's 3.4 km-long section [3]. In the ILC, as a Higgs Factory which is expected to be around 8 kilometers long, the installation of over 16,000 niobium cavities is planned [2] [4]. A new cavity treatment that increases the quality factor and accelerating gradient of niobium cavities at frequencies of 1.3 GHz was presented in 2017 [5]. This process, entitled Nitrogen Infusion, produces quality factors of $2 \cdot 10^{10}$ at accelerating gradients of $40 - 45$ MV/m for single-cell cavities [5] and $1.5 \cdot 10^{10}$ at 37 MV/m for nine-cell cavities [6]. The treated cavities display a better performance compared to traditional preparations, such as the European XFEL recipe [7], without the need to remove material from the surface. With the increasing number of projects using to Niobium technology, the ambition to improve performance is at an all-time high. However, a fundamental understanding of nitrogen infusion is still missing. In addition to nitrogen, the distribution of oxygen and carbon within the RF layer is believed to be a crucial factor in determining the performance of Nb cavities. The reproducibility of the nitrogen infusion treatment is low. This is mainly due to the various uncertainties involved in the process. Various laboratories around the world were engaged in collaborations to reproduce the nitrogen-infusion treatment, but this has not yet been achieved [8].
This chapter introduces the reader to superconducting radio-frequency cavities. It begins by explaining how they were invented, then moves on to describe the cavity physics and the possibilities they offer for particle acceleration.

1.2 Birth of RF cavities

The very first accelerators were nothing more than electrostatic capacitors. They were limited in achievable energy by the breakdown voltage of the material. Overcoming this effect was possible by using alternating-fields as proposed by Ising [9]. Based on this idea the first RF linear accelerator was constructed by the Norwegian physicist Rolf Wideröe [10]. Drift tubes were connected to a RF source. The tubes are alternately connected to the poles producing a AC voltage between the tubes as shown in Fig. 1. During the time in which particles travel from one gap between tubes to the next, the RF source polarity changes, so that particles in the gaps always see an accelerating field. The insides of the tubes are shielded from the fields as they act like Faraday cages. The conducting tubes have to be-

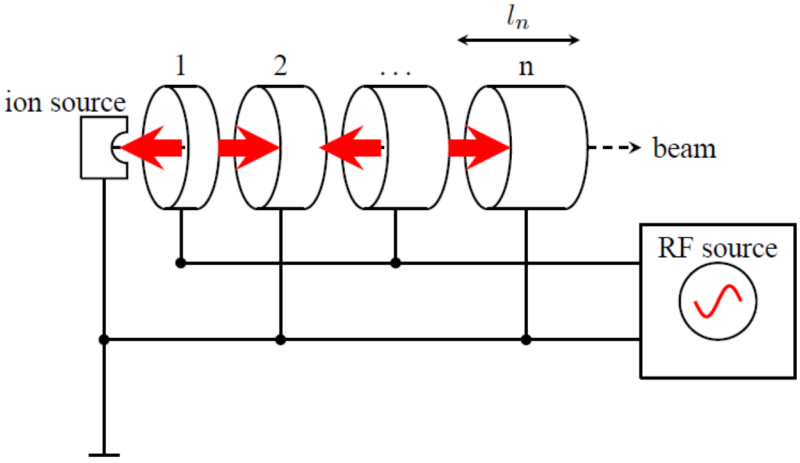

Figure 1: Schematic construction of a RF linear accelerator according to Rolf Wideröe (taken from [11]). The red arrows point in the electric field direction between the tubes. While the particles travel from one gap to the next, the RF phase of the electric field varies by π, so that particles always see an accelerating field in the gaps. Provided that the length of the tubes l_n and the rf frequency f has been adjusted correctly according to $l_n = v/(2f)$ with the particle velocity v.

come longer with increasing particle velocity (synchronicity condition). For a RF frequency f, the length of the n'th tube is given by $l_n = v/(2f)$, where v is the particle velocity. The Wideröe linac was therefore limited by the drift tubes becoming unfeasible long. A Wideröe accelerator that was built in 1931 in Berkeley by Lawrence was 1.2 m long and had 30 drift tubes [12]. It accelerated mercury ions to 1.26 MeV with a 7 MHz RF source at a voltage of 42 kV. The Wideröe linac is suitable for particle velocities up to 5% of speed of light i.e. an energy of 1.2 MeV for protons and 640 eV for electrons [13]. Already at these velocities and the then available frequencies, the drift tubes had to be several meters long. Using higher frequency means more RF energy was radiated as the structure was not electromagnetically shielded and the drift tubes acted as antennas, making the acceleration very inefficient for higher energies. A solution was to put the linac into a conducting cylinder as a resonator proposed by Louis Alvarez in 1946 [14]. By putting the Wideröe linac into a conducting tube as shown in Fig. 2, the first RF cavity was created. The field between the gaps of the Alvarez linac points in the same direction, in contrast to the fields in a Wideröe linac. The

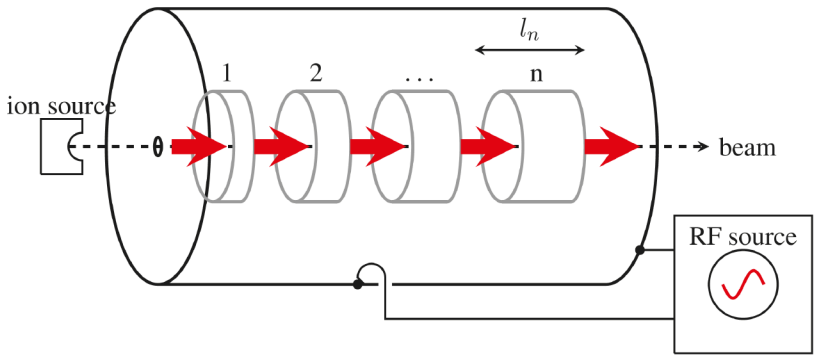

Figure 2: Schematic construction of a so called Alvarez drift tube linac (taken from [11]). It is basically an Wideröe linac shielded by an conducting cylinder. The red arrows point in the field direction between the tubes. Different from the Wideröe linac they point in the same direction

Alvarez structure is based on a so-called "pillbox" resonant cavity operating at the lowest resonance, where the E-field is uniform along the cavity axis [11]. For relativistic particles, meaning velocities close to the speed of light (referred to $\beta > 0.99$ with $v = \beta c$), it is no longer necessary to adapt the RF frequency as particles gain energy rather than velocity, nor does the tube length need to change. These conditions are already fulfilled for energies above 1 MeV in electron accelerators and above several GeV in proton accelerators.
A cavity can be represented by a capacitance and an inductor in one circuit as shown in Fig. 3. Having a capacitance in parallel to an inductor creates a resonator with a resonant

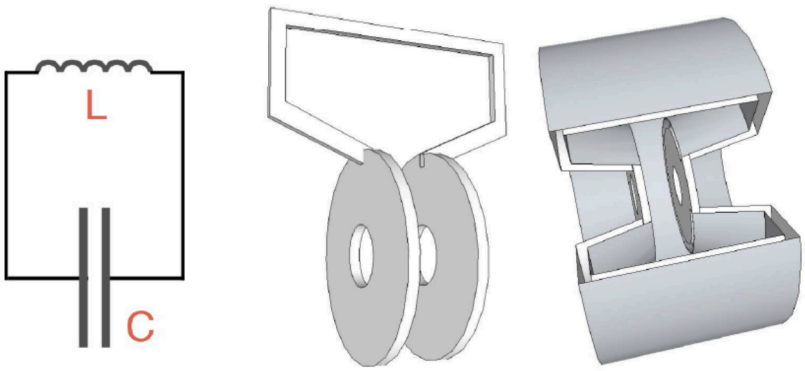

Figure 3: Cavity representation as an LC circuit [11].

frequency $w_0 = 1/\sqrt{LC}$. The simplest cavity design would be an empty cylinder with a conducting surface, also called a pillbox cavity. The electromagnetic fields can be induced in the cavity either as travelling or standing waves. For traveling waves, electromagnetic waves are fed by a power coupler at one side of the cavity. The waves travel trough the cavity in phase with the particles, transferring energy while the wave is decaying. This induces a large energy spread in the particle bunch. On the other hand, a standing wave is obtained by closing the resonator system, building up a standing wave pattern by multiple reflections. Due to the additional boundary condition in the longitudinal direction, certain

electromagnetic modes are restricted. For standing waves, the so called TM_{010}-mode is fed into the cavity, where TM stands for transverse magnetic. The TM_{010}-mode is the simplest one; its field pattern for a 9-cell TESLA type cavity is illustrated in Fig. 4. Only certain

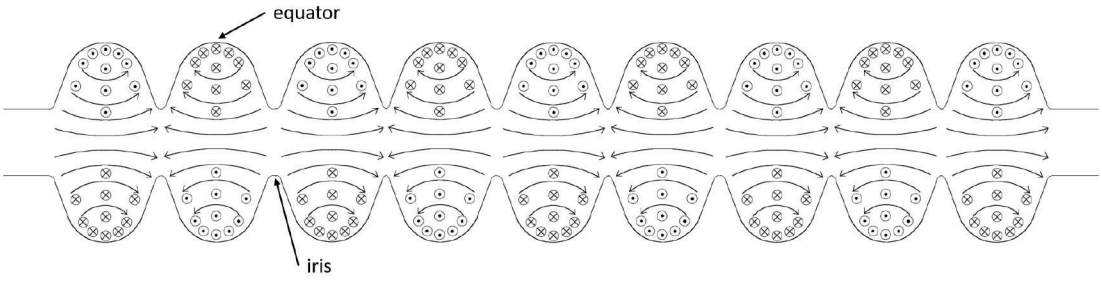

Figure 4: Schematic view of the electric and magnetic field in a 9-Cell TESLA-shaped cavity [15]. The electric-field component is excited parallel to the particle direction while the magnetic field is transverse to the beam axis. The magnetic field has its strongest contribution at the equators where the electric field is the weakest. Thus the overall surface resistance is dominated by the magnetic field component by inducing currents on the cavity inner surface.

'loss-free' modes (for perfect conducting walls) can exist in the cavity. Any RF power that is filled at frequencies other than the loss-free excited modes will be damped exponentially. Travelling-wave structures need a total filling time in the sub-microsecond range. Building up a standing-wave pattern on the other hand takes from 10 s to microseconds; superconducting cavities are in the millisecond range. Travelling-wave structures are more power efficient for applications requiring very short beam pulses (< 1 μs); such cavities are able to achieve high accelerating gradients (≈ 100 MeV/m) also with normal-conducting copper cavities but only for very short pulses. Normal conducting cavities are mostly made of copper and water cooled to reduce electrical surface resistance from dissipated heat due to induced currents from the rf field. However, the anomalous skin effect [16] leads to the resistance eventually plateauing, leading to inefficiency since much energy is dissipated as heat rather than in accelerating particles. A way to overcome this effect is to use a superconducting material, which has practically zero surface resistance. The idea to use superconducting materials for RF cavities was already proposed in 1961 [17]. For a long time there has been research into the further development of the shape and treatment of such cavities. Making use of elliptical superconducting RF cavities based on bulk niobium such as the so-called TESLA type as shown in Fig. 4 delivered a step towards higher accelerating gradients and is nowadays one of the most common accelerator technologies.
An electron gains maximal possible energy from the cavity if, in terms of the phase of the rf field, it is located where the electrical field reaches its maximum value. The accelerating gradient E_{acc} is defined by means of this energy gain as

$$E_{acc} = \frac{1}{L}\int_{-L/2}^{L/2} E(z)cos(\omega z/v)dz, \tag{1}$$

while L depicts the length of the cavity, $E(z)$ is the electrical field along coordinate z of the beam axis, ω is the frequency of the rf field and v is the particle velocity. Looking at

the field distribution inside a single-cell cavity as shown in Fig. 5 shows that the electric field has its maximum at the inner surface of the iris of the cavity, E_{peak}. Accordingly the magnetic peak surface field, B_{peak}, builds up along the equator surface. The elliptically

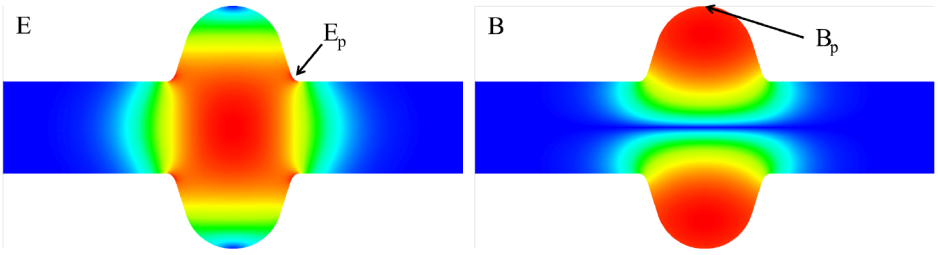

(a) Electric field distribution. The electric field is maximal at the iris inner surface of the cavity.

(b) Magnetic field distribution. The magnetic field is maximal at the equator inner surface of the cavity.

Figure 5: CST simulation of the electric and magnetic field distribution for a TESLA type single cell cavity.

shaped superconducting TESLA cavities are designed to have low ratios of E_{peak}/E_{acc} and B_{peak}/E_{acc}, which both depend on the geometry of the cavity. It should be noted that a compromise had to be made, since a lower B_{peak}/E_{acc} comes at the expense of a higher E_{peak}/E_{acc} if for example cell-cell coupling is taken into account [18]. High E_{peak} values are disadvantageous in terms of field emission and voltage breakdown, which will be explained in more detail below. The peak magnetic field, B_{peak}, sets a limit for the maximal achievable E_{acc}.

Charged particles produce an electromagnetic wake as they pass through the cavity, exciting eigenmodes of higher frequencies. Such beam-induced higher-order modes perturb the next incoming particles, which can influence beam stability and cause power dissipation [1]. To remove these unwanted perturbations, special higher-order-mode (HOM) couplers are attached to the cavity. A cavity consisting of several cells has to be treated as a coupled resonator, where the number of cells corresponds to the number of passband modes (eigenfrequencies) and is operated in the so called π-mode. In this mode, electromagnetic fields in neighboring cells oscillate in opposite phase, as shown in Fig. 4. A single-cell cavity is a resonator with a certain frequency and thus can only be fed by rf signals with a frequency within its passband mode. The number of available passband modes is proportional to the number of cells in a coupled resonator. The passband modes for a 9-cell cavity are therefore noted as $x/9$ π where $x/9$ refers to the phase advance of the standing wave between neighboring cells. The corresponding field amplitudes of the passband modes are shown in Fig. 6. From the distributions it is clear that the π-mode is the one that will accelerate particles the most.

Current transport in superconductors is loss-free in static fields. For RF fields, however, the wall currents sustaining the fields dissipate energy. A parameter that serves as a figure of merit for cavity performance is the quality factor:

$$Q_0 = \frac{\omega_0 U}{P_c},$$

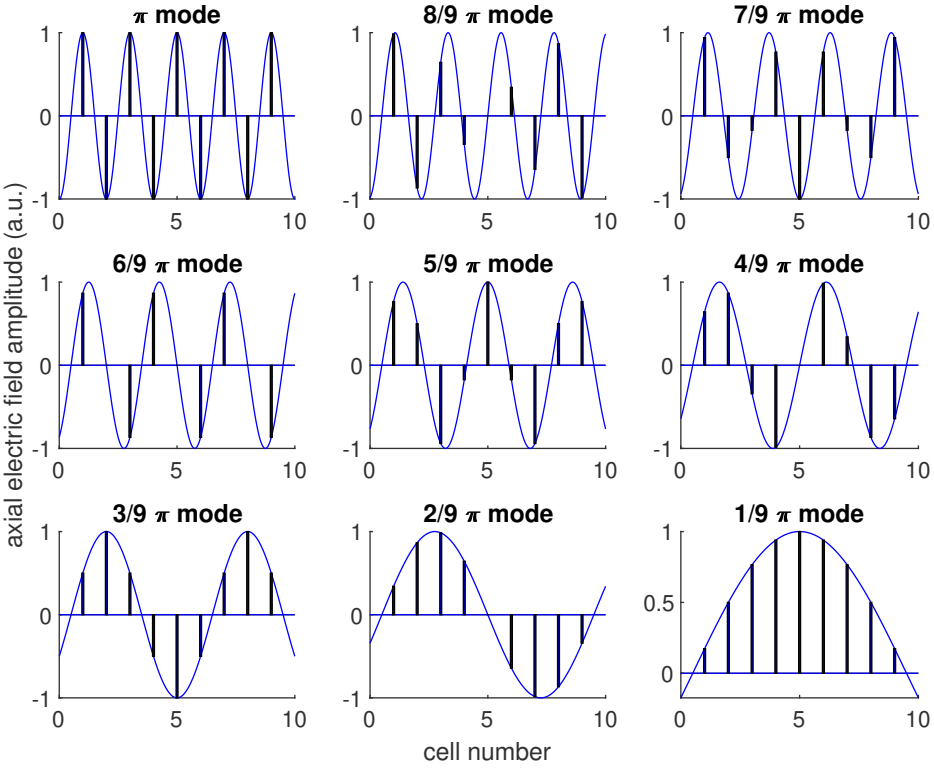

Figure 6: Axial electric field amplitudes of the orthonormal eigenmodes from a 9-cell cavity.

where U stands for the stored energy in the cavity, ω_0 represents the resonant frequency and P_c is the dissipated power in the cavity walls. $Q_0/2\pi$ gives the number of cycles it takes to dissipate the energy stored in the cavity. The total energy is given by the equation

$$U = \frac{1}{2}\mu_0 \int_V |\boldsymbol{H}|^2 dV = \frac{1}{2}\epsilon_0 \int_V |\boldsymbol{E}|^2 dV,$$

where $\boldsymbol{H}$ describes the local magnetic and $\boldsymbol{E}$ the local electric field integrated over the volume of the cavity. ϵ_0 is the vacuum permittivity and μ_0 the vacuum permeability. The surface resistance R_s characterizes the losses due to Joule heating under the assumption that the surface resistance does not vary over the cavity surface, giving a power dissipation of

$$P_c = \frac{1}{2}R_s \int_S |\boldsymbol{H}|^2 ds,$$

where the integral is taken over the cavity inner surface. This gives for the quality factor

$$Q_0 = \frac{\omega_0 \mu_0 \int_V |\boldsymbol{H}|^2 dV}{R_s \int_S |\boldsymbol{H}|^2 ds} = \frac{G}{R_s},$$

while G is defined as the geometry constant, which is independent of material properties and cavity size but depends on the shape of the cavity. The quality factor depends on cavity

size while R_s depends on the frequency [1]. A theoretical description of R_s is presented in the following section.

1.3 Superconductivity

Superconductivity is a phenomenon of vanishing electrical DC resistance at and below a material-dependent critical transition temperature, T_c. It was first observed in various metals such as mercury, lead, and tin by Heike Kamerlingh Onnes [19]. Most superconducting RF cavities consist of niobium, the chemical element with the highest critical transition temperature of $T_c = 9.2$ K under normal pressure. A superconductor is also a perfect diamagnetic material, as first shown by Walther Meißner and Robert Ochsenfeld in 1933 [20]. Thus a material in the superconducting phase will expel an external magnetic field as long as this field is below a certain critical field strength, H_c. This effect is related thermodynamically to the free-energy difference between the normal and superconducting states in zero field. It was empirically found that H_c can be approximated by a parabolic law

$$H_c(T) \approx H_c(0)[1 - (T/T_c)^2]. \tag{2}$$

The perfect conductivity and the Meissner effect which give superconductivity its unique interest were first well described by the brothers F. and H. London [21]. A parameter λ has been introduced as a penetration depth in which a magnetic field is exponentially shielded from the interior of a superconducting sample i.e. the Meissner effect. The London equations give an ideal theoretical upper limit for $T \to 0$ as

$$\lambda_L(0) = \left(\frac{mc^2}{4\pi n e^2} \right)^{1/2},$$

where m is the electron mass, e the electrical charge, n the electron density and c the speed of light. Based on the idea of a non-local generalization of Ohm's law where the current is localized by fields within a volume with a certain radius [22], a non-local generalization of the London equation was proposed by Pippard [23]. He argued that the superconducting wavefunction has a characteristic dimension ξ_0. It can be estimated from the uncertainty principle according to which only electrons within the Fermi energy contribute to superconducting phenomena. They have a momentum range of $\Delta p \approx k_B T_c / v_F$, where v_F is the Fermi velocity and k_B the Boltzmann constant, resulting in

$$\Delta x \gtrsim \hbar / \Delta p \sim \hbar v_F / k_B T_c,$$

while $\hbar = \frac{h}{2\pi}$ and h denotes the Planck constant. This leads to the characteristic so-called Pippard coherence length

$$\xi_0 = a \frac{\hbar v_F}{k_B T_c}, \tag{3}$$

with a being a numerical constant. Superconductors such as tin and aluminum were found to have $\xi_0 \gg \lambda_L$. Pippard assumed that, in the presence of scattering, the coherence length ξ is in relation to that of a perfect material ξ_0 as

$$\frac{1}{\xi} = \frac{1}{\xi_0} + \frac{1}{l}, \tag{4}$$

where l is the electron mean free path.
Cooper [24] showed in 1956 that even a weak attraction can pair two electrons into a bound state. As long as the interaction is attractive, the Fermi sea of electrons is unstable against the formation of at least one bound pair. In order to produce an attractive interaction, the interaction potential must have negative values, which only happens when the motion of the ion cores is taken into account. The physical mechanism behind superconductivity arises through an electron that polarizes the medium by attracting positive ions, causing a slight ripple in its path, attracting another electron to this displacement. This results in an effective attractive interaction between the electrons. If this attraction is strong enough to overcome the repulsive Coulomb interaction, superconductivity results. The importance of the electron-lattice interaction via quantized lattice vibrations, also called phonons, to explain the mechanism behind superconductivity was first suggested in 1950 by Fröhlich [25]. In the same year this suggestion was experimentally confirmed by the discovery of the isotope effect [26], [27]. It shows that T_c and H_c of many superconducting metals are proportional to $M^{-1/2}$ for isotopes of the same element, with M being the isotope mass. The formation of Cooper pairs led to the foundation of a microscopic theory named after Bardeen, Cooper and Shrieffer [28]. In the microscopic BCS theory, Cooper-pair condensation is described via the BCS groundstate wavefunction, in which each pair forms a singlet having anti-symmetric spin. In the language of second quantization, this singlet wavefunction reads

$$|\psi_0\rangle = \sum_{k>k_F} g_{\mathbf{k}} c^*_{\mathbf{k}\uparrow} c^*_{-\mathbf{k}\downarrow} |F\rangle,$$

where $c^*_{\mathbf{k}\uparrow}$ and $c^*_{-\mathbf{k}\downarrow}$ stand for creation operators specifying the occupied states that create an electron of momentum $\mathbf{k}$ with spin up or down, $g_{\mathbf{k}}$ are weighting coefficients and $|F\rangle$ represents the Fermi sea with all states filled up to k_F. The effective total momentum and spin of a Cooper pair is zero, inheriting the same properties as a boson moving without friction, leading to the zero-resistance characteristic of superconductivity. All charge carriers are condensed into pairs at absolute zero and break up again at higher temperatures, until above T_c none of the carriers remain paired, passing over to the normal conducting state. Based on the BCS theory, the fraction of unpaired carriers n_n increases exponentially with temperature via $n_n \sim e^{-\Delta/k_B T}$ where 2Δ is the energy that is needed to break the pairs. Here the simplified picture known as the London two-fluid model [21] was used, where the total electron density n can be divided into two parts, n_s for superconduction and n_n for normal conduction. For a flow of alternating currents, the surface resistance of a superconductor is non-zero. The Cooper pairs travel without friction but have inertial mass. Therefore a retarded alternating-current (AC) electric field will be present in the penetration layer due to the time-delayed response of the Cooper pairs and the normal carriers will be constantly accelerated and decelerated, leading to dissipation proportional to the rf frequency squared.
An approximation for the surface resistance of a niobium cavity is given by the sum of the BCS resistance R_{BCS} and a temperature-independent part, the residual resistance R_0. In a simplified form, the surface resistance R_S below the crossover frequency, i.e. much smaller than $2\Delta/h \approx 10^{12}$ Hz [29] can be written as the sum of R_{BCS} of Nb for temperatures $T < T_c/2$ together with the residual resistance:

$$R_S = R_{BCS}(T) + R_0 = A\frac{\omega^2}{T} e^{-\frac{\Delta(T)}{k_B T}} + R_0,$$

where A represents a material-dependent quantity that depends on the energy gap at zero temperature $\Delta(T=0)=\Delta_0$, the intrinsic coherence length ξ_0 and the London penetration depth λ_L. The BCS theory is applicable in cases where the energy gap Δ is constant in space; if the material is inhomogenious, the fully microscopic theory becomes difficult. Already 7 years before the BCS theory was published, a more macroscopic theory was proposed by Ginzburg-Landau (GL) [30] in which a complex pseudo-wavefunction ψ is introduced to describe the superconducting electrons. The local density of superconducting electrons is then given by

$$n_s = |\psi(x)|^2.$$

Physically the wavefunction ψ can be thought of as a description of the probability distribution of the center-of-mass motion of the Cooper pairs averaged over time.
A new characteristic length is introduced in the GL theory, the so-called GL coherence length $\xi_{GL}(T)$. The GL coherence length describes the distance over which $\psi(\boldsymbol{r})$ can change without causing an excessive rise in energy. The ratio between penetration depth and coherence length defines the so-called GL parameter

$$\kappa_{GL} = \frac{\lambda_L}{\xi_{GL}}.$$

For typical superconductors, $\kappa_{GL} \ll 1$ and $\xi > \lambda$. It was Abrikosov who noticed [31] what would happen in the GL theory if κ_{GL} were large i.e. $\xi < \lambda$. He showed that an exact breakpoint between two regimes exists at $\kappa_{GL} = 1/\sqrt{2}$, separating superconductors of so called type I and II. For the type I superconductor i.e. $\kappa_{GL} > 1/\sqrt{2}$ and $\xi > \lambda$, an external magnetic field would be expelled until a critical field H_c is reached. Superconductivity will breakdown for $H > H_c$, as shown in Fig. 7 (a). A type II superconductor expels an external magnetic field up to a lower critical field H_{c1} where, instead of a discontinuous breakdown of superconductivity, a continuous increase in flux penetration starts until an upper critical field H_{c2} is reached, as shown in Fig. 7 (b). The critical field value H_{c2} is given by $\sqrt{2}\kappa_{GL}H_c$

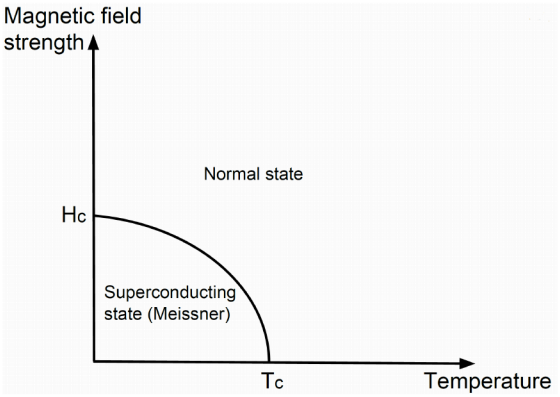

(a) Temperature dependence of criticial field from Type I superconductor. A parabolic behaviour was empirically determined and follows equation 2.

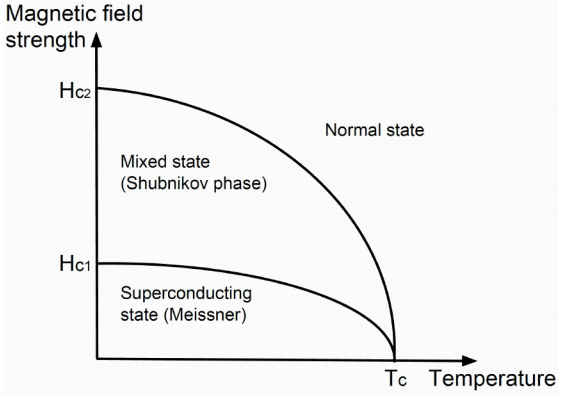

(b) Temperature dependence of criticial field from Type II superconductor.

Figure 7: Phase-diagram Type I and Type II superconductors [32].

and can be much larger than H_c, as the diamagnetic energy cost of keeping the field out

is less because of the partial flux penetration. Between H_{c1} and H_{c2}, the so-called mixed state or Schubnikov state exists, in which flux penetrates in a regular array of flux tubes, each carrying a quantum of flux $\phi_0 = \frac{hc}{2e}$. In Fig. 8, the one-dimensional variations of $\psi(x)$ and a magnetic field $h(x)$ are shown for the cases $\kappa_{GL} \ll 1$, referring to type I and $\kappa_{GL} \gg 1$, referring to type II superconductors. In the case of type I superconductors, a positive surface energy can be seen, since an inter-facial layer of $\sim (\xi - \lambda)$ between normal and superconducting material exists which pays the energetic cost of excluding the magnetic field. A negative surface energy results for type II superconductors, so that the subdivision into domains proceeds until it is limited by the microscopic length ξ. In fact it was shown by Gor'kov in 1959 that the GL theory is derivable as a limiting case of the microscopic BCS theory valid near T_c [33].
Niobium is a type II superconductor and has a GL parameter of $\kappa_{GL} \gg 1$. The BCS

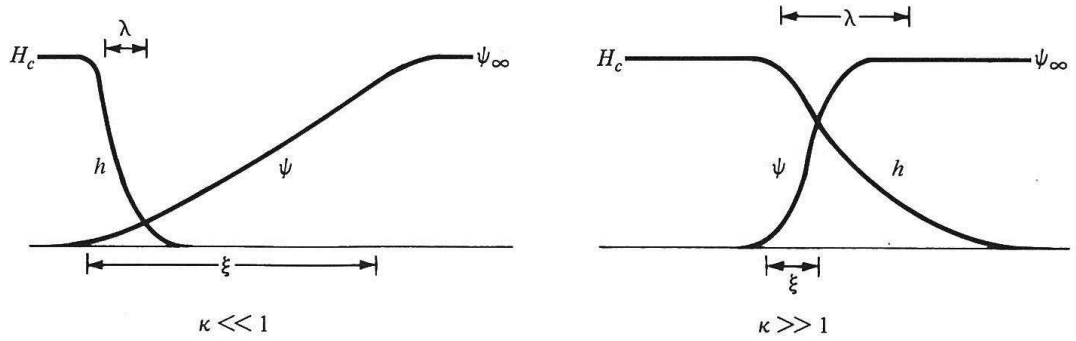

Figure 8: Contributions to the surface energy of type I ($\kappa_{GL} \ll 1$) and type II ($\kappa_{GL} \gg 1$) superconductors in the intermediate state $H \approx H_c$ in which superconducting and normal conducting domains exist, illustrated by the variation of one-dimensional pseudo wavefunction ψ and magnetic field h [22].

resistance for niobium at a frequency of 1.3 GHz is about 800 nΩ at 4.2 K and 15 nΩ at 2 K. In [34], the residual resistance has been found to be of the order of $10 - 20$ nΩ. The critical magnetic field is of utmost importance to maintain the superconducting Meissner phase and hence limits the maximal achievable accelerating field for a superconducting cavity. Niobium has an critical magnetic field of 190 mT at $T = 2$ K. A value about 20% higher has been measured in [35], which can be explained by the so-called superheating field. This phenomenon is related to the transition phase between the critical fields of a type-II superconductor. Energy is needed to nucleate a fluxoid which leads to the possibility of a metastable state where the energetically favorable transition has not occurred due to the activation-energy barrier which vanishes at the superheating field H_{sh}. The frequency correspond to times of the applied field has to be shorter than the relaxation time of this phase transition, which is in the order of 1 ns for niobium. The B_{peak}/E_{acc} ratio for a TESLA-type niobium cavity can be calculated to be about 4.26 $\frac{\mathrm{mT}}{\mathrm{MV/m}}$ [34]. With this ratio, the superheating field for niobium of about 228 mT gives a thermodynamical limit on the accelerating field of $\approx$ 55 MV/m. Several 9-cell cavities have been measured during the European XFEL production to have maximum achievable gradients above 40 MV/m [36]. A 9-cell TESLA cavity that reached up to 45 MV/m was reported in 2011 [37].

1.4 Surface superconductivity

Another critical field describing a surface effect, denoted H_{c3}, was predicted by Saint-James and de Gennes [38], [39]. The effect is caused by the finite size of real superconductors. Superconductivity can nucleate at a metal-insulator surface in a parallel field to a superconducting surface beyond H_{c2} while the bulk remains normal conducting. A superconducting surface sheath of thickness $\sim \xi(T)$ forms for field values between H_{c2} and H_{c3}, while $\psi \to 0$ applies inside the superconductor. For the superconducting interface, the boundary condition of the wave function ψ is given by

$$\left(\frac{\nabla}{i} - \frac{2\pi\vec{A}}{\Phi_0}\right)\psi\Big|_n = \frac{i\hbar}{b}\psi,$$

where $\vec{A}$ is the vector potential. The parameter b depends on the material that forms the interface with the superconductor. If it is an insulator, $b \to \infty$. If it is a magnetic material, $b \to 0$. For $\vec{H} \parallel \hat{z}$ normal to the surface the boundary condition is fulfilled by $\psi = e^{ik_y y}e^{ik_z z}f(x)$ for $k_z = 0$ (this is the relevant case for H_{c2}). Thus, H_{c2} corresponds to the magnetic field at which superconductivity begins on a surface in the direction normal to the applied field. For surfaces parallel to the applied magnetic field, the boundary condition becomes

$$\frac{\partial\psi}{\partial x}\Big|_{surface} = \frac{df}{dx}\Big|_{surface} = 0 \tag{5}$$

The eigenfunction $f(x) = e^{-\frac{(x-x_0)^2}{2\xi^2}}$ fulfils this condition for $x_0 = 0$ or ∞ at the surface, whereby in both cases the associated eigenvalue equals H_{c2}. An eigenfunction with a lower eigenvalue, which still fulfils the boundary condition described in equation 5, can be formed if k_y is chosen such that the position x_0 of the minimum of the effective potential lies within the surface of the superconductor at a depth ξ, as shown in Fig. 9. It turns out that this new surface eigenfunction must have a smaller eigenvalue than that of the volume eigenfunction, since it results from a smaller, broader potential than the simple parabola about x_0. The exact solution shows that the surface eigenvalue is smaller by a factor of 0.59, which leads to $H_{c3} = 1/0.59 \cdot H_{c2} = 1.695 \cdot H_{c2}$. Thus it can be concluded that superconductivity will nucleate in a surface layer of thickness $\sim \xi$ in a magnetic field parallel to the surface at a field $\approx 70\%$ greater than that at which nucleation occurs in the volume of the material. This indicates that a sample could carry a surface supercurrent in a wide range of fields when there is no volume superconductivity.

Doping the top layer with impurity atoms is expected to change the surface properties of the superconductor. The introduced impurity atoms reduce the mean free path l of the charge carriers within the superconductor and, as follows from eq. 4, subsequently also the coherence length. The coherence length introduced by Pippard differs from the coherence length ξ derived from the Ginzburg-Landau theory. However, $\xi(T) = \xi_0$ applies to pure superconductors far below T_c. For impure superconductors close to T_c, the coherence length is $\xi(T) = 0.855\sqrt{\frac{\xi_0 l}{1-t}}$, where $t = T/T_c$ [22]. By lowering the coherence length, the upper critical magnetic field increases with $H_{c2} \sim 1/\xi^2$. Since critical magnetic field of the surface H_{c3} is directly proportional to H_{c2}, this is also increased.

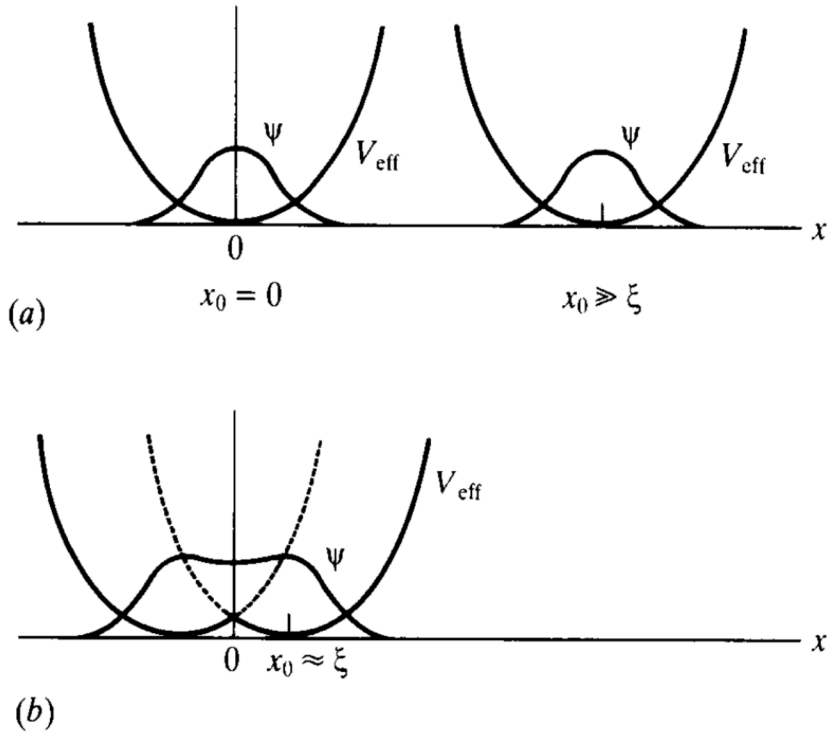

Figure 9: (a) Surface and bulk nucleation at H_{c2}. The corresponding eigenfunction is $f(x) = e^{-\frac{(x-x_0)^2}{2\xi^2}}$. (b) Surface nucleation at H_{c3}. The surface of the superconductor lies at x = 0. The trial function $f(x) = (1 + cx^2)e^{-ax^2}$ leads to the essentially perfect agreement with an resulting $H_{c3} = 1.659 \cdot H_{c2}$ where the parameters c and a were determined variationally by minimizing the Gibbs free energy. [22]

1.5 SRF cavity performance limitations

Superconducting radio-frequency cavities such as the elliptical TESLA-type cavities operating at 1.3 GHz offer the advantage of extremely low electrical surface resistance in the range of 10 nΩ at 2 K. The quality factors presently achieved exceed 10^{10}, far above that possible for normal conducting cavities. Several known mechanisms exist that influence the cavity performance. Corresponding characteristic Q_0 vs E_{acc} curves are illustrated in Fig. 10. This chapter briefly explains each of the performance limiting mechanisms.

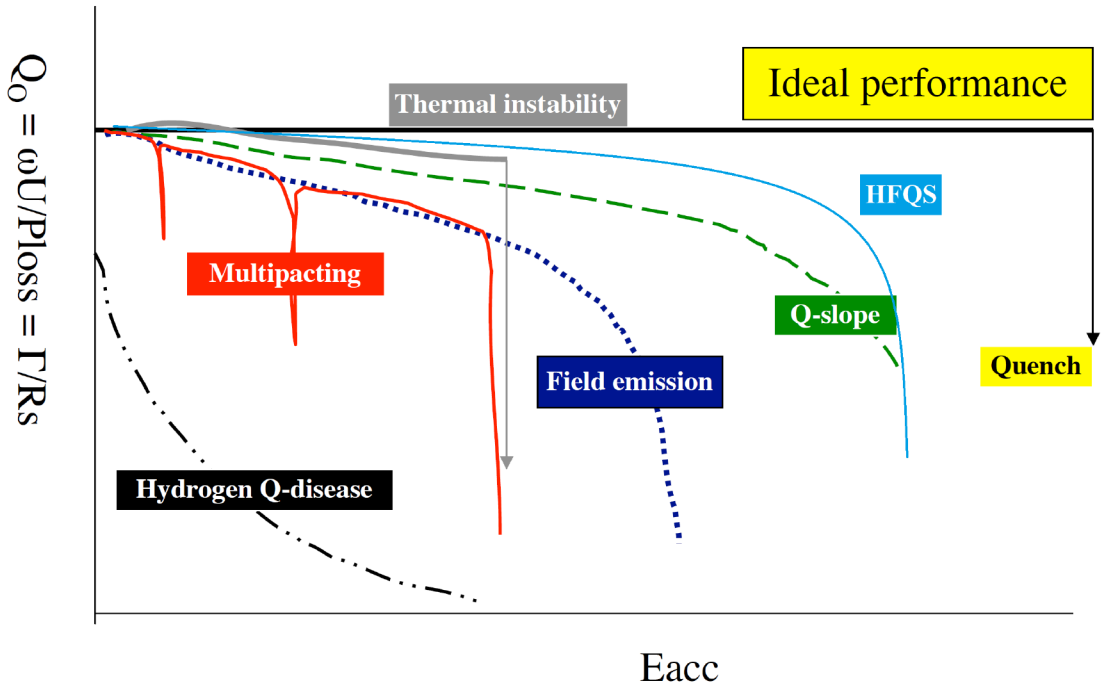

Figure 10: Schematic curves of quality factor vs. accelerating field for different performance limitations [40]. The theoretical limit is shown as the ideal performance. This is estimated from the thermodynamical limit for the gradient of 55 MV/m at an constant Q_0 factor of $1 \cdot 10^{11}$ where a $R_{BCS} \sim 8$ nΩ at 1.3 GHz and 2 K and $R_{res} \sim 2$ nΩ for niobium is assumed.

1.5.1 Breakdown of superconductivity (quench)

The accelerating gradient of a cavity can't be increased indefinitely. This phenomenon, known as quench, occurs when the electric surface resistance of the niobium increases suddenly until the superconducting state breaks down. The quench is characterized by a sudden drop in Q_0 as shown in Fig. 10. Fundamentally the gradient is limited by vortices penetrating the superconductor and overcoming the field of first penetration given by the theoretical rf critical magnetic field, the superheating field H_{sh}. Non-fundamental quench mechanisms are introduced in SRF cavities due to the existence of certain limiting factors that can be caused by for example defects at the RF surface. Two mechanism can cause a non-fundamental quench:

- A thermal quench can be initiated by a small region of the cavity surface, also called hot spots, in case a sufficient amount of heat is produced that cannot be cooled down enough by the helium bath, so that the hot-spot region cannot maintain the superconducting state any longer. For example, defects that become normal conducting cause heat dissipation leading to growth of the normal conducting zone until the cavity quenches.

- A magnetic quench, where a geometrical defect is still superconducting but leads to a local rise of the magnetic field above the critical field, thus exceeding the local field of first penetration.

The sharp increase in the surface resistance of the normal zone can only be controlled up to a certain heat-dissipation level. This level is the threshold that limits the fast spreading of the normal zone. The weld at the equator region is particularly often the source of quenches, since macroscopic defects occur more often and the magnetic field also has its maximum here.

1.5.2 Field emission

Electron field emission occurs when sharp tips or dust particles are present on the cavity inner surface. Electrons are emitted from the cavity inner surface driven by the electric field. This is most likely observed at the inner surface of the cavity irises, where the electric field reaches its highest value as shown in Fig. 5 (a) on page 13. The emitted electrons are accelerated by the rf field and can collide with the cavity surface, generating X-rays by Bremsstrahlung. The collision from the accelerated electrons with the niobium produces heat that increases the local temperature which can even lead to thermal breakdown. At the beginning of the TESLA cavity production, field emission at field strengths below 10 MV/m was a regular occurring problem due to residues from the chemical surface treatments. Improving clean room conditions and using high-pressure rinsing led to a significant reduction in particle surface contamination and helped to avoid field emission up to about gradients of 25 MV/m. However, geometrical defects are still common and can cause field emission occurring above field strengths of 25 MV/m.

1.5.3 Multipacting

Multipacting is a phenomenon describing electron avalanches occurring in a resonant trajectory. In case the electrons are synchronized with the rf field and the impact energy of the primary electron is in the range to produce a secondary electron i.e. if the secondary yield $\delta > 1$, a large number of electrons build up spontaneously and absorb rf energy, leading to high power losses and heating of the walls, thus reducing the quality factor. In cavities that operate in the axial-symmetric TM_{01} mode, multipacting happens mostly at the equatorial region where the electric field has its lowest and the magnetic field its highest value. Different cavity-surface treatments have produced different δ values. The yield has been measured on niobium bulk samples for different treatments [41]. It was shown that electropolished samples lead to lower δ as shown in Fig. 11. Furthermore it has been shown that heating niobium to 300°C reduces δ from 2.6 to 1.4 [42]. The elliptical TESLA cavity design shows varying magnetic field lines along the wall, drifting the elctrons to the

equator where no perpendicular electric field is present, thus preventing a further release of electrons [43]. Multipacting can be handled by allowing the cavity to multipact for a few minutes. The electrons clean the cavity surface and the δ falls below unity. As long as the cavity is held under vacuum, the multipacting is cured. Multipacting therefore rarely remains a permanent problem for TESLA cavities.

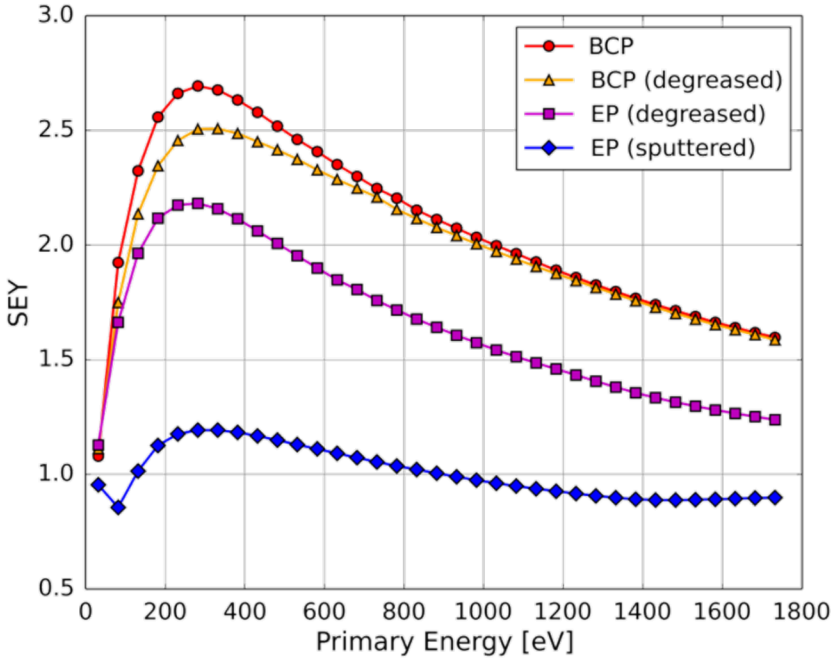

Figure 11: Secondary electron yield δ vs. energy of primary electrons for bulk niobium after different surface treatments [41].

1.5.4 Hydrogen Q-disease and HFQS

The hydrogen Q-disease [44] [45] [46] is known to cause a characteristic drastic Q_0 drop from 10^9 to 10^8 starting at low accelerating-field strengths as shown in Fig. 10. This phenomena is caused by hydride precipitation occurring during cavity cool-down to cryogenic temperatures. Hydrogen is absorbed exothermally by niobium and therefore it is difficult to avoid contamination of the cavity material during surface chemistry treatments using hydrofluoric acids. The Q-disease only occurs if there is a significant amount of bulk hydrogen concentration and the cool down is long enough to grow large niobium hydrides. A typical approach to reveal large amounts of hydrogen contamination is to hold the cavity at about $80 - 175$ K during the cool down for several hours. At these temperature the Nb-H precipitates form and grow larger islands depending on the time spent at this temperature.

Nb-H precipitates are superconducting below 1.5 K but the surface fields can still be sustained up to the breakdown of the proximity effect (Cooper pairs can diffuse from a su-

perconducting metal into a normal metal in close proximity [22]) acting on the niobium hydrides in the near-surface layer [47] which causes decreasing Q_0 values with increasing field, as shown in Fig. 10. This behaviour in fact holds for any weakly superconducting precipitates (i.e. with a T_c much lower than that of pure niobium). In [47] it is also proposed that the high-field Q-slope referred to as HFQS in Fig. 10 can be quantitatively described by the same effect but is caused by the hydrogen within the segregation layer near the surface that can also precipitate during fast cool down.
It has been found that baking the cavity under UHV conditions at 700-900°C can cure the Q-disease, while the HFQS has been found to be cured by a so-called "mild baking" under UHV at 120°C [48].

1.6 Residual Resistivity Ratio

Improving the thermal conductivity of niobium has been proven to be an effective method to shift thermal breakdown of SRF cavities to higher fields [45] [49] [50]. The high thermal conductivity is required to dissipate heat from the cavities into the surrounding liquid helium which is used to cool the cavities to operating temperatures of 2 K. Particles, impurities or lattice defects that cause heating of the surrounding niobium material to temperatures above T_c can lead to a quench of the cavity. Hence, better thermal conduction allows the generated heat to dissipate away from the heat source, permitting cavity operation at higher accelerating gradients. An important relevant measure is the so-called "residual resistance ratio" (RRR).
From the Mathiessen rule [51] the electrical resistivity of metals at low temperature can be written as

$$\rho = \rho_{res} + \rho_{ph}(T)$$

where ρ_{res} describes the residual resistivity at $T = 0$ K that is predominantly evoked due electron-impurity scattering and scattering on lattice defects while ρ_{ph} is produced by the temperature dependent electron-phonon scattering [52].
The scattering of conduction electrons on uniformly distributed chemical defects (foreign atoms) causes resistivity that is proportional to the defect concentration. The residual resistivity can be assumed to scale linearly with the impurity concentration as [52]

$$\rho = \sum \frac{\Delta\rho_i}{\Delta C_i} C_i + \rho_{ph}(T), \tag{6}$$

with $\frac{\Delta\rho_i}{\Delta C_i}$ being the resistance coefficients given in Table 1 for the most important impurities in Nb.
By definition, the RRR is the ratio of electrical resistance $\rho(T)$ at room temperature to that at 4.2 K:

$$\mathrm{RRR} = \frac{\rho(295\ \mathrm{K})}{\rho(4.2\ \mathrm{K})}. \tag{7}$$

Since the critical temperature of niobium is with $T_c = 9.2$ K, above the temperature of

Table 1: Resistance coefficients for different elements [53] determined by resistance measurements on niobium intentionally contaminated by impurities.

Element	O	N	C	Ta	Zr
$\frac{\Delta\rho_i}{\Delta C_i}$ $(10^{-11}\ \Omega\mathrm{m}/wt.ppm)$	2.64	3.49	3.33	0.12	0.6

liquid helium, the value of $\rho(T_c = 9.2\ \mathrm{K})$ is normally extrapolated down to $\rho(4.2\ \mathrm{K})$.
The thermal conductivity $\kappa_{thermal}$ is directly related to the electrical conductivity, which can be derived from the free-electron-gas model as described by the "Wiedeman-Franz" law. From that, the relationship between RRR and the superconducting-state thermal conductivity κ at 4.2 K can be derived as:

$$\mathrm{RRR} = 4 \cdot \kappa_{thermal,supercon.}. \tag{8}$$

The thermal conductivity of three niobium samples is shown in Fig. 12. A sharp drop below T_c can be seen for all three samples, where the thermal conductivity increases with RRR.

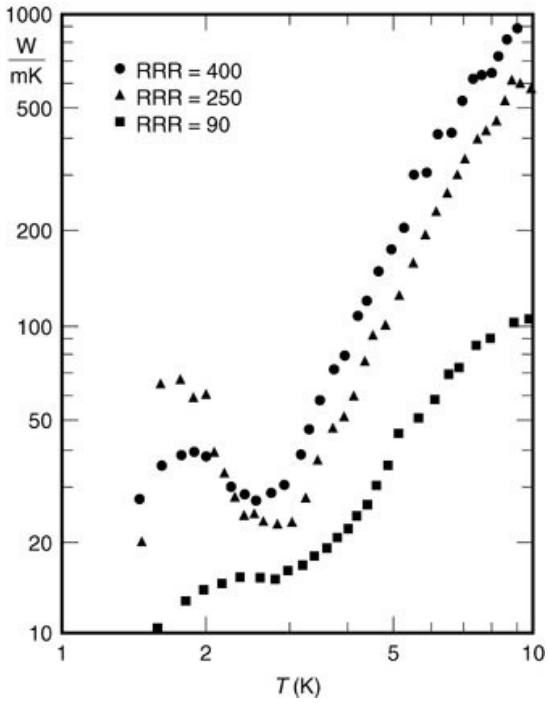

Figure 12: Thermal conductivity of three niobium samples with different RRR. The sample with RRR = 90 is as received, RRR = 400 after postpurification with yttrium, and RRR = 250 after annealing the postpurified sample for 6 hours at 1400°C, which degraded the purity but increased the crystal grain sizes [54].

Heat conduction for temperatures near and above T_c is dominated by electrons because the number of phonons (lattice vibrations) $\propto T^3$. The few remaining phonons are also scattered by electrons. Below T_c, electrons start to freeze out into Cooper pairs, which are not able to transport thermal energy, as they cannot be scattered by phonons. Therefore, the thermal conductivity drops sharply below T_c as shown in Fig. 12.
For temperatures below 4 K, the phonons start to dominate the thermal conductivity, causing an increase, leading to the phonon peak near 2K. Eventually heat conduction by phonons is limited by scattering with lattice imperfections, of which grain boundaries predominate. If the crystal grains of niobium are very large, a large phonon peak can be observed. Annealing at very high temperature can recrystallize the material and increase the grain sizes which is reflected in the thermal conductivity behavior of the sample with RRR = 250 in Fig. 12. This sample was annealed at 1400°C. As the phonon-electron interaction can be neglected for low temperatures, the electrical resistivity then starts to depend only on impurities and lattice defects. The higher the RRR, the fewer defects and interstitials in the material. Thus the RRR characterizes the purity of a metal.
The electronic mean free path l_e of a metal is a function of its purity level [55] [56] [57]. For electrons in niobium, the value of the normal-state electrical resistivity as well as l_e remain almost unaltered in the temperature range below T_c. As shown in eq. 7, the RRR describes the ratio between the resistivity $\rho_{295\mathrm{K}}$ at 295 K and the normal-state resistivity at a sufficiently low temperature. Consequently the RRR is a function of the electronic mean

free path, l_e under the assumption that $\rho_{295\mathrm{K}}$ is nearly independent of the purity level.
The BCS surface resistance calculated via the two-fluid model at a constant temperature of 2 K produces a minimum at $l_e \sim 10$ nm (corresponding to a RRR of ~ 4) as shown in Fig. 13. A RRR value of 300 or better has been established by the SRF community as the

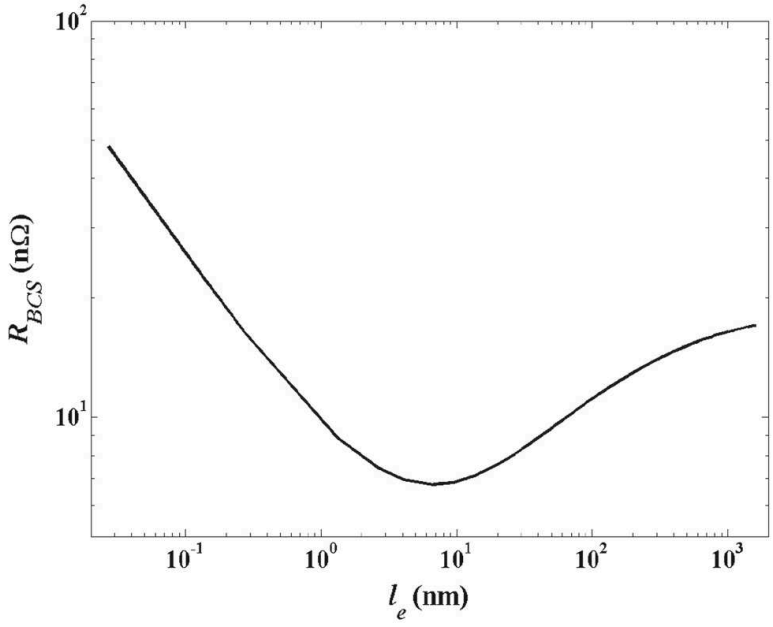

Figure 13: R_{BCS} as a function of l_e at 2 K for Nb calculated via the two-fluid model using the non-local response of electric field [58].

recommended choice for the niobium quality that is used for SRF cavity fabrication. This value is far from the calculated minimum in BCS resistance but a compromise with thermal conductivity has to be made, as eq. 8 elucidates.
Since the RRR value is a measure of the purity of the material, it is sensitive to changes in impurities due to diffusion during cavity treatments such as heat treatments in vacuum conditions or under certain gas atmospheres and after chemical surface treatments. Therefore, the RRR value is a particularly interesting parameter for niobium cavities and should be monitored especially during treatments such as nitrogen infusion, which will be discussed in more detail in the following chapters.

2 Cavity fabrication and preparation

In addition to the fact that niobium shows the highest critical temperature and critical magnetic field of all pure metals, it is also inert at room temperature since, a protective pentoxide layer covers the surface. Niobium has mechanical properties well suited for deep drawing, which makes it a suitable candidate for cavity production. An ingot of niobium it is purified by electron beam re-melting in a vacuum furnace so that impurities can "boil" out of the molten niobium. The ingot is forged into a slab, annealed and rolled gradually into sheets. After that, the material is again annealed to recrystallize. Depending on the desired grain size, the duration of this process must be adjusted carefully. This also has an effect on the RRR of the niobium. As explained in sec. 1.6, low impurity level as indicated by a high RRR has important benefits for superconducting cavities, since by the Wiedemann-Franz law it is directly connected to the thermal conductivity. Thus the niobium purity is important. A main contaminant is the metal tantalum, typically in a concentration of about 500 ppm by weight, since it is contained naturally in the niobium ores due to its similar chemical properties. An amount of 500-1000 ppm by weight is not considered to be harmful since it is mostly distributed in the bulk as a substitutional impurity not affecting the electrical properties [1]. Interstitially dissolved impurities such as oxygen, nitrogen, carbon and hydrogen are present in niobium. Niobium has a high affinity for oxygen above 200°C [1], making oxygen typically the most dominant interstitial. It is more dangerous than substitutional impurities such as tantalum and affects the RRR and thus the thermal conductivity, since the oxygen atoms can act as scattering centres for the electrons. According to [1], oxygen decreases the T_c of niobium by 1 K/at% whereas tantalum decreases T_c by 1 K/at%. Removing the interstials during the electro-beam melting stages of the ingot is the most convenient method to obtain high-purity niobium.
Niobium outgassing has been extensively studied at high temperatures [53]. From the starting content, melt rate and partial pressure of residual gases in the vacuum furnace, reactions, degassing rates, and equilibrium impurity content of oxygen, carbon, nitrogen, and hydrogen can be calculated. Results from such studies show that the equilibrium contribution from the residual gas in the furnace dominates the final interstitial impurity value after the first few melts. The amount of the interstitial impurities O, N, and C can be reduced to below 10 μg/g and for H close to 1 μg/g. Four to six melting steps are usually required to achieve such low impurity content. A RRR value of around 500 can ultimately be achieved [59].
Standard grain sizes of roughly 50 μm, referred to as fine-grain (FG) material, are formed via forging and rolling into 2.8 mm thick sheets. Grain sizes up to several centimeters can be achieved by directly cutting from the ingot; such material is called large-grain (LG) material. This newer manufacturing approach has shown benefits such as the elimination of the long production chain from large-grain ingot to fine-grain sheet. It seems to be more cost effective and provides cavities with naturally high Q_0 and large accelerating gradients [59] [60]. The impurity concentration for a typical European XFEL production sheet is given in table 2. The cavity fabrication and preparation process for European XFEL, which developed over years [62], differs in some production steps from the TESLA version in order to take into account some mechanical and safety aspects. Further details of the complete production chain can be read here [61].
More studies on the mechanical properties and development of treatments for SRF applications of niobium can be found in [63] [64] [65].

Table 2: European XFEL specifications for the niobium used for cavity production [61].

Electrical and mechanical properties		Impurity content (μg/g)			
RRR	> 300	Ta	≤ 500	H	≤ 2
Grain size	≈ 50 μm	W	≤ 50	O	≤ 10
Yield strength	> 50 N/mm^2	Mo	≤ 50	N	≤ 10
Tensile strength	> 50 N/mm^2	Ti	≤ 50	C	≤ 10
Elongation at fracture	$> 30\%$	Fe	≤ 50		
Vickers hardness	≤ 60	Ni	≤ 50		

2.1 Chemical surface treatments

The criteria for smoothness and cleanliness of the cavity surface are very demanding in order to achieve high accelerating gradients in superconducting cavities. A lot of work is therefore invested into the preparation of the inner surface of the cavity. During the development of the TESLA cavity design, several surface-treatment methods were developed to achieve high performances. The so-called buffered-chemical-polishing (BCP) and electropolishing (EP) played an essential role. In the following those two methods will be explained in further detail.

2.1.1 Buffered Chemical Polishing

For Buffered Chemical Polishing (BCP) an acid mixture 1:1:2 with their respective concentration of HF(48%), HNO_3(85%) and H_3PO_4(96%) is usually used, resulting in a removal rate of 1 μm per minute [66]. The hydrofluoric acid is used to dissolve niobium pentoxide, that is naturally present on the niobium surface. A re-oxidation of the niobium by an oxidizing agent is subsequently achieved using nitric acid. A mixture of HF and HNO_3 is heavily exothermic and removes 30 μm per minute [66]. This mixture would heat up quickly because of the reaction, which leads to a thermal runaway. Large amounts of gases are emitted at the same time. The Phosphoric acid is added as a buffer compound to reduce the reaction rate [67]. The BCP acid mixture is cooled to 15°C, which decreases hydrogen diffusion into the niobium [68] [69].

2.1.2 Electropolishing

Not only removal but also smoothing of the inner surface of a cavity can be achieved by electro-chemical polishing (EP) and is nowadays widely used for SRF cavities [70] [71]. During the EP, an external power source drives the oxidation process and sulphuric acid (H_2SO_4) is used as the oxidizing agent. A commonly used acid mixture is one part HF(48%) and nine parts H_2SO_4(96%). The hydrofluoric acid dissolves the niobium pentoxide generated from it. One benefit of electropolishing over BCP is that enhanced control of the process stability is provided by the application of a voltage in the surface-removal process. The electric field is enhanced by protrusions, which are therefore removed more rapidly than the average, providing a smoother overall surface. The applied voltage regulates the chemical reaction, thereby preventing issues such as thermal runaway during BCP. Some

sulphur may remain on the cavity surface, as sulphuric acid is used in this process. Subsequent ethanol rinsing removes these residues. The removal rates for electropolishing vary depending on the temperature, anode to cathode distance, anode to cathode voltage and the anode current density, etc. In [72] a removal rate of 0.3 μm/min, which is typically used for the SRF cavity, is specified. After a standard EP treatment, the resulting surface roughness is around 0.5 μm, whereas for BCP cavities it is $1 - 5$ μm. It is widely accepted that EP-treated cavities can achieve higher acceleration fields than BCP cavities [66] [73].

2.2 European XFEL cavity production

The main steps for cavity preparation for the standard European XFEL process after the welding of the equator seams is given in Fig. 14, denoted as "Final EP Scheme". The sheet rolling and half-cell deep drawing, causes mechanical damage in a layer of about 100 μm from the inner surface (damage layer). Therefore, as a first step, $110 - 140$ μm is removed from the inner surface via electro-chemical polishing. This is followed by 800°C annealing (baking) in vacuum conditions, so that the niobium can partially recrystallize and elastic deformations of the material can relax. As already mentioned in sec. 1.5.4, hydrogen can be loaded into the material during electro-chemical polishing, causing Q-disease. The baking step mostly removes the hydrogen. Depending on the vacuum condition and partial pressure of residual gases, the cavity inner surface again becomes contaminated with interstitial impurities during the baking step. To treat this, a second electro-chemical polishing or buffered chemical polishing is included in the process flow after the 800°C baking, in which $10 - 40$ μm are removed. Finally, a 120°C baking in vacuum conditions follows for 48 h. This proved beneficial for cavity performance and cured the HFQS as mentioned in sec. 1.5.4.

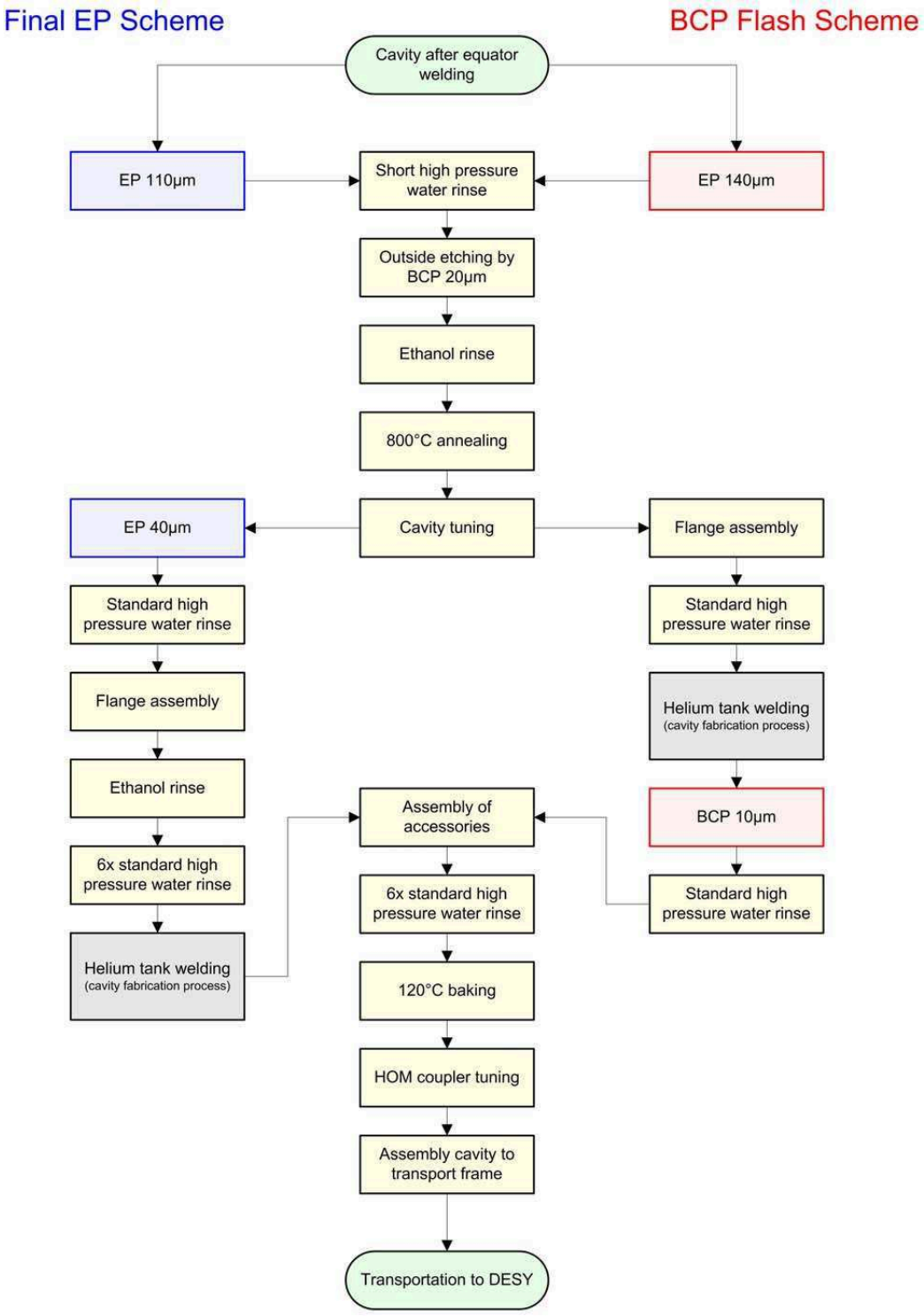

Figure 14: Work flow for cavity preparation for European XFEL and FLASH at DESY [74].

3 Sample preparation

3.1 Sample shape and surface treatments

The niobium samples used in this work were made either in conical or cylindrical form. The samples were cut from niobium sheets with a thickness of 2.8 mm left over from European XFEL cavity production. The conical samples have an outer diameter of 13.23 mm on the bottom and an inner diameter of 10 mm on the top, as illustrated in Fig. 15 (a). Cylindrical samples have an diameter of 10 mm, as shown in Fig. 15 (b). Samples are stored in

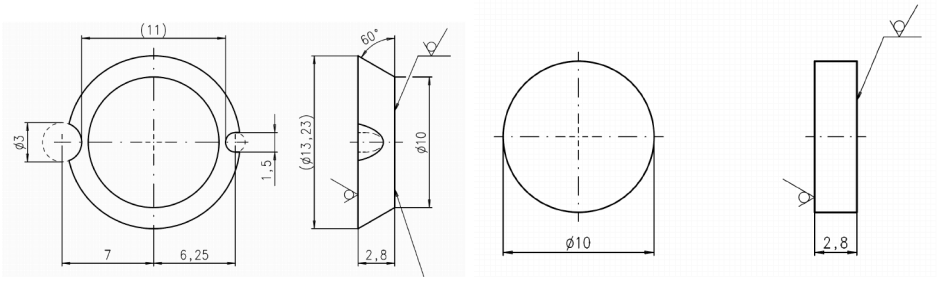

(a) Sample in conical form. (b) Sample in cylindrical form.

Figure 15: Mechanical drawings of samples. The samples are cut from high purity cavity grade material with RRR $\geq$ 300.

a non-magnetic aluminum holder designed for use on measurement instruments such as a scanning electron microscope (SEM). Sticking with conducting tape, which is usually used to make electrical contact between sample and holder to avoid local charging by the secondary electrons from the SEM, is not needed and thus adhesive residue is prevented. The holders are shown in Fig. 16. The samples are placed on the bottom part of the holder from Fig. 16 (a). The top part (Fig. 16 (b) or (c)), for conical or cylindrical samples respectively, is held by three screws holding the samples tight as shown as an example for an conical sample in Fig. 17. The aluminum holder can be used in the same high-pressure rinsing system as for cavities in the DESY clean room [75]. An adapted Teflon holder as shown in Fig. 18 which can hold up to ten samples. If samples are required to be treated in a way as close as possible to how cavities are treated, the European XFEL recipe as described in Fig. 14 for the "Final EP Scheme" was used in an EP system for samples and a sample furnace set up to ensure identical treatment to that experienced by the surface of cavities.

3.2 Sample furnace

Some heat treatments in vacuum conditions or nitrogen atmosphere of samples were carried out in a sample furnace. A photograph of the furnace is shown in Fig. 19. The sample furnace is from the company Carbolite Gero GmbH & Co. KG and consists of a ceramic tube with a bore of 1000 mm length, 90 mm in outer and 80 mm in inner diameter (Pythagoras Typ C 610) capable of being heated up to 1350°C. A pump-stand by Edwards is connected, consisting of a nEXT240D turbo-molecular pump (TMP) and a nXDS6i scroll pump. A more detailed flow chart is shown in Fig. 20. A bypass line at hand-valve 3 (HV3), as shown in Fig. 20, is installed to reduce the pumping speed and hence the amount of nitrogen

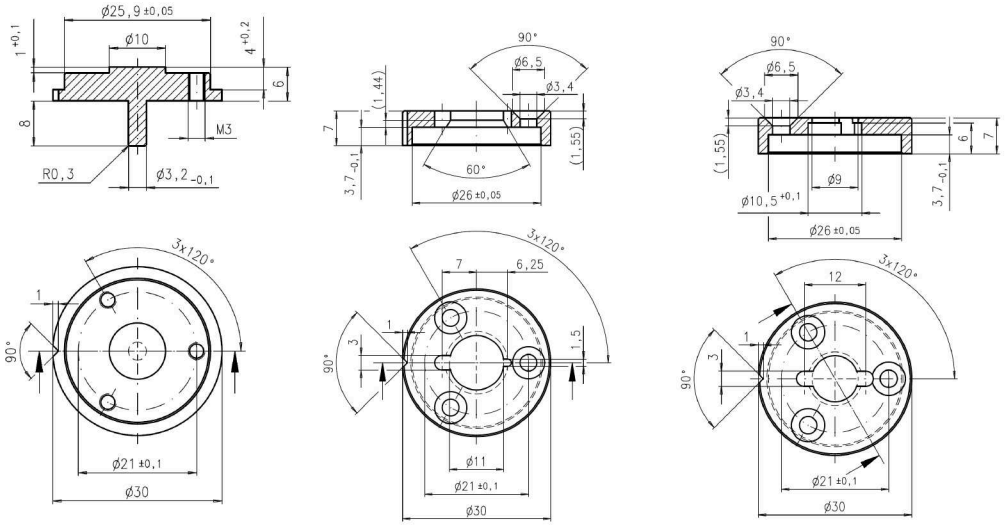

(a) Bottom part of the sample holder.

(b) Top part of conical sample holder.

(c) Top part of cylindrical sample holder.

Figure 16: Mechanical drawing of bottom and top part for conical and cylindrical sample holders. The holders are made of highly pure nonmagnetic aluminum alloy.

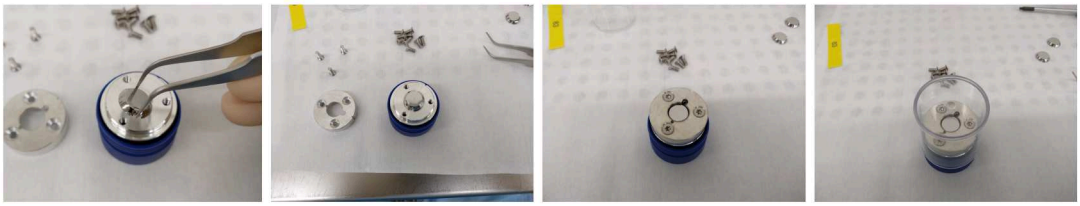

Figure 17: Mount of conical sample in aluminum pin stub holder. The aluminum pin stub is placed in a transport tube for storage, shipping and transport. It protects the samples from contamination.

gas needed to control the pressure. This helps to maintain a more sensitive regulation of the pressure in the chamber. Two full-range pressure gauges are installed: WRG1 (type WRG-S-NW25 by "Edwards") by which the TMP is controlled is behind the hand valves HV2 and HV4 as shown in Fig. 20; WRG2 (type Pkr 261 by "Pfeiffer") is installed in front of the ceramic tube, measuring the pressure of the chamber vacuum as close to it as possible. The gas inlet is controlled by a regulator-type Pfeiffer RVC300 via the measured pressure in the tube by WRG2, enabling it to maintain the desired nitrogen partial pressure in a reproducible way. To examine gas constituents and ensure the cleanliness of the vacuum system and nitrogen gas, an residual gas analyzer is installed. The furnace temperature is mapped by a temperature control system by GERO and additionally measured by a vacuum thermocouple sensor. Bottled high-purity dry nitrogen gas (6.0 standard) is connected to the injection line. For the investigations reported in this thesis, major changes at the furnace to improve vacuum conditions, such as the change from Klein Flange (KF) to CF (ConFlat)

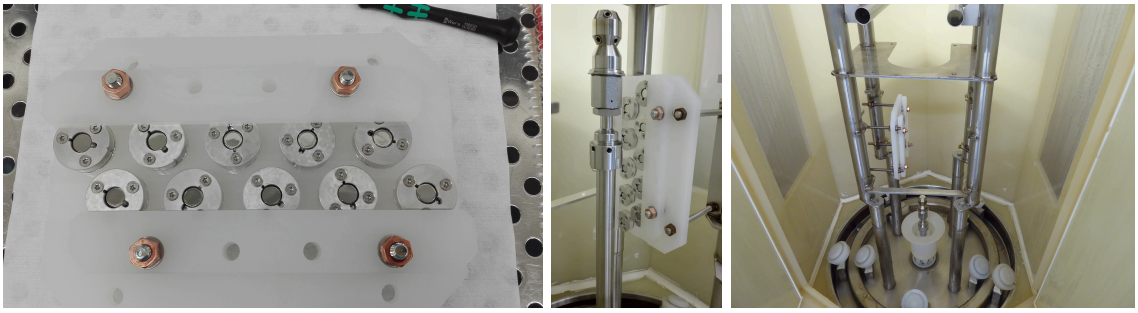

Figure 18: Sample mount for high pressure rinsing. The ten aluminum pin stub holders, with conical samples installed in them, are mounted on a board made out of teflon and firmly screwed on the side with two elongated pieces of teflon. The teflon board can be placed at the same spot as a cavity for high pressure rinsing.

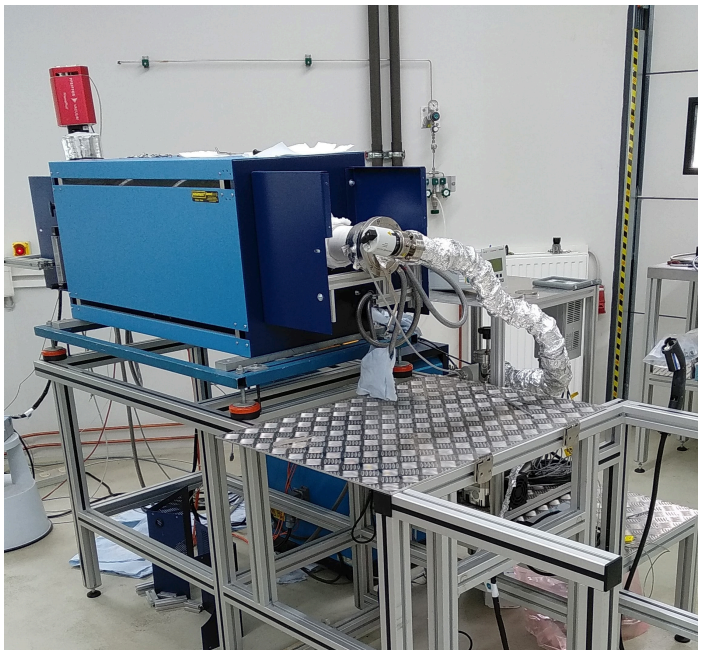

Figure 19: Image of the small sample furnace. For further details, see text.

flanges, were made. For that, a weld at the outer ISO-F flanges of the ceramic tube was required. To qualify the system in a first step, a "rate of rise" test was performed, simply following the pressure increase when all valves to the pumping unit were closed. The data is shown in Fig. 21. The curve labelled 30.05.2018 shows the initial data, which was taken before the change from KF to CF seals. The curve labelled 09.09.2019 is after the change. The pressure rise was recorded with WRG2 by closing HV2 and HV3 and started at a pressure of about $7 \cdot 10^{-7}$ mbar. The pneumatic valve from Pfeiffer has a KF connection. Specially designed stainless-steel KF chain clamps by the company "EVAC" in Switzerland, suitable for ultra-high vacuum up to $1 \cdot 10^{-10}$ mbar, were therefore used for the connection

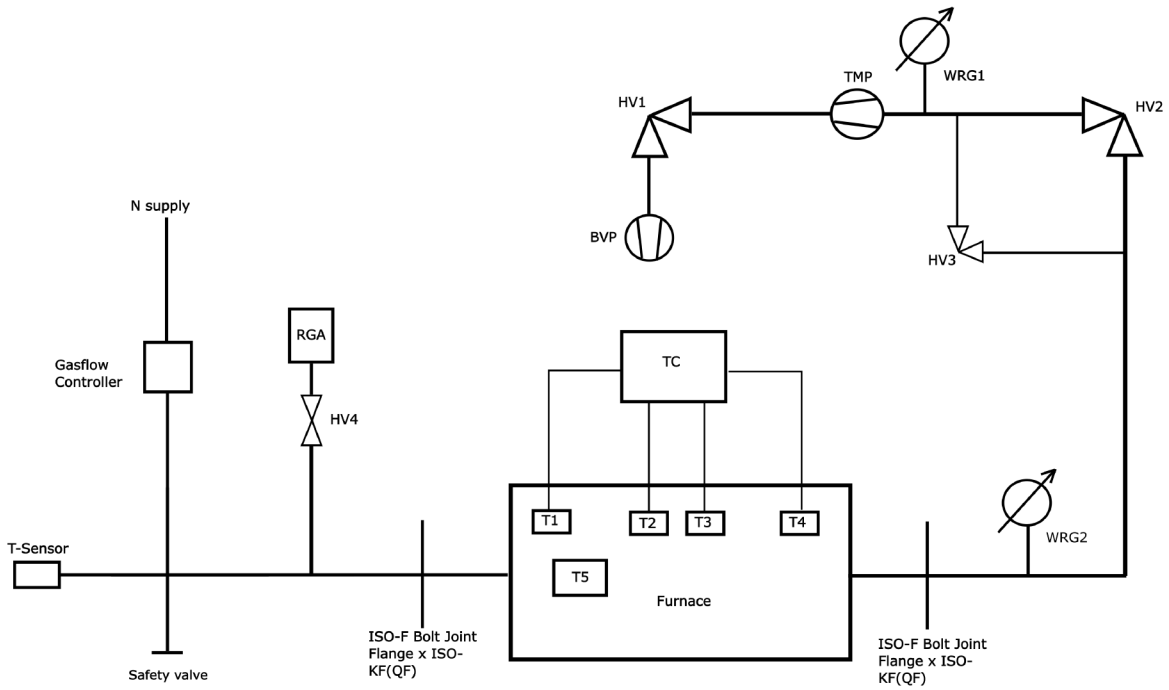

Figure 20: Flow chart of sample furnace. HV: Hand valve; BVP: Backing pump; TMP: turbo-molecular pump; WRG: full range pressure gauge; TC: Temperature control; T"X": Temperature sensors with number "X"; RGA: Residual gas analyzer;

to the pneumatic valve. A helium leak test with the RGA showed no leak up to a leak rate of $\sim 6.6 \cdot 10^{-8}$ $\frac{\text{mbar} \cdot l}{s}$ from any part of the furnace at this point. Nevertheless, later a major leak between ceramic and the metal flange glued seal occurred. Hence, a new ceramic tube of the same type and company was installed. The rate-of-rise with the new ceramic tube directly after installation is shown in the curve labelled 13.05.2020 and already shows an improvement. Nonetheless, leaks were found at both transitions between ceramic and metal flange. These could be closed with the help of "Vacseal" a high-vacuum leak sealant. The rate-of-rise after cleaning processes and several bakeouts up to 1000°C shows a significant improvement, as demonstrated in the curve labelled 08.11.2020, where the starting pressure was $5 \cdot 10^{-8}$ mbar. It was then also possible to achieve a final pressure of $2 \cdot 10^{-8}$ mbar at WRG2. From this, the local desorption rate can roughly be estimated as $1 \cdot 10^{-11}$ $\frac{\text{mbar} \cdot l}{s \cdot \text{cm}^2}$.

An RGA spectrum is shown in Fig. 22 in blue. Peaks are seen at typical masses for air at molecular weights of 1,2 and the so-called "water stairs" from 16 to 18. The masses $19(F^+)$ and $20(HF^+)$ could be explained by the Teflon tubes used for the nitrogen line from bottle to pneumatic valve. The masses 28, 29 and 32 are constituents of air, as are $40(Ar^+)$ and $44(CO_2^+)$. In order to check the gas constituents of the nitrogen line, the RGA spectrum was taken while nitrogen was being inserted by a small amount until the starting pressure of $2 \cdot 10^{-7}$ mbar dropped to $5 \cdot 10^{-7}$ mbar. The spectrum is shown in Fig. 22 in green. The masses 14, 28 and 29 increase corresponding to nitrogen insertion. It can be seen that there is no pollution of nitrogen or leaks in the line. The following figure 23 shows

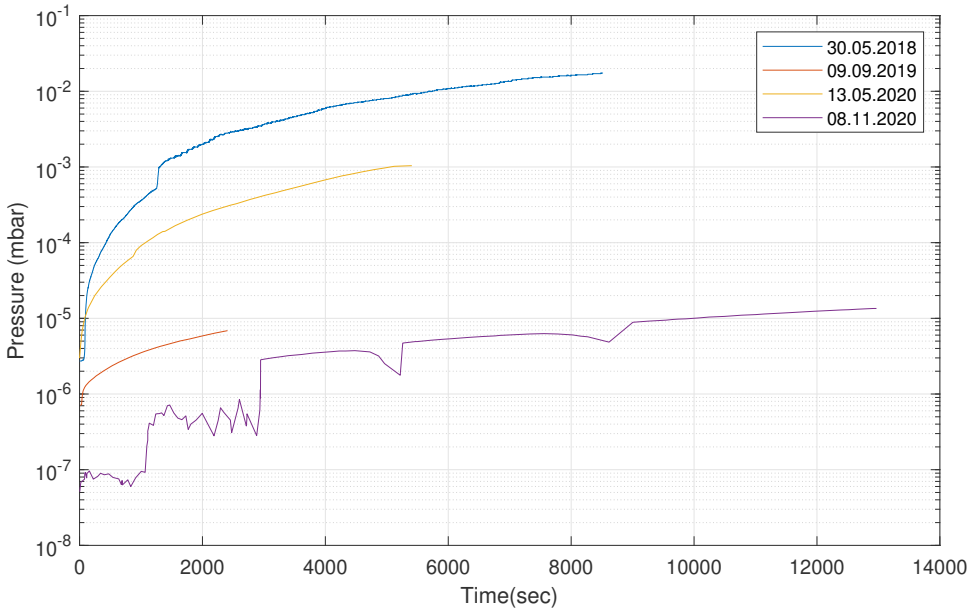

Figure 21: Pressure against time from a rate-of-rise test of the sample furnace recorded at WRG2 with HV2 and HV3 closed at room temperature and for different dates. The most recent shown in purple has a starting pressure of $5 \cdot 10^{-8}$ mbar. The jumps in the beginning of curve labelled as 08.11.2020 are measurement artifacts.

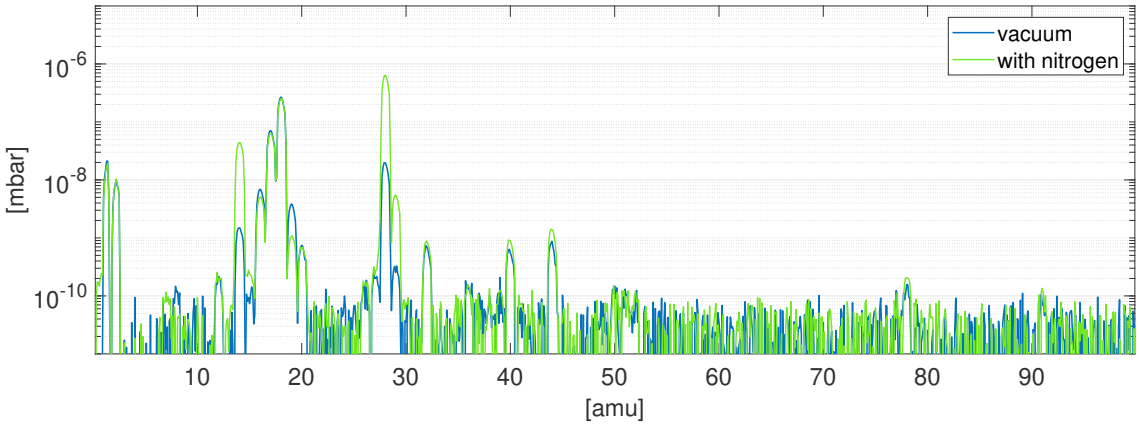

Figure 22: RGA spectrum at room temperature with and without the addition of nitrogen. In vacuum (blue) at a pressure of $2 \cdot 10^{-7}$ mbar recorded from WRG2. With nitrogen (green) where the gas-flow controller is set via WRG2 to a nitrogen partial pressure of $5 \cdot 10^{-7}$ mbar.

mass spectra recorded during a nitrogen-infusion process. The nitrogen-infusion process was carried out by initially heating from room temperature to 800°C under vacuum conditions.

Subsequently, after waiting at a temperature of 800°C for 3 hours, it was again reduced to 120°C. When 120°C has been reached, nitrogen was introduced so that the pressure was constant at $3.3 \cdot 10^{-2}$ mbar. Figure 23 (a) was taken at room temperature shortly before the heat ramping started, at an initial pressure of $3 \cdot 10^{-8}$ mbar. Figure 23 (b) was taken at 800°C and a pressure of $1.3 \cdot 10^{-6}$ mbar. Figure 23 (c) was taken at 120°C after the hold at 800°C; a pressure of $1.8 \cdot 10^{-8}$ mbar was recorded here. Finally Fig. 23 (d) was taken when the nitrogen partial pressure was set to $5 \cdot 10^{-7}$ mbar. The RGA was then switched off and HV4 closed in order to continue with the Nitrogen Infusion at $3.3 \cdot 10^{-2}$ mbar, since the RGA could be damaged if the pressure was above $1 \cdot 10^{-5}$ mbar. The vacuum condition here was even better than that in the previous nitrogen test shown in Fig. 22. The water stairs are less pronounced and the overall pressure has been improved due to further bakeouts. The vacuum quality at 120°C as shown in Fig. 23 (c) shows excellent clean conditions. The spectrum after nitrogen inlet in Fig. 23 (d) shows a increase in nitrogen during the heating step at 120°C.

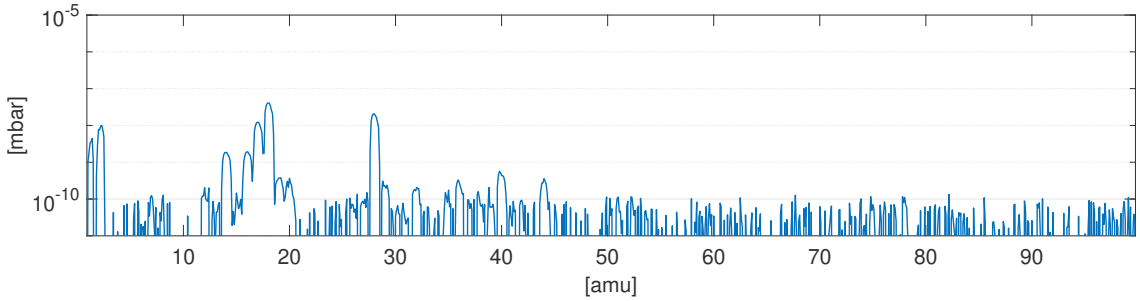

(a) RGA spectrum at room temperature and a pressure of $3 \cdot 10^{-8}$mbar recorded from WRG2.

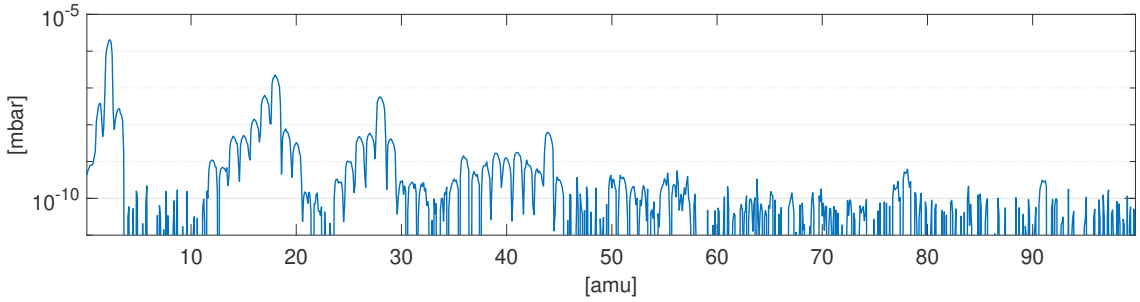

(b) RGA spectrum at 800°C and a pressure of $1.3 \cdot 10^{-6}$ mbar recorded from WRG2.

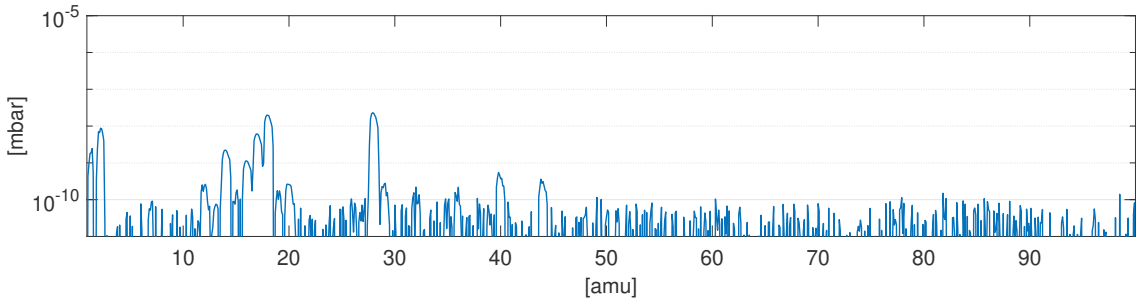

(c) RGA spectrum at 120°C and a pressure of $1.8 \cdot 10^{-8}$ mbar recorded from WRG2.

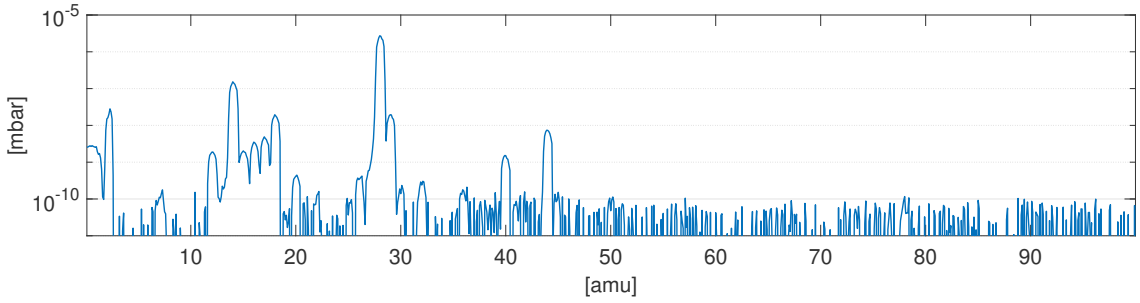

(d) RGA spectrum at 120°C where the gas-flow controler is set via WRG2 to a nitrogen partial pressure of $5 \cdot 10^{-7}$ mbar.

Figure 23: RGA spectrum during a 120°C nitrogen infusion run.

4 The role of nitrogen for niobium SRF cavities

4.1 Nitrogen doping

The discovery of the enhancement of niobium cavity performance by nitrogen enrichment happened a few years ago. Different recipes have been published since then. The nitrogen-doping treatment as reported in 2013 by Anna Grassellino [76] consists of high-temperature annealing between 800-950°C in 10^{-6} mbar for 3h followed by anneal in a nitrogen-rich atmosphere around $2.7 \cdot 10^{-2}$ mbar for a certain period of time (usually 2-20 min) and a follow-up diffusion phase of 6-30 min while maintaining the temperature. Chemical etching then removes nitride precipitates from the niobium-cavity inner surface. Nitrogen doping

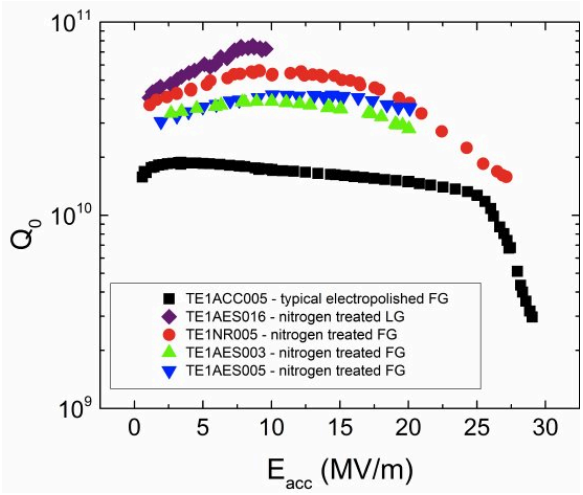

Figure 24: Q_0 vs. E_{acc} comparison between nitrogen-doping and standard EP treated cavities from [76].

increases the quality factor but the cavity starts to quench at mid ($\approx$ 20 MV/m) accelerating fields. Another special feature of the nitrogen doping is the so-called anti-Q-slope, where field dependence of the quality factor is reversed so that the surface resistance decreases with increasing field from low to mid fields, as shown in Fig. 24. Quality factors above $5 \cdot 10^{10}$ at 2 K can be achieved with this treatment, with the benefit of less RF heating and hence lower refrigeration costs. The nitrogen-doping recipe has existed for a considerable time now and therefore substantial research has been done and the treatment has already been employed in real devices. The Linac Coherent Light Source (LCLS-II) project at SLAC used nitrogen doping as one of the treatment processes for the SRF cavities to be placed in cryomodules [77]. Several exposure and annealing time trials were conducted in order to find the optimal formula that fulfilled the LCLS-II cavity performance parameters. The project's formula was the so-called 2N6 (2 minutes of nitrogen exposure followed by 6 minutes of annealing in a UHV atmosphere). Research to optimise the process, involving adjusting the nitrogen diffusion and annealing duration, continues.
If the cavity is not sufficiently shielded from external magnetic fields, flux can be trapped when the cavity enters the Meissner state [22]. Additional losses in RF fields can occur from this "trapped flux," resulting in a rise in temperature-independent residual resistance.

Nitrogen-doped cavities are known to have an increased sensitivity to trapped magnetic fields. Additional losses from trapped magnetic flux can result in considerable increases in dissipated power. The majority of residual resistance in well-prepared cavities has been found to be due to magnetic flux trapped in the cavity's walls. The quantity of ambient magnetic field trapped in the cavity walls is, however, greatly influenced by the specific dynamics of a given cool down. Fast cool down in nitrogen-doped cavities improved the Q_0 performance compared to slow cool down, according to Romanenko et al. [78]. Examining the NbN phase diagram in Fig. 25 shows that, at 800°C, nitrides will immediately start to precipitate on the surface in a nitrogen atmosphere. Nitride phases on the surface will act as

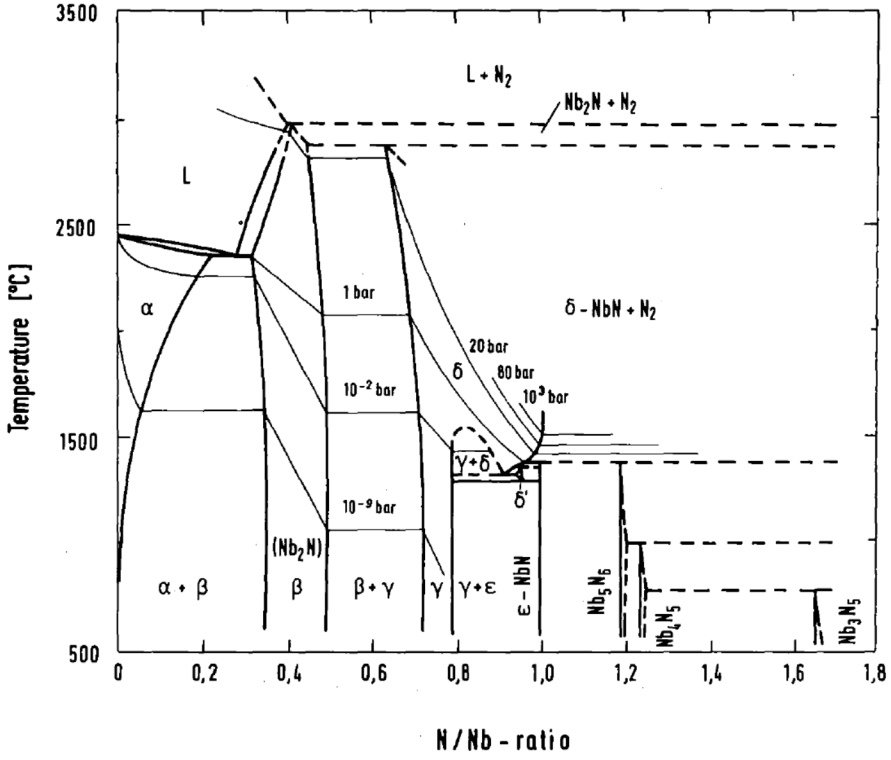

Figure 25: Nb-N phase diagram. [79]

an barrier, making it more difficult to have nitrogen atoms incorporated in a body-centered cubic Nb lattice as interstitials, without the host lattice transforming into a different phase, known as an $\alpha - \mathrm{NbN}_x$ solid solution. Nitrides also explain the star-shaped structures observed on a niobium sample surface that has been nitrogen doped as shown in Fig. 26, which probably belong to the hexagonal $\beta - \mathrm{Nb_2N}$ phase. Niobium nitride phases are not superconducting at 2K, which might be one explanation why they require a short post-treatment EP removal of about 5 μm to avoid bad Q degradation, as shown in Fig. 27 when not enough of the surface is removed. Furthermore, the precipitation compromises the surface smoothness.

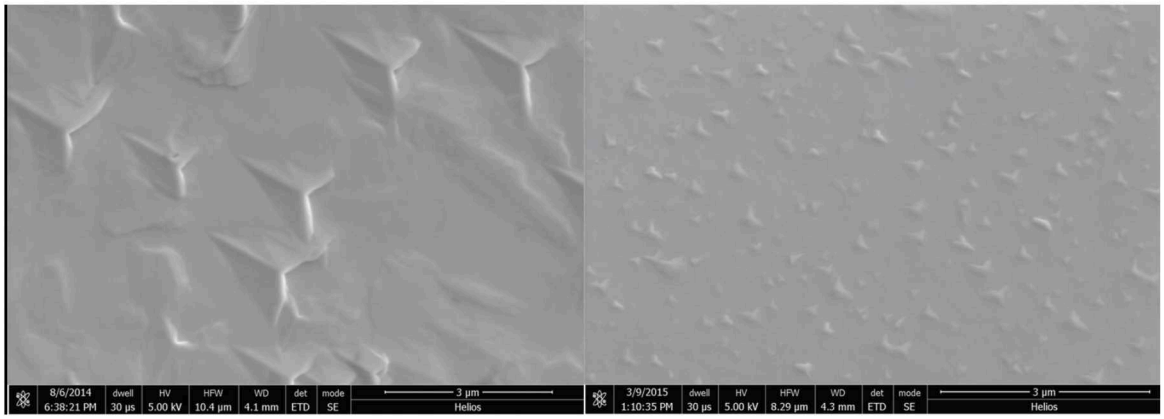

Figure 26: SEM images of a niobium sample after annealing at 800°C in nitrogen gas for 20 minutes on the left and for 2 minutes on the right. Images are taken from [80].

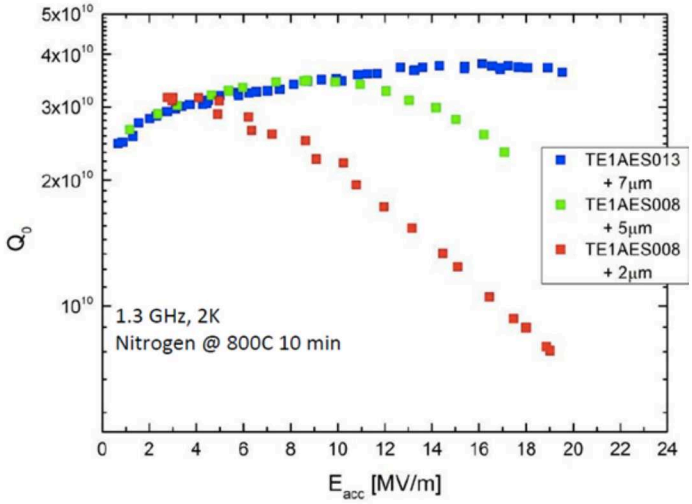

Figure 27: Cavity performance of nitrogen-doped cavities after different amounts of surface material removal. Graph taken from [81].

4.2 Nitrogen infusion

The "nitrogen infusion" recipe was discovered in 2016/17 again by Fermilab [5]. Here the nitrogen is introduced at 120°C at a partial pressure of $3.33 \cdot 10^{-2}$ mbar after the cavity has first been heated up to 800°C and then cooled down. The pressure and temperature curve for a 120°C baking in UHV and a successful 120°C-infusion run at Fermilab is shown in Fig. 28. Nitrogen infusion also increases the quality factor, although less than for doping. However, very high accelerating voltage (above 40 MV/m) can be achieved while maintaining the fairly high Q-factor of about $2 \cdot 10^{10}$ at 40 MV/m and no anti-Q-slope, as shown in Fig. 29. The mechanism behind the two recipes is not currently well understood. It is questionable if the physical mechanism that leads to the performance improvement is the same for both recipes. The nitrogen-infusion treatment is still not reproducible to the same extent in the

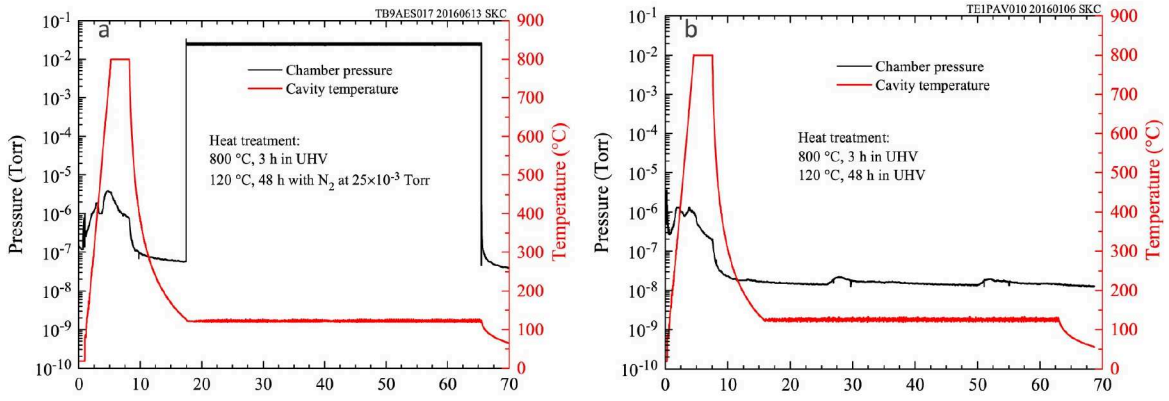

Figure 28: Pressure and temperature data for a nitrogen infusion run at 120°C on the left graph and a 120°C run in UHV on the right graph from Fermilab [5].

laboratories that have attempted it [82] [83] [84] [85]. This indicates that the nitrogen-infusion recipe has some key factors that lead to the success of the recipe that have not yet been identified to the same extent.

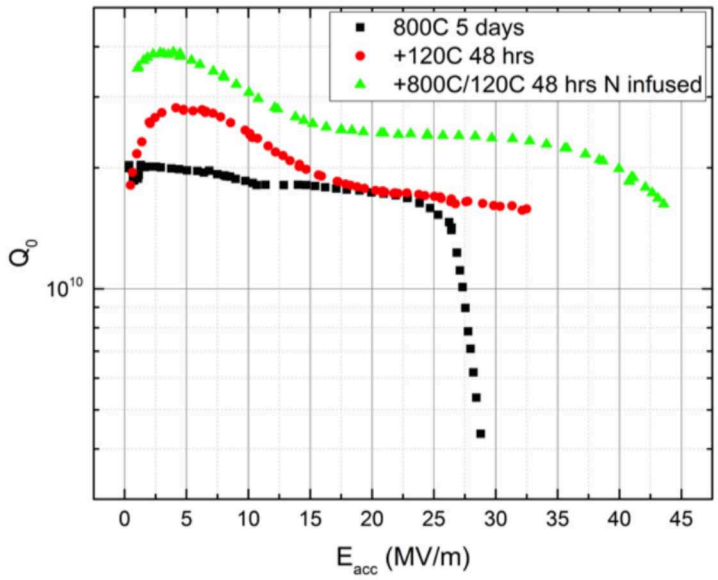

Figure 29: Q_0 vs. E_{acc} comparison between nitrogen infusion and standard EP-treated cavities from [5].

4.3 Motivation for a dedicated sample study

The London penetration depth for niobium at absolute zero has been measured in [86] to be $\lambda_L(0) = 39 \pm 5$ nm. This means the field actually only just penetrates the surface and the very first few Angstroms or even fraction of an Angstrom of the surface are the most important. The inner cavity surface is the crucial factor determining the surface resistance and thereby the cavity performance. Fabricated cavities are unlikely to consist of a perfect single-crystal niobium lattice. Instead grain boundaries, mechanical stresses leading to inhomogeneties, impurities and interstitials all contribute to the resulting performance. Particle contamination on the surface can lead to field emission. During the cooldown of a cavity, dissolved hydrogen can precipitate in hydrides which can even deform the niobium lattice and leave "scars" on the surface. Normal conducting inclusions, hydrides, oxides, and trapped magnetic flux have all been demonstrated to contribute to the residual resistance [1]. On all of these effects, a treatment such as the nitrogen enrichment of the surface might have an impact, causing the observed performance improvement. Since it is difficult to do surface analysis on the cavity inner surface without destroying the cavity, sample studies might be the most appropriate choice to disentangle the effect of nitrogen on these factors. With OBACHT for example, a optical inspection robot developed at DESY and KEK [87], macroscopic defects can be analysed but microscopic modifications stay hidden. Samples and cavities can be treated identically, being processed simultaneously within the same vessel, although the comparability between sample and cavity still needs to be treated with caution as the material history might be slightly different. The surface area of a TESLA-shaped [34] single-cell cavity is approximately $A_{cavity} = 970$ cm^2, which is very different to a typical sample surface area of about $A_{sample} = 0.5$ cm^2. A cavity performance test will be determined by its complete surface and will in principle be a value which indicates how "good" the complete surface is on average i.e. macroscopic defects will also play a role. That is why only microscopic behavior between samples and cavities can be compared if treated together. However, pre-surface treatments such as for example electropolishing will change the crystallographic appearance and physical properties depending on many factors. With samples, a closer look at individual effects can be taken and one parameter after another investigated. This requires good planning as sample preparation, actual treatment and subsequent analysis are time consuming.
The specification of an excellent recipe for nitrogen enrichment of cavities requires a good understanding of what exactly its effect on the cavity is. How much nitrogen actually diffuses into the niobium lattice depends on several factors, including the temperature and diffusion time, the texture and purity of the surface. Some measurement techniques to determine this will be presented in the next chapters.

4.4 Nitrogen diffusion in niobium

Several different measurement techniques to characterize the chemical composition of surfaces exist. We would like to find the exact concentration and depth of interstitial nitrogen of our niobium samples after treatment. The Arrhenius equation gives a temperature-dependent diffusion coefficient for nitrogen atoms in bcc Nb,

$$D(T) = D_0 \cdot e^{\frac{-E_a}{kT}}, \tag{9}$$

where $D_0 = 0.063\ \frac{\text{cm}^2}{\text{s}}$ is the diffusion constant, $E_a = 1.66796$ eV the activation energy [88] and k the Boltzmann constant. The parameters D_0 and E_a are also called the diffusion activation parameters. Applying Ficks Law [89] to eq. 9 gives a diffusion depth from the surface as

$$l = 2\sqrt{Dt}. \tag{10}$$

The depth at a temperature range of 120°C to 500°C is plotted in Fig. 30. At a temperature

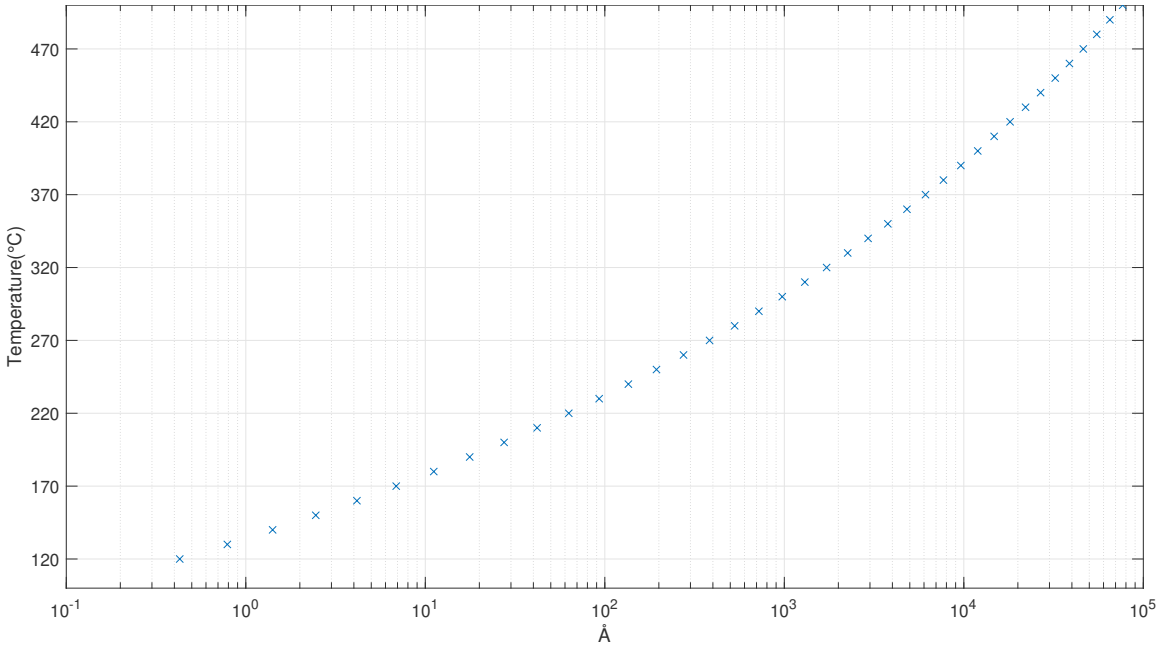

Figure 30: Temperature against diffusion depth from the surface of nitrogen in bcc Nb calculated by eq. 9 for 48h with $D_0 = 0.063\ \frac{\text{cm}^2}{\text{s}}$ and $E_a = 1.66796$ eV [88].

of 120°C, Fick's Law predicts a diffusion depth of 0.43 Å. Temperatures such as 120°C seem therefore to be too low to let any nitrogen diffuse into the niobium lattice to make a significant solid solution.
The kinematics for nitrogen diffusion in niobium have been studied with many different methods and temperature ranges. Measurements on diffusion coefficients must have been influenced by the natural oxide layers and at high temperature by the growth of precipitates that have not always been taken into account. The temperature dependence of diffusion coefficients was found to obey the Arrhenius formula in only a few cases [88]. Microstructual features such as dislocations, grain boundaries or effects associated with impurities can lead to significant deviations. Furthermore, this calculation is a rough estimate, and any dependence on D_0 is of minor importance as Eq. 9 depends linearly on it. However, the activation energy is exponentiated and therefore needs to be known to high accuracy to make useful estimates. It is known that niobium grows an oxide layer on top of the surface when exposed to air, as shown in the simplified schematic in Fig. 31.
According to [90], the thickness of the niobium-oxide layers usually does not exceed a few nanometers. The passivating Nb_2O_5 layer makes it more difficult for nitrogen to diffuse

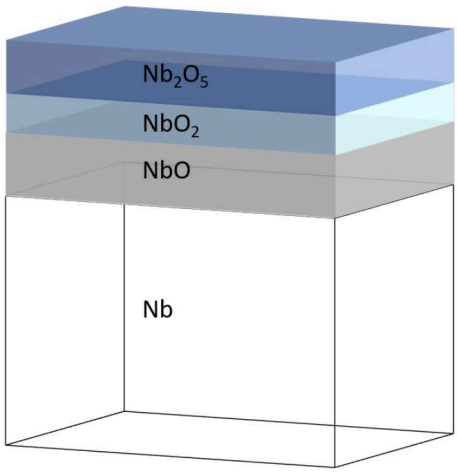

Figure 31: Simplified schematic view of oxide layers on niobium surface which are naturally present if exposed in air.

into the bulk as it acts as a diffusion barrier. It has been shown in previous work [91] [92] [93] [94] [95] [96] [97] [98] that the naturally occurring pentoxide, dioxide and monoxide components start to decompose at certain temperatures so that

$$Nb_2O_5 \rightarrow NbO_2 \rightarrow NbO. \tag{11}$$

Reaching 800°C as in the nitrogen-doping or infusion recipe should reduce the niobium pentoxide and niobium dioxide at least, leaving a thinner niobium monoxide layer. Exactly how much of the oxides remain on the surface at 800°C is still controversial and under investigation. However, an important fact is that NbO is not passivating and thus does not act as a diffusion barrier [99]. This could explain why the pre-annealing step at 800°C is necessary in the case of nitrogen infusion.

5 RRR measurements on cavities and samples

5.1 Motivation

It has long been known that the RRR value is an important parameter because it is related to the level of contamination, as discussed in sec. 1.6. For a long time, it was assumed that high-purity niobium with the highest possible RRR would be best, since there is a direct relationship between RRR and thermal conductivity, as shown in eq. 8 from sec. 1.6. The theoretical limit for the RRR of niobium is 32000 [1]. As already mentioned in sec. 1.6, the European XFEL specification had a value of 300 during production, which is a realistically achievable value for fine-grained material. In the past, studies have been carried out on large-grained material which can have an average RRR value of around 500. Large-grain niobium cavities also performed better on average [100] [101]. Light impurities such as O, C, N, H can be influenced by heat treatments and chemical treatments such as BCP and EP. Because of its high affinity for Nb, oxygen is the most dominant.
However, surface treatments such as nitrogen doping and infusion show that impurities caused in a controlled manner, a few nm to μm below the surface, can lead to an improvement in performance. Whether this is also noticeable in the RRR parameter is the topic of this chapter.
There are two known techniques to determine the RRR value. One is the eddy-current method, which was developed to carry out measurements directly on cavities. This method does not require physical contact with the material, which is why it is considered non-destructive. The other method is based on a resistive measurement via a direct standard 4-pt contact. Although this method promises significantly higher measurement accuracy, damage to the sample surface is inevitable.

5.2 RRR eddy-current setup

Non-destructive measurement of the RRR of the cavity material can be achieved by using AC eddy currents produced by a coil. If a normal-conducting metal is placed in an AC magnetic field with frequency f, an eddy current with a penetration depth of

$$\delta = 1/\sqrt{\pi\mu\sigma f}$$

is induced, where σ is the conductivity and μ the permeability. This is also known as the skin effect. The eddy-current density decreases with distance from the coil that produces the AC magnetic field, reaching $1/e \approx (37\%)$ of the surface density at the penetration depth δ. The eddy currents flowing in the metal induce magnetic fields that oppose the primary fields. Measuring the back-induced magnetic field allows the RRR value to be measured non-destructively. The illustration of an eddy current is shown in Fig. 32. A measurement probe consists of a primary coil as a source of the AC magnetic field, a pickup coil that detects the back-induced field from the eddy current and a backing coil that compensates the signal from the primary coil. The primary coil sits on top of the pickup coil as shown in Fig. 33 (a) and consists of a small solenoid magnet with 50 windings. The compensation coil is similar to the pickup coil but with opposite voltage to eliminate the signal induced by the primary coil in the pickup coil. As shown in Fig. 33 (b), the pickup coil is a one-layer pancake coil. The setup consists of 9 sensor probes in total, where 3 sensors are

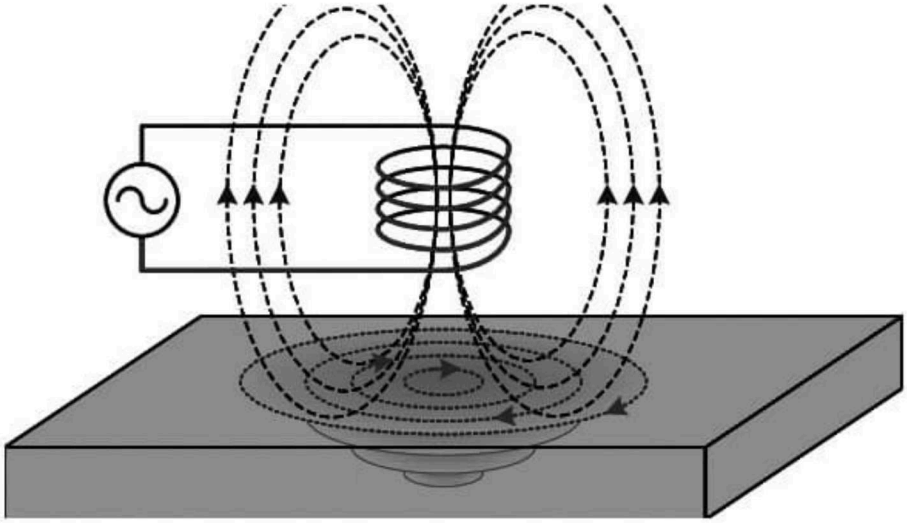

Figure 32: Eddy currents induced in a metal by alternating-fields.

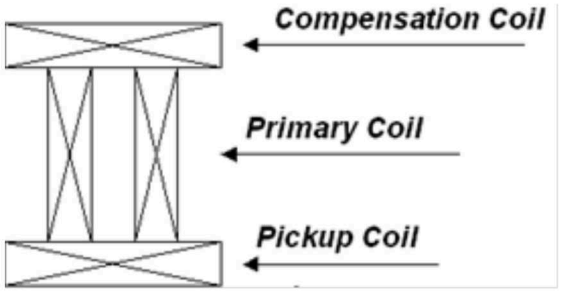

(a) Sketch of the RRR coil probe structure.

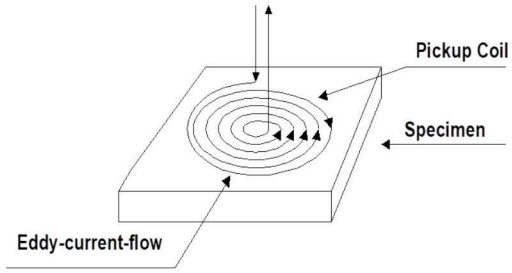

(b) Pickup coil stucture which is a one-layer pancake-shape coil.

Figure 33: RRR coil structure [52].

packed in one holder as shown in Fig. 34 (a). It is complicated to express the dependence of the eddy current on the sample resistivity, as it depends on the probe structure, the sample shape and the distance between coils and samples. Instead, the relative jump from the pickup voltage in the transition between normal and superconducting i.e. at T_c, is used to estimate the RRR value as discussed below and shown in Eq. 12. The measured temperature dependence of the pickup voltage is shown as an example in Fig. 35 (a) with the voltage jump U_j from superconducting to normal state. The sensors used here have been calibrated earlier with the calibration curve taken from [52] shown in Fig. 35 (b). The accuracy is reduced with increasing RRR values because the slope flattens, which becomes a significant effect for values of RRR > 500. Several factors have to be taken into account in assessing the measurement accuracy of the RRR setup. The cool-down or warm-up speed

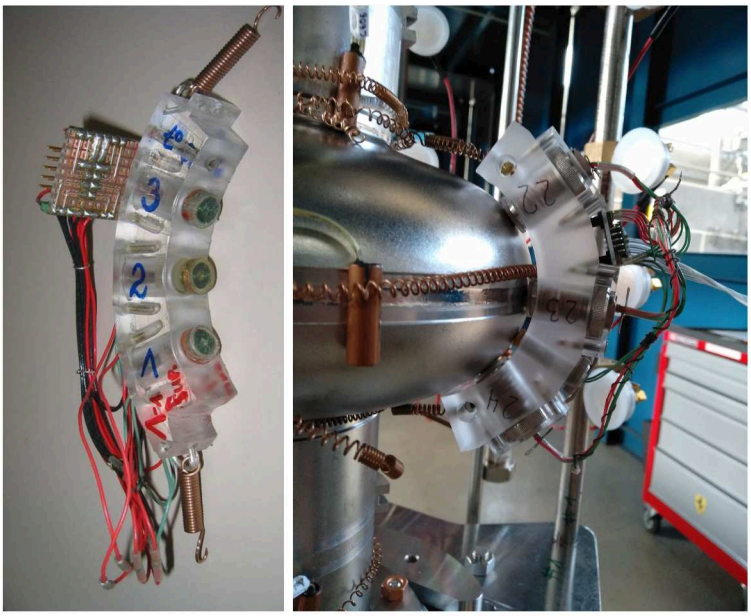

(a) RRR sensor holder.

(b) Attached RRR eddy current sensors on a single-cell cavity.

Figure 34: Photographs of eddy-current RRR sensor holders designed to measure the RRR on niobium SRF cavities.

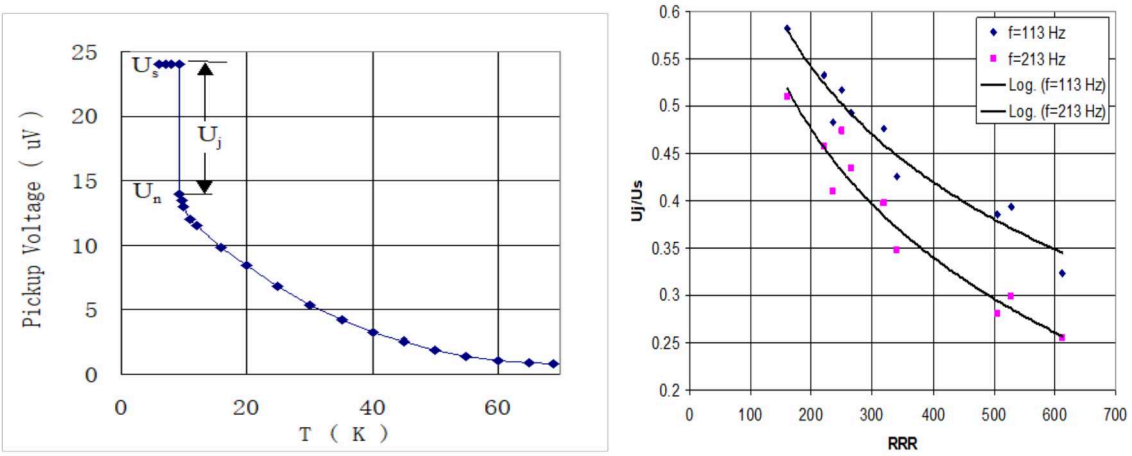

(a) Example curve of measured Pickup voltage vs temperature.

(b) Measured curve for U_j/U_s vs RRR with 10 samples for two different frequencies. The curve for $f = 213$ Hz is used for calbration for our RRR sensors.

Figure 35: Pickup voltage and calibration curves for the RRR sensors taken from [52].

and homogeneity across T_c influences the accuracy with which the jump can be measured, depending on the sampling rate of the DAQ. Due to the low readout frequency and transient

time when switching between coils, a slower temperature change at around T_c is necessary to increase the measurement accuracy of the jump. The readout time between two data points for the pickup voltage is approximate 27 seconds. Figure 34 (b) shows a photograph of how the RRR sensors are attached to a single-cell cavity. The middle sensor sits on the equator weld, which makes an optimal contact between the sensor coil and the cavity difficult. The RRR holder design was intended for 9 cells which have stiffening rings for stabilization of the complete structure. Therefore cable ties were used to attach the holders to single-cell cavities. This might have a detrimental influence on the results as it means that the coils cannot always be in optimal contact with the surface. In reference [52], the influence of the distance between probe and cavity surface has been investigated and shown to have a strong effect on the accuracy. The sensitivity of the RRR measurement has been determined to be about 5% for changes in distance of around 0.2 mm. Therefore, careful installation of the holders is essential, especially for single cells. Figure 36 shows a typical signal from a measurement on a single-cell cavity. The temperature is measured by a Cernox® sensor that is attached to the cavity. Three temperature sensors were installed: (i) one at the iris above the equator (top iris), (ii) one at the iris below the equator (bottom iris) and one at the equator of the single cell. The temperature data shown in Fig. 36 is from the sensor installed at the equator, as this is spatially the closest one to the RRR holder. The real and imaginary parts of the complex signal are referred to as U^x and U^y, respectively. The quantities $U_n^{x,y}$ and $U_s^{x,y}$ are measured directly at the voltage jump where the transition from normal to superconducting or vice-versa happens, depending on whether a cool-down or warm-up through T_c is measured. Furthermore, the signals U_0 at room temperature are collected and subtracted from the measured signal. The quantity

$$\frac{U_j}{U_s} = \frac{\sqrt{(U_s^x - U_n^x)^2 + (U_s^y - U_n^y)^2}}{\sqrt{(U_s^x - U_0^x)^2 + (U_s^y - U_0^y)^2}},$$

determines the RRR value as

$$RRR = e^{\left(\frac{U_j/U_s - a}{b}\right)}, \tag{12}$$

where a and b are calibration parameters taken from Fig. 35 (b).

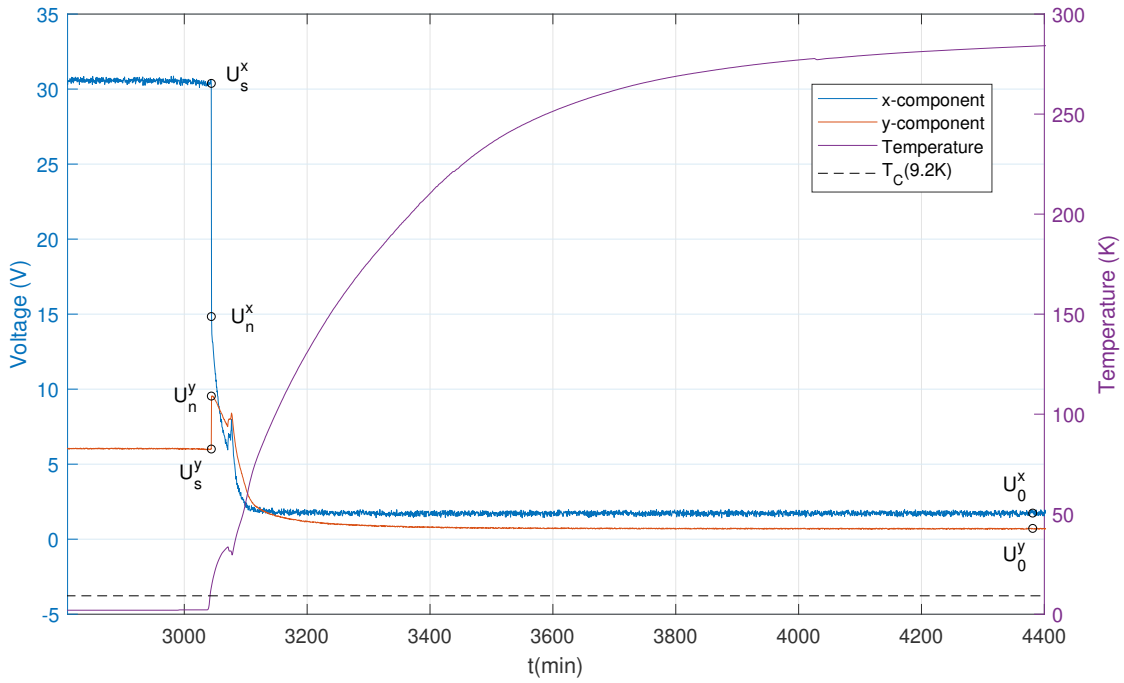

Figure 36: Voltage (left vertical axis) and temperature (right axis) vs time from RRR eddy current sensors. The temperature is measured by a Cernox® sensor attached at the equator of the single-cell cavity.

5.2.1 RRR eddy-current measurements on single-cell cavity

The RRR eddy-current measurement of a single-cell cavity before and after a nitrogen infusion at 120°C is shown for each sensor in Fig. 37. The coils are attached as shown in Fig. 34 (b). Neglecting sensor 1 and 2 due to signal interference in the measurement,

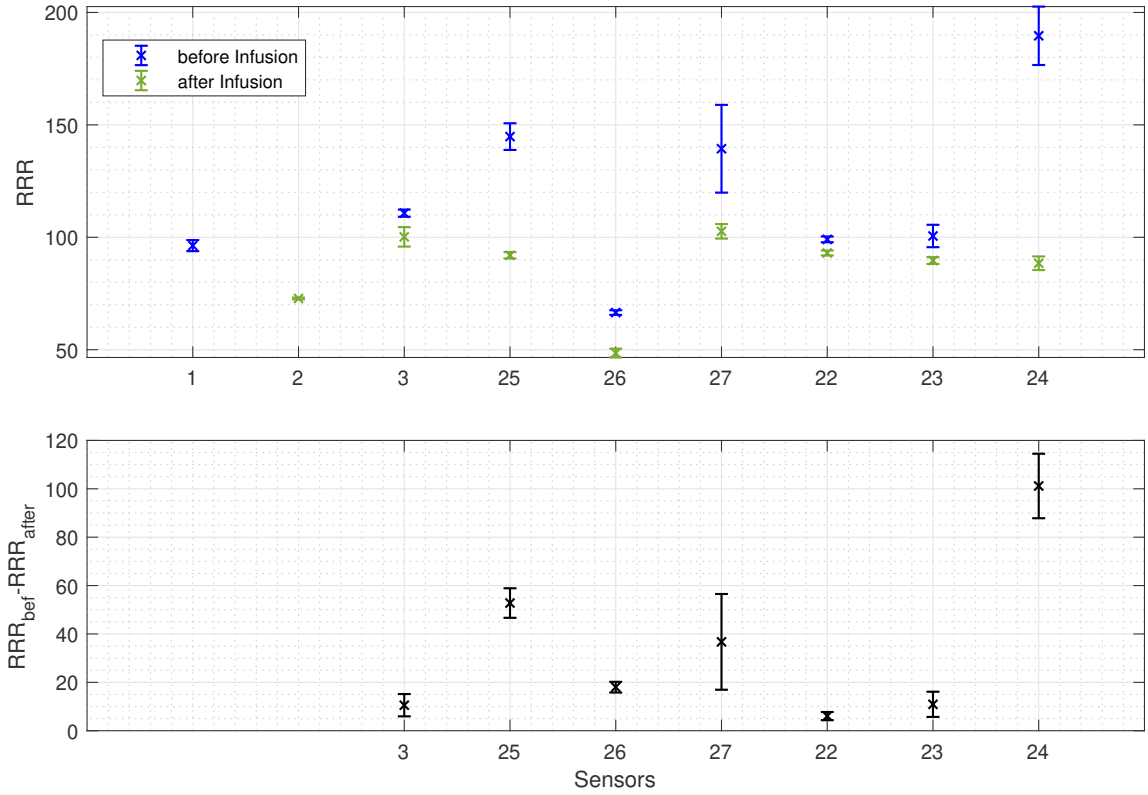

Figure 37: Measured RRR values on a single cell cavity before and after a nitrogen infusion by AC eddy current. The values are averaged over several temperature cycles. Due signal interference one of the data points for sensor 1 and 2 is missing for each measurement. The relative difference between before and fter treatment is shown in the bottom. They are in reasonable agreement except for sensors 25 and 24.

an average decrease for the RRR after the Infusion treatment of $\Delta\text{RRR} = -34 \pm 12$ is observed. The average value before the Infusion is $\text{RRR}_{bef} = 118 \pm 13$ and after the Infusion $\text{RRR}_{after} = 86 \pm 6$. The values differ significantly from the European XFEL specification value of about 300. This indicates that a re-calibration of the sensors was required since the cavity was made from RRR $\sim$ 300 material. This issue is discussed further in the next section about RRR measurements on samples. The cavity performance before and after a nitrogen infusion treatment is shown in Fig. 38. The performance decreased after about 20 MV/m after the treatment. As further reviewed in sec. 7.2, carbide precipitation occurred on witness samples during this run and are suspected to be the cause for the suppression of

any performance enhancement.

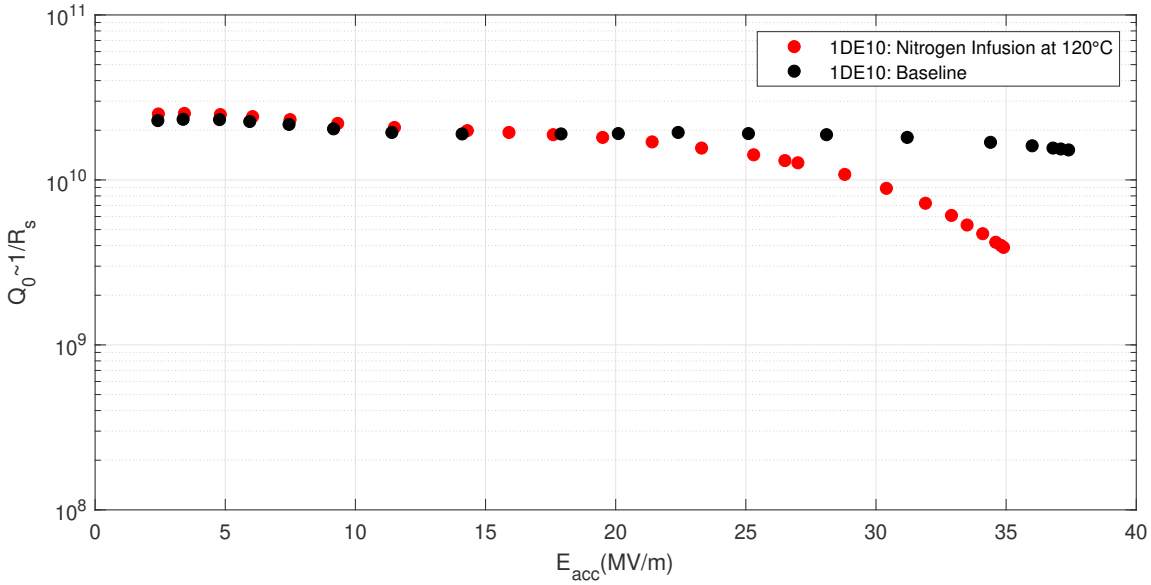

Figure 38: Cavity performance after a nitrogen infusion at 120°C. The performance before the nitrogen infusion is shown in the baseline curve in black. A deterioration in the performance beyond about 20 MV/m is observed. The cavity performance did not change for low fields.

5.2.2 RRR eddy-current measurements on samples

To assess if a calibration is necessary, it was decided to do several measurements with samples with known RRR for different cool downs and warm ups and calculate the RRR for each. The RRR was measured via the 4-pt contact method for three cylindrical samples with a diameter of 10 mm and a thickness of 2.8 mm. (The 4-pt contact method will be discussed in detail in section 5.3.) The samples were then measured with three of the RRR eddy-current sensors i.e. one holder, by attaching them as shown in Fig. 39. Several measurements were

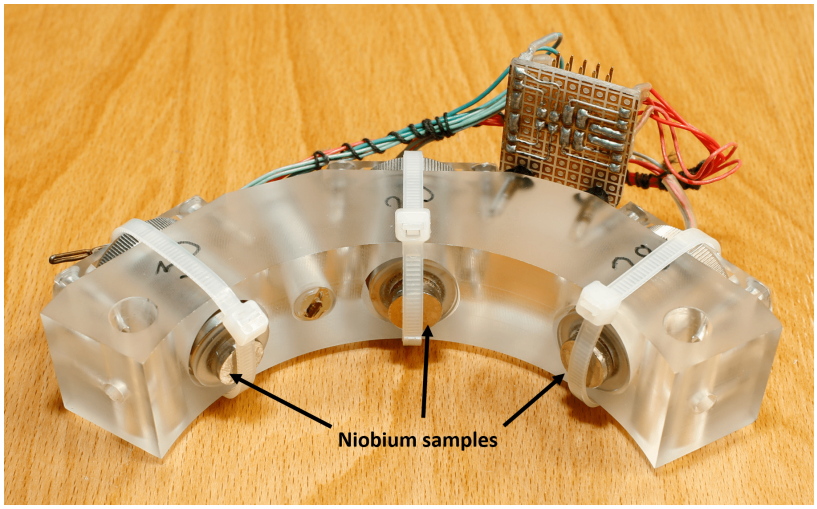

Figure 39: Three niobium samples with known RRR attached to the sensors.

done over a few cool-down and warm-up cycles through T_c, which were repeated after the samples were swapped so that each was measured on all three sensors in this holder. As examples, the measured voltage from the middle sensor where the sample with a RRR = 371 was placed is shown in Fig. 40. The voltage jumps as the temperature cycles through T_c are clearly visible. The results for the three circular samples are shown in table 3, where the

Sample	**4-pt**	**Sensor 30**	**Sensor 29**	**Sensor 28**
1	371	120 ± 5	169 ± 4	202 ± 4
2	149	39.3 ± 2.9	64 ± 8	78.4 ± 2.2
3	158	40.5 ± 1.9	78 ± 6	88.4 ± 0.5

Table 3: RRR(at 9.2 K) values of circular samples measured by AC eddy current compared to known values from the 4-pt method. The values are averaged over the results from several temperature cycles through T_c as is shown for example in Fig. 40. The errors are estimated confidence intervals with 68% confidence level.

RRR value measured from the 4-pt contact method (not extrapolated to 4.2 K) is shown next to the AC eddy current averaged over the results from several temperature cycles. From these values the sensors were re-calibrated by plotting U_j/U_s vs RRR measured by 4-pt and do a fit as shown in Fig. 41. The newly obtained calibration parameters were tested

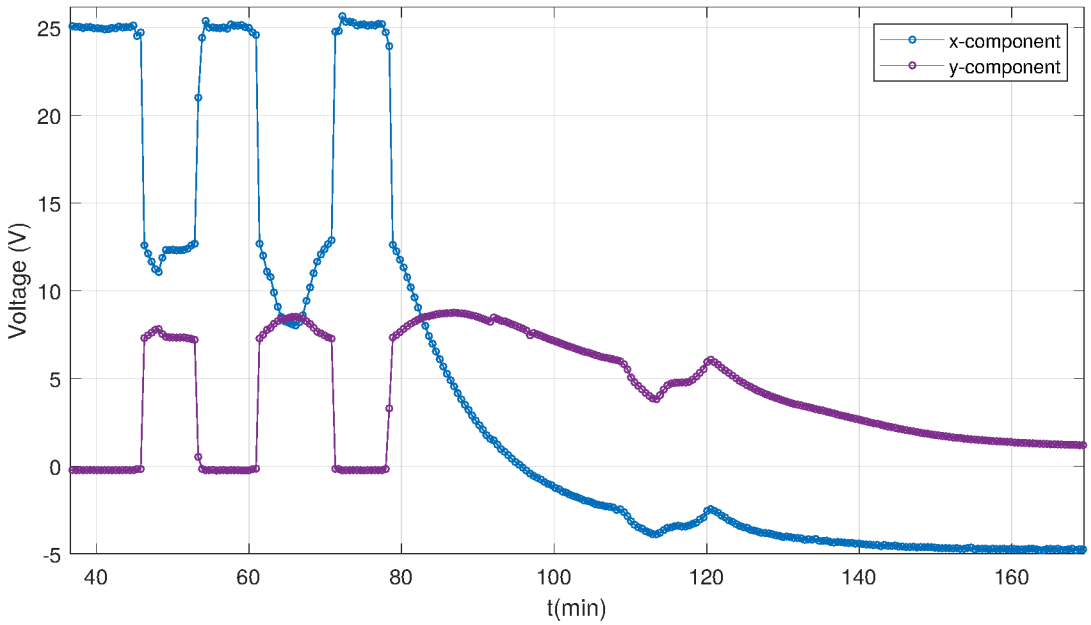

Figure 40: Measured voltage vs time from RRR eddy-current sensors (circles).

on three large-grain samples on which the RRR has been also measured by the 4-pt method in advance. The results are given in table 4. On average the values deviate about $\sim 7\%$

	RRR(4-pt)	**RRR(old calibration)**	**RRR(new calibration)**
Sensor 28	451	228	420 ± 50
Sensor 29	481	233	510 ± 130
Sensor 30	432	130	402 ± 15

Table 4: This table shows a re-calibration. Shown are RRR (at 9.2 K) values from three circular large-grain samples measured by the 4-pt and AC eddy-current methods calculated with the old calibration curve shown in Fig. 35 (b) and with the curve obtained from our samples shown in Fig. 41 for comparison.

from the 4-pt measurement with the new calibration parameters while the old calibration parameters gave about $\sim 59\%$ deviation. While only three samples with known RRR have been used to re-calibrate for demonstration purposes here, more samples would increase the calibration accuracy. These results show that a new calibration of all sensors is needed but a relative comparison between measurements of the same sensors can be applied. The data points in Fig. 40 indicate that the sampling rate was sufficient for the applied temperature gradient, since the rise and fall is sampled by several data points. However, if only one jump is measured, as in Fig. 36, a high temperature gradient across T_c can influence the accuracy. One more example where the temperature cycling was done explicitly close to T_c is shown in Fig. 42, where differences in the jump heights can be seen. In order to use the system for systematic studies, it is mandatory to reduce the number of sensors or redesign the DAQ

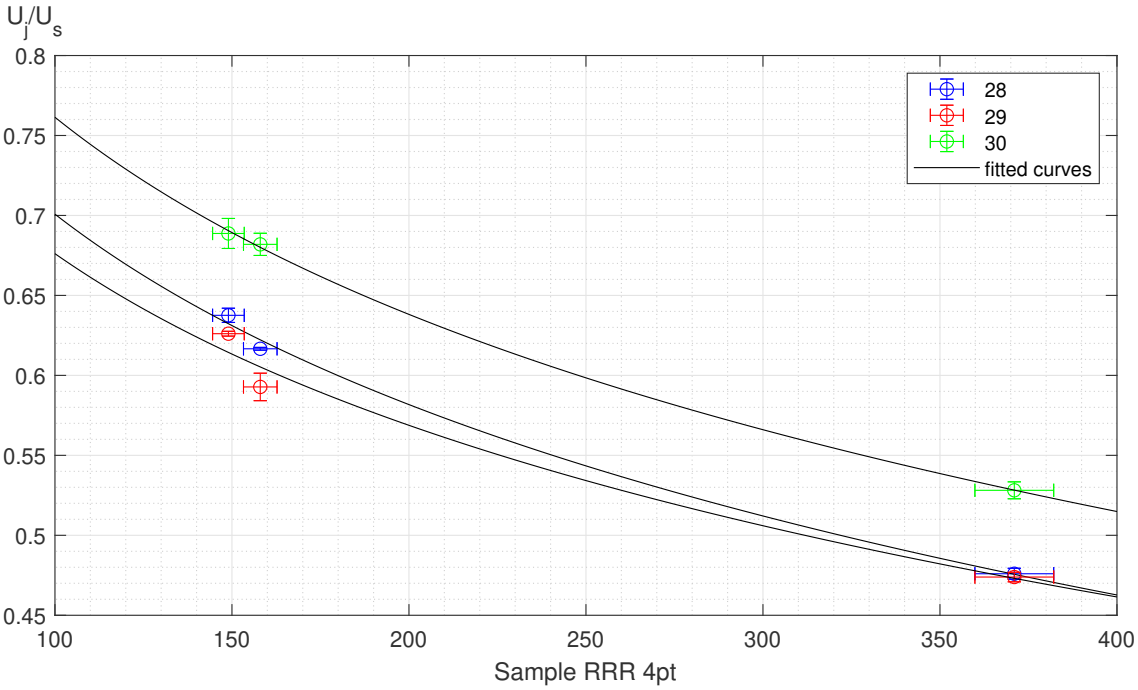

Figure 41: U_j/U_s values measured by AC eddy current with sensor number 28, 29 and 30 averaged over several temperature cycles vs RRR measured by 4 pt contact method on samples.

system to remove the to switch between the coils. In addition, to reduce any uncertainties regarding the alignment, sensor holders for single-cell cavities have to be built. The samples used here are just slightly bigger in diameter then the pickup coils. Therefore it is not clear that all the field passes through the sample or whether some is lost around the edges. For the calibration via samples with known RRR, the size should be increased to provide the same conditions as on cavities.
Whether the RRR sensors cause flux trapping during cavity measurements or not has been tested on one cavity. The Q_0 vs. E_{acc} curve has been measured while the coils were turned off i.e. with magnetic field absent and another measurement was done while they were turned on i.e. a magnetic field from the coils was present. The result is shown in Fig. 43. The cavity performance is more influenced by trapped flux at lower temperatures. Measurements at 2 K and 1.8 K show a higher loss in Q_0 at the lower temperature, indicating that flux is trapped from the RRR sensors. It is therefore advisable to deactivate the RRR coils during the cooldown and performance testing. For further investigations of the influence of nitrogen treatments on the RRR value of samples, a different method was chosen which promises a higher measurement accuracy and has long been established in the quality control of niobium. The next section is concerned with this method and its results on niobium samples.

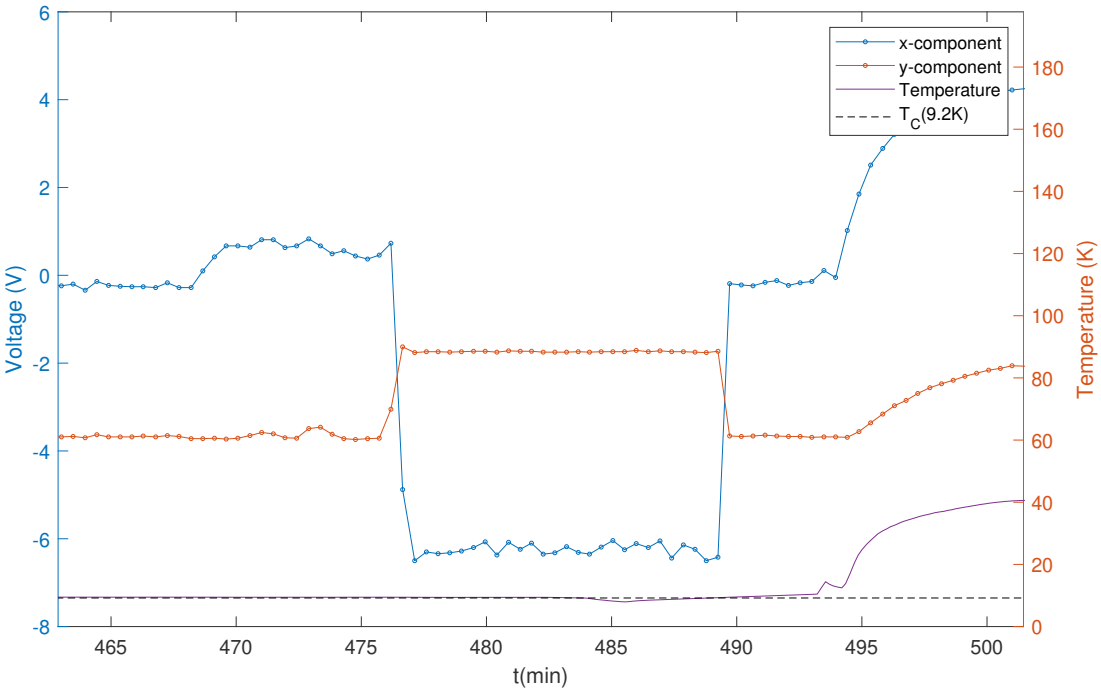

Figure 42: Voltage (left vertical axis) and temperature (right axis) vs time from RRR eddy current sensors. The temperature is measured by a Cernox® sensor attached at the equator of the single-cell cavity.

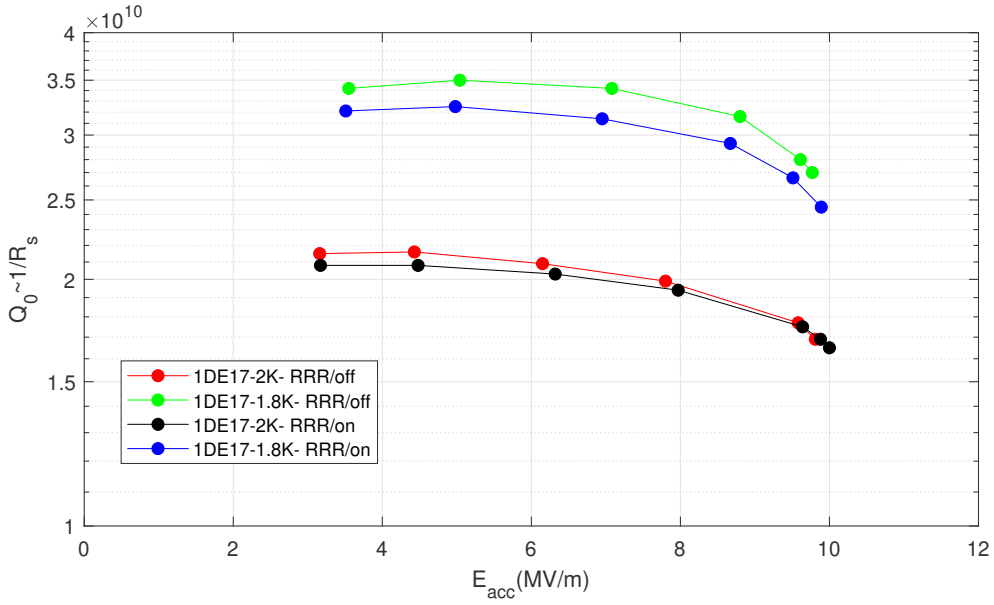

Figure 43: Performance of cavity 1DE17 with attached RRR AC eddy-current sensors turned on and off. A reduction in quality factor is observed after the RRR coils have been switched on. This is more prononuced for the performance measurement at 1.8 K, indicating that the reduction is caused by trapped flux generated from the RRR coils.

5.3 RRR 4-pt contact method

A DC RRR measurement system was created at DESY and served as an important tool for niobium quality control. This method is based on a four-wire sensing technique, which enables the measurement of very small resistances, since the effects of the contact resistance are minimized. A known current I flows through the sample via the two outer lines shown in Fig. 44. The voltage U across the sample is tapped via the two inner lines. The resistance of the sample can be calculated using Ohm's law. Only a negligible current flows through the voltmeter. For the subsequent measurements, a current of 1 A is used. The sample holder

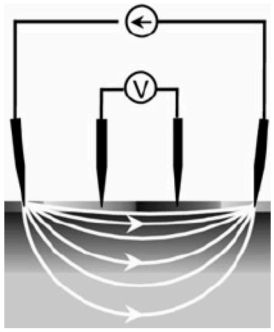

Figure 44: Illustrative principle of the 4-pt contact method [102].

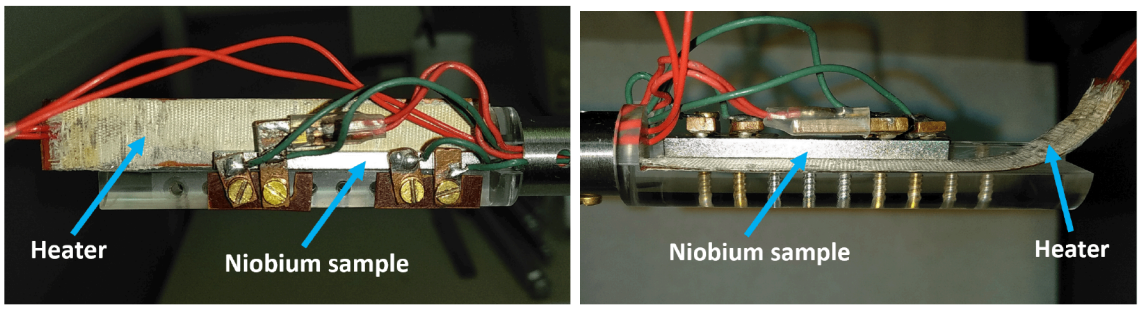

(a) Topview (b) Sideview

Figure 45: Photograph of sample holder for RRR measurement via 4-pt contact method.

that was used in the following experiments is shown in Fig. 45. A niobium sample is clamped in, the 4 contacts, which are copper coated with silver are screwed tight from above. The warm-up and cool-down procedure is performed by immersing the sample into liquid helium. The temperature is controlled using Cernox temperature sensors. The thermoelectric voltage that occurs as a result of a temperature gradient along the sample can be very critical. As a result, the temperature gradient must be minimized. The temperature dependence of resistivity is measured by slowly heating a sample clamped on a thin-film flexible resistive heater as shown in Fig. 45. The temperature deviations during the heating or cooling of the sample are very small, allowing precise determination of the superconducting jump point.

The sample's resistivity is measured above T_c and very close to it as shown for one of the sample measurements in Fig. 46. The voltage at the intersection between the lines

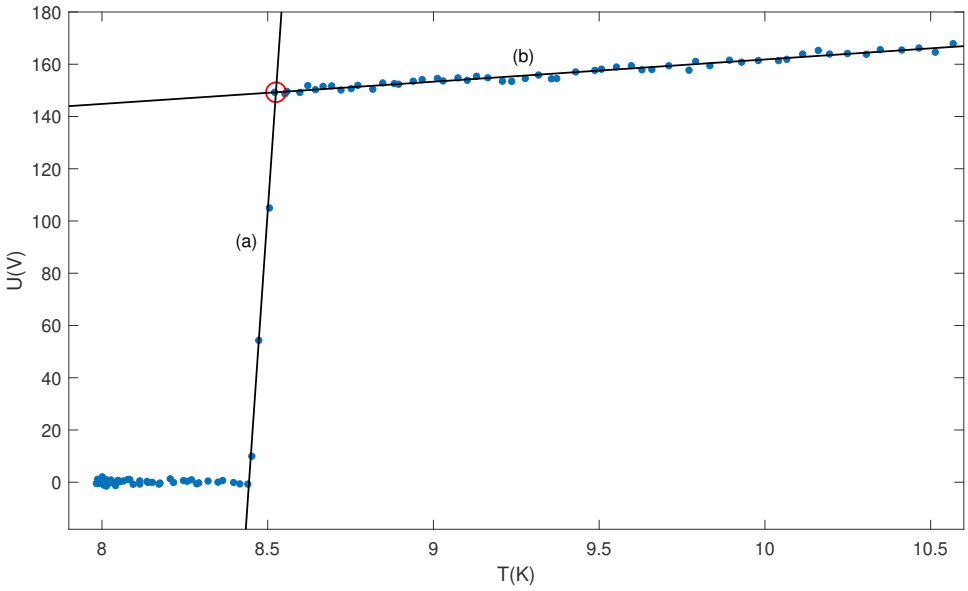

Figure 46: Data (voltage vs. temperature) from resistivity measurement of one sample and the two fitted lines (a) and (b) to determine the intersection marked by the red circle giving $U(T_c)$. The error bars are smaller than the symbol size.

(a) and (b) gives $U(T_c)$. For Nb, T_c is 9.2 K but appears to be lower here because there is a temperature gradient between the sample and the sensor. Figure 47 shows the whole temperature range up to room temperature. The voltage is extrapolated to 295 K using a cubic polynomial. Since $\rho = U/I$ it follows by $\mathrm{RRR} = \rho(295\ \mathrm{K})/\rho(T_c)$ that the RRR at T_c by

$$\mathrm{RRR}_{9.2\mathrm{K}} = \frac{U(295\ \mathrm{K})}{U(T_c \approx 9.2\ \mathrm{K})}$$

can be determined. The accuracy of this measurement depends mainly on the accuracy in determining the intersection that is shown in Fig. 46. The voltage is measured by a Keithley Digital-Multimeter with a precision of about 1 nV and has a magnitude of about 2 mV achieved by using a pre-amplifier and a polarity-reversal device. The total error thus consists of the resolution on the voltage measurement combined in quadrature with the error estimated from the temperature determination. It has conclusively been shown in [52] that the total systematic and absolute accuracy including that which can be attributed to variations caused by assembling and disassembling the samples is in the range of 2-3%.
As mentioned in sec. 1.6, the T_c of niobium is higher than the liquid-helium temperature 4.2 K on which the RRR is usually defined (see eq. 7). Therefore, the value $\mathrm{RRR}_{9.2\mathrm{K}}$ is extrapolated linearly to $\mathrm{RRR}_{4.2\mathrm{K}}$. However, since this introduces an additional uncertainty the RRR values of the samples measured here are compared at the measured temperature.

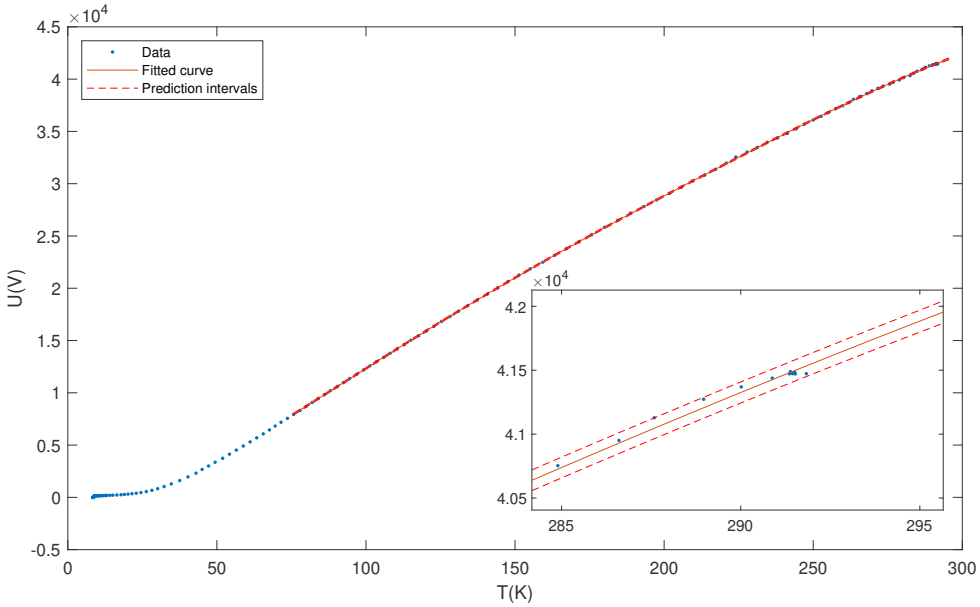

Figure 47: Data (voltage vs. temperature) from resistivity measurement of one sample from room temperature to below T_c. The error bars are smaller than the symbol size. The cubic polynomial is shown in red extrapolated to 295 K with 95% prediction intervals.

5.3.1 RRR 4-pt measurement on niobium fine-grain samples

Since the 4-pt method represents a more precise measurement compared to the eddy-current method, it was selected to investigate the influence of nitrogen infusion on the RRR value of samples. For the sample geometry, rectangular instead of cylindrical samples were used as shown in Fig. 45. A total of ten fine-grain niobium samples, 5 of which were subjected to a nitrogen infusion in a temperature range between 120°C and 400°C, were measured. A temperature cycle was carried out, ramping up to 800°C for 3 hours under vacuum conditions, subsequently brought down to the desired temperature (120°C - 400°C) for 48 hours, during which nitrogen is introduced. It is assumed that no nitrides are formed up to 500°C, in a pure nitrogen atmosphere at 500°C as was the case in [95]. However, the pre-annealing step at 800°C was omitted and a niobium single crystal (Nb100) was used to obtain these results.
Since some theories explain the characteristics of N-Doping by postulating an α-Nb(N) solid solution, i.e. in purely interstitial dissolved nitrogen in niobium, a maximum temperature of 400°C was used to avoid any Nitrogen precipitation. As will be discussed in sec. 6, no typically $\beta - Nb_2N$-shaped precipitates (nitrides) were observed with the SEM on samples that were treated with a nitrogen infusion temperature of 400°C.
The remaining 5 samples were subjected to the same temperature treatment, but without nitrogen, i.e. under vacuum conditions. This method measures the bulk, but if the accuracy is sufficient, information about the surface properties can be obtained. A comparison with

the sample without introduced nitrogen represents the contribution from other residual gases that have penetrated the material or diffused out of the bulk. An RGA spectrum was recorded during the 120°C infusion and was shown in sec. 3.2 in Fig. 22 and 23 to show the condition of the furnace and nitrogen line. During the treatment, a small niobium box (shown in sec. 7.2.4 in Fig. 73) was used to cover the samples. The box serves to protect the sample surface against line-of-sight particles from the oven walls. The niobium box received a BCP(see sec. 2.1.1) and was pre-fired to 1000°C in vacuum conditions. The benefits from that are discussed in sec. 7.2.4.
A sample that was infused with nitrogen at 400°C shows neither carbides nor nitrides, which on the one hand demonstrates that the oven is clean and on the other confirms the assumption that no nitrides are formed at 400°C. From the diffusion coefficient eq. 9 for nitrogen atoms in niobium, a diffusion depth from the surface of $\approx$ 1491 nm would be expected from 48h of treatment at 400°C. With a sample volume of $(2.88 \cdot 3 \cdot 42)$ mm^3, the nitrogen-enriched volume is therefore $\approx 0.2\%$ of the total volume. If the RRR measurement accuracy as discussed in the previous section is maintained, a significant difference due to the nitrogen treatment might be observed. Detailed process steps of sample preparation with subsequent measurement and treatment sequence are discussed in the following section.

5.3.2 Sample preparation and treatment sequence

The samples are fine-grain samples made of niobium from the manufacturer Tokyo Denkai which were cut to a size of $(2.88 \cdot 3 \cdot 42)$ mm^3. The first step in this process was to BCP the samples for 20 minutes to remove the damage layer on the surface and remove any remaining residue. They were then cleaned in an ultrasonic bath and rinsed with deionized water. Two of the samples were measured at this preparation step in order to establish a reference value for any further treatment and how much the RRR value possibly changes when baking at 800°C. A large change in the RRR value after 800°C baking would indicate contamination in the oven. The next step was to bake at 800°C in a vacuum ($\sim 10^{-7}$mbar) for 3 hours in the sample furnace, whose condition is described in more detail in chapter 3.2. The two samples that were measured before baking were now measured again. The results for these two samples are shown in table 5. The RRR value before and after the 800°C treatment remained unchanged within the measurement uncertainty. Furthermore, the RRR for the remaining samples were also measured at this point. To clean the surface, the samples were then treated again with a short BCP of about 2 minutes, cleaned in an ultrasonic bath and rinsed with deionized water. The samples were then treated with the baking cycle described above, five samples each in vacuum conditions and five with a nitrogen atmosphere ($3.3 \cdot 10^{-2}$ mbar) at the infusion temperature after the pause at 800°C. The results are presented next. According to the work of [103], no significant changes in the RRR value for samples with RRR $\sim$ 300 were measured after several etching processes of different lengths via BCP. The changes were a little more noticeable for samples with RRR $\sim$ 500. In this case, the changes are sufficiently low if not more than 2 μm of material is removed with a BCP of 2 minutes.

Sample No.	**RRR(before 800°C)**	**RRR(after 800°C)**	**ΔRRR**
1	275 ± 6	281 ± 5	5 ± 7
2	288 ± 6	293 ± 6	5 ± 8

Table 5: RRR(at 9.2 K) values from two fine grain samples measured by the 4-pt method. Errors are 68% confidence level.

5.3.3 Results

The results from the RRR measurements are summarized in table 6. The change in RRR

Sample No.	Inf T	RRR(initial)	RRR(after)	ΔRRR
3	400°C w N	295 ± 4	252 ± 4	-43 ± 5
4	330°C w N	296 ± 4	247.4 ± 2.6	-48 ± 5
5	260°C w N	289 ± 5	238.6 ± 2.9	-50 ± 6
6	160°C w N	296 ± 8	259 ± 5	-37 ± 9
2	120°C w N	293 ± 6	265.7 ± 1.9	-28 ± 6
8	400°C no N	304 ± 6	274 ± 5	-30 ± 8
9	330°C no N	288 ± 5	253 ± 6	-34 ± 8
10	260°C no N	293 ± 7	256 ± 5	-37 ± 9
11	160°C no N	292 ± 6	256 ± 5	-36 ± 7
1	120°C no N	281 ± 5	248 ± 4	-32 ± 6

Table 6: RRR(at 9.2 K) values from fine-grain samples measured by the 4-pt method. The infusion temperature denoted as "Inf T" is the temperature subsequently reached after a hold at 800°C for 3 hours under vacuum conditions. Errors are 68% confidence level.

before and after the infusion heat treatment is denoted as $\Delta\text{RRR} = \text{RRR}_{\text{after}} - \text{RRR}_{\text{initial}}$. It is assumed that the "Infusion" treatment without nitrogen (i.e. the same temperature cycle as with the nitrogen Infusion but in a vacuum), can only change the RRR value via contamination and that these same processes also take place in the presence of nitrogen in addition to the penetration of nitrogen into the surface. It should be possible to make statements about the pure nitrogen process by comparing these two RRR changes. In Fig. 48 the change in ΔRRR before and after the treatment without nitrogen compared to the samples treated with nitrogen is shown.
The highest measured value in ΔRRR is at an infusion temperature of 260°C, for the sample with nitrogen introduced. Up to a temperature of 260°C, a greater change in the RRR value can be seen for the samples infused with nitrogen compared to the samples treated without nitrogen. At 160°C and 120°C, no significant changes are observed. This is to be expected because the lower the temperature at which nitrogen is let in, the less nitrogen or other gases if present can diffuse into the material.

As already explained in section 1.6, the residual resistance can be represented according to eq. 6 from sec. 1.6 as the sum of the contamination resistances depending on the respective concentration C. This results in the following equation for the RRR

$$\text{RRR} \approx \frac{\rho_{ph}(295\text{K})}{\rho_{res}} = \frac{1.45 \cdot 10^{-7}\ \Omega\text{m}}{\sum_i \frac{\Delta\rho_i}{\Delta C_i} C_i}.$$

Assuming that the material has an initial contamination, $\Delta\rho_{init}$

$$\text{RRR}_{init} = \frac{1.45 \cdot 10^{-7}\ \Omega\text{m}}{\frac{\Delta\rho_{init}}{\Delta C_{init}} C_{init}}.$$

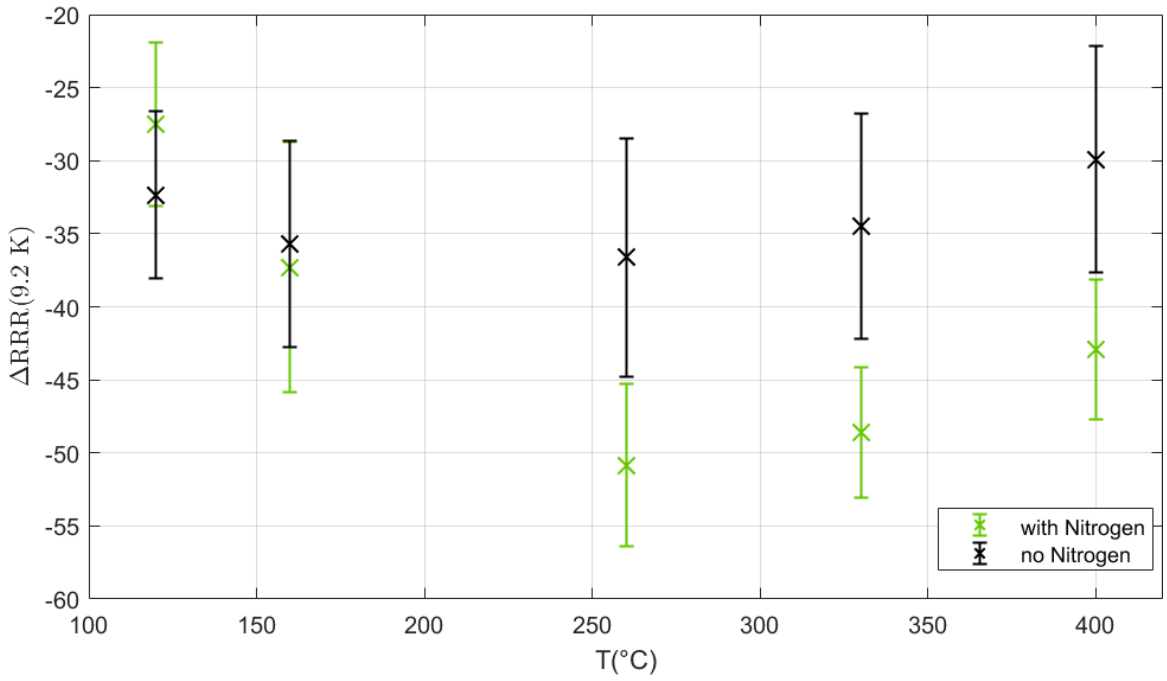

Figure 48: Difference $\Delta\mathrm{RRR}(9.2\ \mathrm{K}) = \mathrm{RRR}_{\mathrm{after}} - \mathrm{RRR}_{\mathrm{initial}}$ between before and after treatment of the samples. The treatment was done with nitrogen (green points) and under Vacuum (black points) respectively at a temperature shown on the x axis. All samples were temperature-cycled starting with 800°C for 3 hours under vacuum conditions and subsequently ramped down to the desired temperature (ranging from 120°C to 400°C) for 48h under either partial pressure of nitrogen ($3.33 \cdot 10^{-2}$ mbar) or under vacuum conditions.

After the treatment in vacuum conditions, in addition to the initial contamination, a $\Delta\rho_{new}$ is added, so that

$$\mathrm{RRR}^{noN}_{after} = 1.45 \cdot 10^{-7}\ \Omega\mathrm{m} \cdot \left(\frac{\Delta\rho^{noN}_{init}}{\Delta C^{noN}_{init}} C^{noN}_{init} + \frac{\Delta\rho_{new}}{\Delta C_{new}} C_{new} \right)^{-1}. \tag{13}$$

The $\Delta\rho_{new}$ is assumed to be composed of any "residual contamination" from the interior of the oven and any contamination still on the sample surface.
As discussed in sec. 4.4, the naturally occurring pentoxide and dioxide components start to decompose at higher temperatures. Since there is a pre-annealing step of 800°C, only a monoxide layer remains on the surface after the infusion temperature, as shown in [95]. Furthermore, it is assumed that when baking at the infusion temperature for 48 hours, the oxygen is redistributed, so that oxygen diffuses from the surface into the bulk. This process will behave differently depending on the temperature [104] [105]. For the RRR after the treatment with nitrogen is given by

$$\mathrm{RRR}^{wN}_{after} = 1.45 \cdot 10^{-7}\ \Omega\mathrm{m} \cdot \left(\frac{\Delta\rho^{wN}_{init}}{\Delta C^{wN}_{init}} C^{wN}_{init} + \frac{\Delta\rho_{new}}{\Delta C_{new}} C_{new} + \frac{\Delta\rho_{N}}{\Delta C_{N}} C_{N} \right)^{-1}.$$

This transforms to

$$C_N = \left(\frac{1.45 \cdot 10^{-7}\ \Omega\mathrm{m}}{\mathrm{RRR}^{wN}_{after}} - \frac{\Delta\rho^{wN}_{init}}{\Delta C^{wN}_{init}} C^{wN}_{init} - \frac{\Delta\rho_{new}}{\Delta C_{new}} C_{new} \right) \cdot \frac{\Delta C_N}{\Delta\rho_N}. \tag{14}$$

Transforming eq. 13 according to $\frac{\Delta\rho_{new}}{\Delta C_{new}} C_{new}$ and inserting in eq. 14 gives

$$C_N = \left(\frac{1.45 \cdot 10^{-7}\ \Omega\mathrm{m}}{\mathrm{RRR}^{wN}_{after}} - \frac{\Delta\rho^{wN}_{init}}{\Delta C^{wN}_{init}} C^{wN}_{init} - \frac{1.45 \cdot 10^{-7}\ \Omega\mathrm{m}}{\mathrm{RRR}^{noN}_{after}} + \frac{\Delta\rho^{noN}_{init}}{\Delta C^{noN}_{init}} C^{noN}_{init} \right) \cdot \frac{\Delta C_N}{\Delta\rho_N}.$$

With the $\mathrm{RRR}^{noN}_{init} = 1.45 \cdot 10^{-7}\ \Omega\mathrm{m} \cdot \left(\frac{\Delta\rho^{noN}_{init}}{\Delta C^{noN}_{init}} C^{noN}_{init} \right)^{-1}$ for the sample in which no nitrogen was introduced and $\mathrm{RRR}^{wN}_{init} = 1.45 \cdot 10^{-7}\ \Omega\mathrm{m} \cdot \left(\frac{\Delta\rho^{wN}_{init}}{\Delta C^{wN}_{init}} C^{wN}_{init} \right)^{-1}$ for the sample in which nitrogen was introduced during the treatment, the concentration of nitrogen can be deduced from

$$C_N = \frac{1.45 \cdot 10^{-7}\ \Omega\mathrm{m}}{\frac{\Delta\rho_N}{\Delta C_N}} \cdot \left(\frac{1}{\mathrm{RRR}^{wN}_{after}} - \frac{1}{\mathrm{RRR}^{wN}_{init}} - \frac{1}{\mathrm{RRR}^{noN}_{after}} + \frac{1}{\mathrm{RRR}^{noN}_{init}} \right), \tag{15}$$

where $\frac{\Delta\rho_N}{\Delta C_N} = 3.49 \cdot 10^{-11} \frac{\Omega\mathrm{m}}{wt.ppm}$ is taken from table 1 in sec. 1.6.
The RRR values from table 6 with eq. 15 give nitrogen concentrations for the respective infusion temperature shown in table 7. The negative value for the 120°C infusion is un-

Inf T	C_N(wt.ppm)
400°C	0.9 ± 0.5
330°C	0.8 ± 0.6
260°C	1.0 ± 0.6
160°C	0.04 ± 0.6
120°C	-0.5 ± 0.5

Table 7: Nitrogen concentration in wt.ppm calculated from RRR values in table 6 by eq. 15.

physical but is compatible with zero. In order to determine how much the surface had an influence on the change in the RRR value, a further short BCP of 2 minutes was done on four samples and the RRR value measured again. The results are shown in the table 8. The samples that were treated with and without nitrogen at an infusion temperature of 400°C and 260°C were selected. It would be expected that the higher the temperature, the more the surface should be affected by the nitrogen treatment. After 2 minutes of BCP, it can be assumed that roughly 2 μm has been removed from the surface. Since the RRR values did not change within the accuracy of the measurement, it can be assumed that the interstitials have penetrated much deeper than 2 microns into the sample.

Sample No.	Inf T	RRR (before)	RRR (after)	2 min BCP
3	400°C w N	295 ± 4	252 ± 4	256 ± 6
8	400°C no N	304 ± 6	274 ± 5	275 ± 6
5	260°C w N	289 ± 5	238.6 ± 2.9	238 ± 5
10	260°C no N	293 ± 7	256 ± 5	252 ± 5

Table 8: RRR(at 9.2 K) values from fine-grain samples measured by the 4-pt method. Additional BCP for 2 minutes was applied on four samples. Errors are 68% confidence level.

5.4 Discussion

The aim of the present research was to examine correlations between the nitrogen infusion temperature and the RRR value. Two different measurement methods have been used for this. One method was the alternating-field method, in which changes in the induced magnetic field are measured. Measurements were done on a cavity and on samples. Although it was found that the sensors have to be re-calibrated a useful statement can be made about relative changes before and after a treatment. The other method used on samples was the 4-pt method, which is known to be more precise than the alternating-field method but inevitable degrades the surface being measured.

The change in RRR before and after an infusion treatment with nitrogen at 120°C was measured via the eddy-current method on a single cell cavity whose performance is shown in Fig. 38 to be $\Delta\mathrm{RRR}_{\mathrm{1DE10}} = -34 \pm 12$ (see sec. 5.2.1).
This is the same order of magnitude as the 4-pt measurement on samples as discussed in 5.3 and shown in table 6. For the samples, a change in RRR value of $\Delta\mathrm{RRR}_{120°\mathrm{C,Inf}} = -28 \pm 6$ for the nitrogen infusion at 120°C and a $\Delta\mathrm{RRR}_{160°\mathrm{C,Inf}} = -37 \pm 9$ for the nitrogen infusion at 160°C was measured, which is compatible with the value for the cavity.
The 4-pt method was therefore the chosen method to investigate the parameter range as a function of temperature between 120°C and 400°C for nitrogen infusion. The change in the RRR after baking in a vacuum at 800°C for 3 hours was measured on two samples. The results are in table 5 and show no significant change. For our study, an initial temperature of 120°C was first chosen, which comes from the original recipe from Fermilab, next 160°C, which was successful at Jlab. However, for 160°C a doped behaviour of the cavities was mostly observed [82] [83]. Finally, 260°C, 330°C and 400°C were chosen empirically in order to find a maximum infusion temperature at which, if possible, no nitrides crystallize on the surface. The results are in table 6. A deterioration in RRR was found irrespective of whether nitrogen was used or not. The changes in ΔRRR due to the infusion treatments are shown in Fig. 48. For infusion with nitrogen, the change in RRR is compatible with zero for temperatures below and including 160°C. Assuming ideal vacuum conditions and a pure nitrogen atmosphere, it would be expected that the change in the ΔRRR between treatment with nitrogen and treatment without nitrogen would reduce as the infusion temperature decreases, as less and less nitrogen would diffuse into the sample. However, ΔRRR does not increase with higher infusion temperatures beyond 260°C. This suggests that other processes take place in addition to nitrogen infusion.[1] Differences between ΔRRR depending on whether or not nitrogen is injected can be seen from 260°C. The introduction of

[1] In fact, some studies have already been carried out on baking at 120°C for 48 hours and low-temperature baking in general (100°C-140°C). It was found that a low-temperature baking of cavities was beneficial in reducing the Q-drop as discussed in sec. 1.5.4. In [104], a model was introduced to explain why the Q-drop is removed by the 120°C baking. The model suggests that the baking increases interstitial oxygen near the surface, thus reducing the surface lower critical field H_{c1}. In [106], measurements were carried out on cavities that were low-T baked in a temperature range of 50°C-180°C. In contrast to the measurement shown here, the 800°C step was omitted. The surface RRR value of the cavities was also determined before and after the treatments and showed that the RRR value decreased with increasing temperature. The idea behind this was that an oxygen redistribution took place, so that oxygen diffused from the natural surface oxide layer into the bulk material. This could also explain the deterioration in RRR when treating without nitrogen in the results presented here.

nitrogen causes RRR to decrease, as manifested in the increase of ΔRRR as shown in Fig. 48, as expected since the nitrogen diffuses into the material. Although there is a tendency for ΔRRR to decrease with temperature after 260°C, the data are insufficiently precise to establish this. Finally, based on the measurement shown here, it can be concluded that the bulk RRR value of samples is reduced after an infusion with nitrogen compared to without nitrogen at the same temperature.
Unlike the low-temperature bake at 120°C which is known to improve the HFQS (see sec. 1.5.4) [48], in these experiments the temperature was initially held at 800°C. Better information about actual changes in the surface could be obtained if the contacts were closer together so that the field lines as shown in Fig. 44 stay closer to the surface. A alternative method could be to use thinner samples and thus change the volume to surface ratio enough to have the RRR changes more influenced by surface processes. Furthermore, it would be interesting to repeat the measurement and remove layer by layer with chemical etching to reveal how the RRR changes with depth. To use large-grain material for this investigation would help to establish whether grain boundaries have an important role in this process.

6 Surface composition for nitrogen infusion at 400°C

6.1 Introduction

To detect a nitrogen signal with secondary ion mass spectrometry (SIMS) in niobium samples after a nitrogen infusion could help to understand to what extent the nitrogen content plays a role in the performance enhancement by this treatment. Measurements were done with a time-of-flight SIMS (ToF-SIMS) at Fraunhofer IFAM in Bremen, Germany. The ToF-SIMS approach is based on mass analysis of secondary ions in a time-of-flight mass spectrometer. ToF-SIMS is a surface-sensitive method that utilizes a pulsed ion beam to remove molecules (secondary ions) from atomic monolayers on the surface of the sample. The mass of the particles is determined by measuring the time it takes for them to reach the detector. The method's excellent detection sensitivity allows the detection of trace elements with concentrations as low as ppm. The intensities of secondary ion signals do not allow any clear conclusions regarding the quantitative composition of the individual components due to the significant reliance of secondary ion emission on the surroundings of the emission point (matrix effect). In the static operating mode, less than 10% of the atoms of the top monolayer are removed during a measurement. In this mode, the information depth comprises the top one to three monolayers. In all experiments to date, no nitrogen could be found in the SIMS measurements for all samples which were infused together with cavities at DESY for infusion temperatures of 120°C and 160°C. However, the incorporation of nitrogen into Nb following exposure to $3.3{\cdot}10^{-2}$ mbar nitrogen at 120°C has been reported [5] [82].

Before the 800°C nitrogen doping, attempts to develop the nitride phase for surface passivization in SRF cavities failed to achieve the Q-rise phenomenon. As described in [48], it was assumed that by reducing the amount of impurities and defects within the penetration depth of the RF field from the Nb surface the performance would be improved, both in terms of quality factor and maximum accelerating gradient. It has long been known that baking at 800°C for several hours in UHV can reduce the density of lattice defects such as dislocations and vacancies. The amount of interstitial hydrogen should also be reduced and, as already mentioned in sec. 4, the oxide layer dissociates so that only a few monolayers of NbO remain on the surface. However, the residual gases inside the furnace would be reabsorbed by Nb after cooling and subsequent exposure to air and water, which would be an issue with this technique. It was proposed at SLAC already in 1971 [107] that a way to overcome this would be by passivating the surface. A passivated layer should act as a diffusion barrier and thus preventing hydrogen and oxygen absorption from the atmosphere. For surface passivization it was suggested to form a thin nitride layer (of about 10 nm) on the surface by thermal diffusion of nitrogen during the furnace cooldown. The nitride layer should be thin enough to not affect Nb's superconducting characteristics considerably. A calculation from [107] showed that a nitride layer about 10 nm thick on the Nb surface can be achieved by admitting a nitrogen partial pressure of about $5 \cdot 10^{-6}$ Torr (or $\sim 6.67 \cdot 10^{-6}$ mbar) at 400°C for 15 min. When a single-cell large-grain SRF cavity was heat-treated at 800°C for 3 h then cooled down to 400°C and baked in a nitrogen environment with a partial pressure of 10^{-5} mbar, an overall increase in quality factor was found [48]. However, SIMS on witness samples did not show the presence of any interstitial nitrogen or formation of a nitride layer. Thus their conclusion was that the temperature and partial pressure of nitrogen were insuf-

ficient for nitrogen to diffuse into niobium or for any nitride phase to form. The detection of nitrogen with the help of SIMS is difficult, as mentioned above. Even after treatment at only 120°C, as is usual with nitrogen infusion, nitrogen could be detected, as noted in other publications. This shows that previous research is still controversial, especially with regard to SIMS measurements on nitrogen-treated niobium.
In this chapter the results of infusion in the sample oven are presented - the aim is to use SIMS to detect a nitrogen signal and to find possible differences between fine-grain (FG) and large-grain (LG) samples. Since previous measurements with SIMS did not show any signal in the temperature range from 120°C to 160°C, a temperature of 400°C, close to the temperature beyond which no nitrides are formed, was selected, as discussed in sec. 5.3. The partial pressure of nitrogen with $3.3 \cdot 10^{-2}$ mbar was kept the same as for the standard nitrogen infusion treatment from [5] as well as the temperature-holding times (3 h at 800°C and 48 h at 400°C). The results in [48] on nitrogen treatment at 400°C did not show any nitrogen incorporation. However, the nitrogen pressure was $\sim 6.67 \cdot 10^{-6}$ mbar compared to $3.3 \cdot 10^{-2}$ mbar and the holding time when nitrogen was introduced was 15 min compared to 48 h in the current work, the amount of nitrogen was several orders of magnitude lower. [2]

6.2 Results

The infusion steps for this process were to ramp to 800°C in vacuum conditions, hold for 3 hours, cooldown to the desired infusion temperature, introduce nitrogen at $3.3 \cdot 10^{-2}$ mbar and hold for 48 hours. In a first attempt, nitrogen was infused on a conical FG sample from the manufacturer Ningxia (see sec. 3 Fig. 15 (a) for sample shape) in the sample oven at 180°C. No caps or other cover against line-of-sight particles were used. The sample received EP for 4 hours as a pre-treatment. No measurable nitrogen signal was found via SIMS as shown in Fig. 53 (a). The surface was inspected via SEM and showed no precipitates on the surface as shown in Fig. 49. During the next treatments, the samples were placed in a small niobium box (see sec. 7.2.4 Fig. 73) which serves as a line-of-sight protection (LOS) and which was previously annealed at 1000°C in a vacuum. For the next attempt, two conical samples, one cut from LG and one from FG material, were infused at 400°C. The LG sample was cut from a single grain of material from the manufacturer Heraeus. The FG sample is from Plansee. The LG sample received a BCP before the infusion. The FG sample received a cavity like pre-treatment consisting of EP for 4 h, 800°C annealing in vacuum conditions for 3 h, a second EP for 1 h and 120°C annealing in vacuum conditions for 48 h. Some areas of the niobium sheet used have turned blue after the treatment in the furnace, as can be seen in Fig. 50. This suggests that the niobium surface is heavily oxidized, caused by residual oxygen or a leak in the nitrogen line. The niobium box used as LOS and the sample that was in it did not turn blue.

[2] The measurement parameters with the SIMS used were: excitation with a 25 keV bi-liquid metal-ion source; bunched mode; analysis area 100 x 100 μm^2; charge compensation with a pulsed electron source. The Sputter parameters were: 3 keV argon ions; area: 300 x 300 μm^2; partial pressure in the Ar source was $3 \cdot 10^{-5}$ mbar.

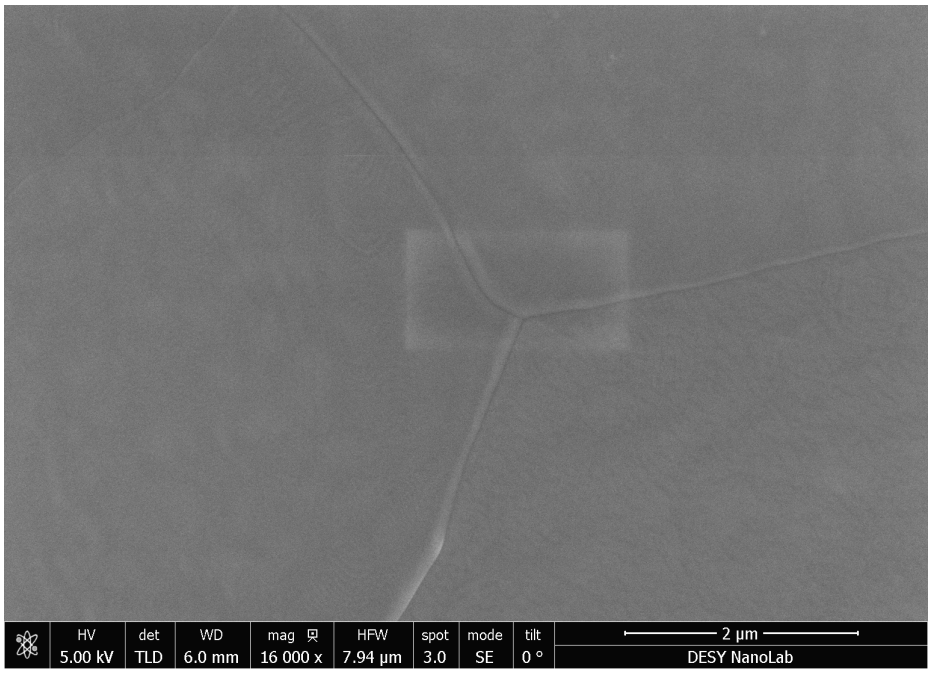

Figure 49: SEM image of EP'ed fine grain sample surface after 180°C nitrogen infusion. The grain boundaries are clearly visible while the surface has a clean smooth appearance. The rectangle comes by the charging effect from the scanning electron microscopy which is known to cause change in image contrasts [108].

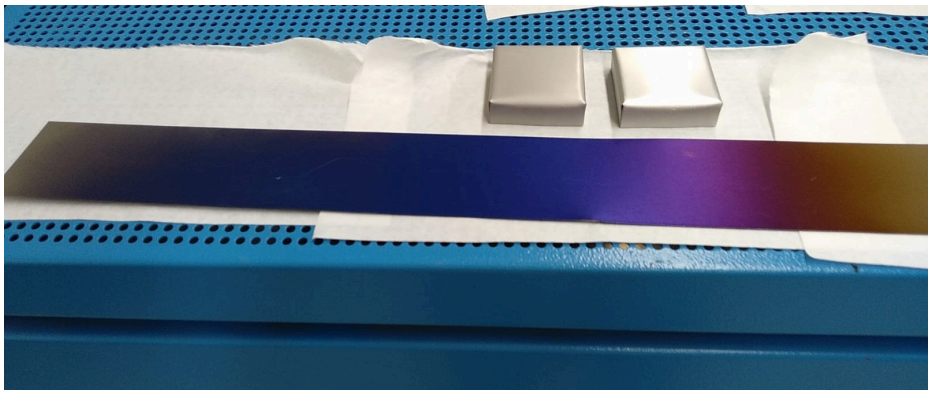

Figure 50: A niobium sheet used inside the sample furnace that went blue due to oxidation during a nitrogen infusion treatment at 400°C. Residual oxygen in the nitrogen line is suspected as a cause.

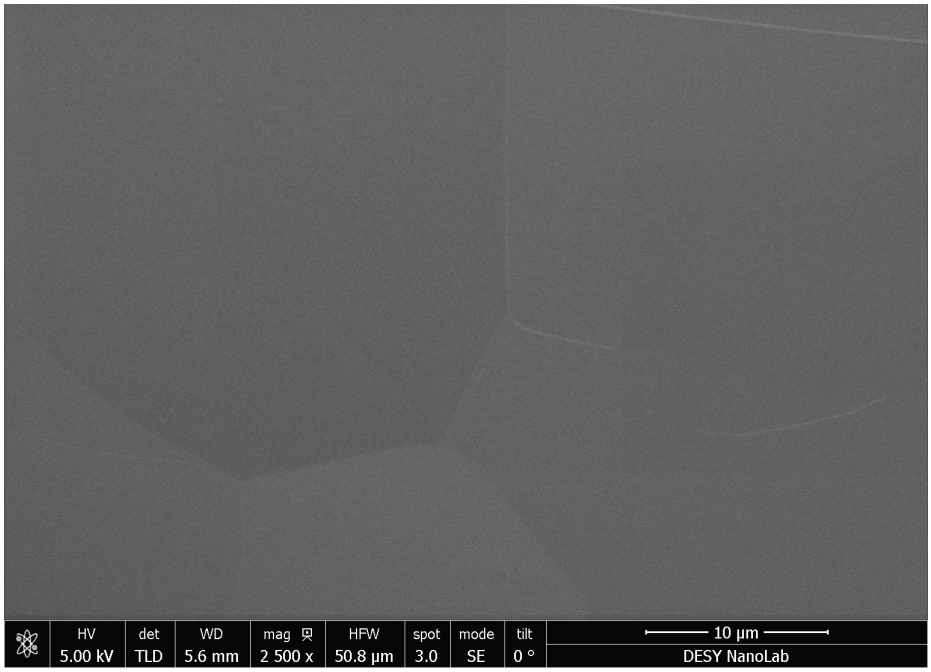

Figure 51: SEM image of EP'ed fine-grain-sample surface after 400°C nitrogen infusion.

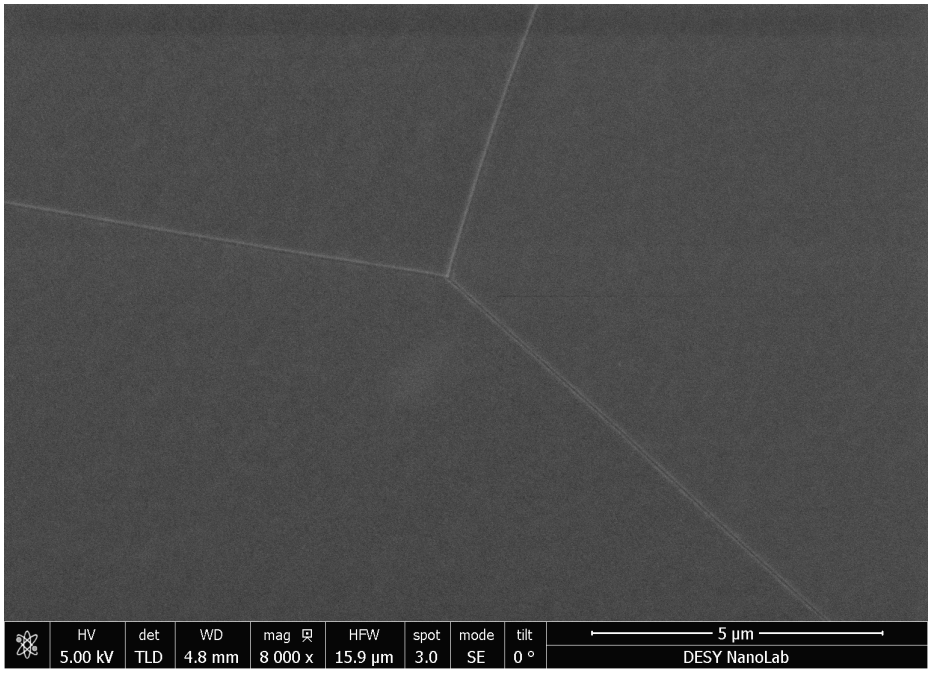

Figure 52: SEM image of EP'ed fine-grain-sample surface after 2nd 400°C nitrogen infusion.

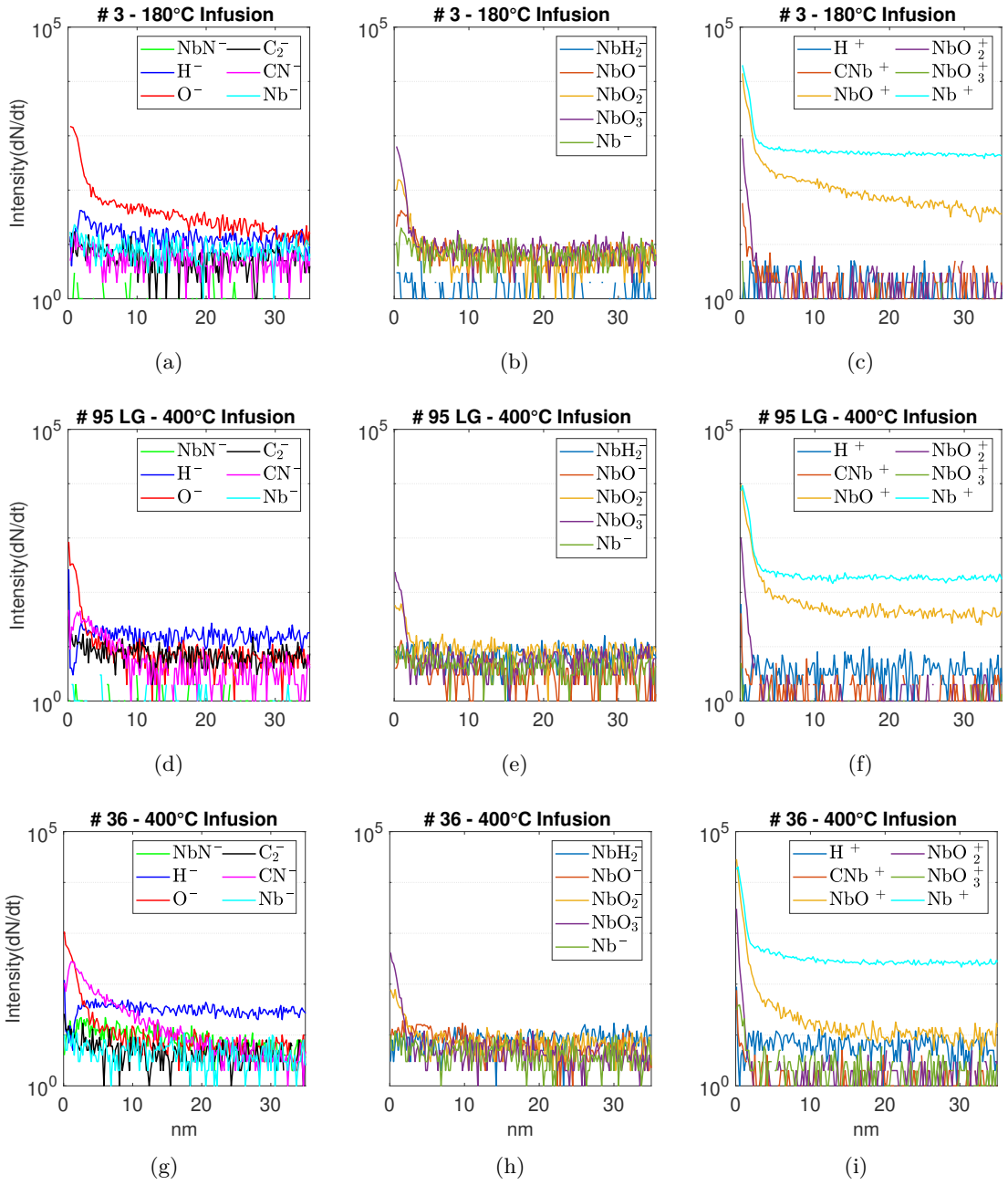

Figure 53: SIMS data of niobium samples that have been nitrogen infused in the sample furnace mentioned in sec. 3.2. The negative ions are split into two figures to aid visibility. Sample 3 is a fine-grain infused at 180°C. Sample 95 is a large-grain infused at 400°C. Sample 36 is a fine-grain infused at 400°C.

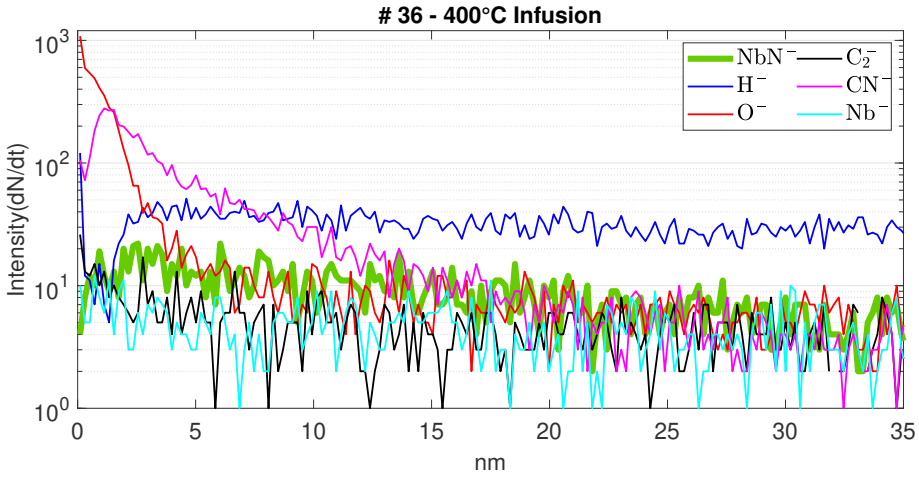

Figure 54: SIMS data of niobium sample that have been nitrogen infused in the sample furnace mentioned in sec. 3.2.

The SIMS measurement shows a high oxygen content in the LG sample, as can be seen in Fig. 53 (f) for the positive ions. This confirms the assumption that there was residual oxygen or a leak during the treatment. No significant nitrogen signal was measured. The FG sample was inspected via SEM and showed no precipitates, as can be seen in Fig. 51. No SIMS data exist from this FG sample. Therefore, another 400°C infusion took place. One conical FG sample from Plansee was placed inside the oven with LOS protection during this run. The sample also received a full cavity-like pre-treatment. Again, the SEM revealed no precipitates after the infusion treatment, as shown in Fig. 52. A NbN signal was detected as shown in Fig. 53 (g). In addition, a CN signal was measured. Besides NbN, CN is the only other nitrogen-containing fragment that can be measured. The presence of both signals together indicates that nitrogen was present in the sample. It is shown again enlarged in Fig. 54. For the first time, an NbN signal from the treated conical Nb samples presented in this work was detected with this measuring device. Since for the LG sample no nitrogen has been detected while a weak signal has been present for the FG sample, there is evidence that grain boundaries are necessary to absorb a detectable amount of nitrogen at the Infusion temperatures. The oxygen content is comparatively very low. The fact that no significant amount of C_2^- was detected confirms that the samples were carbon free. In addition to the conical FG sample, another fine grain sample was treated for the RRR measurement presented in sec. 5.3. As discussed there, the RRR value changed by $\Delta\mathrm{RRR} = -43 \pm 5$.

6.3 Conclusion

When considering the depth profiles, it must be taken into account that the niobium signal is only detected in a significant intensity in the positive secondary-ion polarity. The niobium-oxide signals were found in both positive and negative polarity. The nitrogen-containing fragments, on the other hand, were only detected in the negative polarity. SIMS measurements showed an NbN signal on a fine-grain sample that had been nitrogen infused at 400°C. No such signal was observed on a large-grain sample. However, oxygen contamination was present for the run with the large-grain sample. Another fine-grain sample that was nitrogen infused at 180°C showed no NbN signal either but high oxygen signal for negative and positive polarity. There are two likely causes why no nitrogen was measured for sample 95: That the oxygen residues passivated the surface for the infusion process; diffusion in niobium is dominated by diffusion along grain boundaries. Sample 95 is a large-grain sample which had no grain boundary over the whole sample. Sample 36 is a fine-grain sample, providing a better diffusion potential for nitrogen.
In [95], XRR measurements were done on nitrogen-infused samples. The concentrations observed in [5] [82] must have been detected by XRR measurements. However, this was not confirmed in the publications. It was suspected that the absence of grain-boundaries in the single-crystalline sample that was used could be the reason why nitrogen wasn't detected. The existence of grain-boundaries may operate as both a nucleation and diffusion location for foreign phases and interstitial species.
Since the samples showed no precipitates in the SEM, there was no evidence for carbide formation, as confirmed by the low carbon signals in the SIMS measurements. Furthermore, the fact that no precipitates were found in the SEM implies that no nitrides were formed either. This indicates that our observed NbN signal in Fig. 53 (g) and 54 could actually be interstitial nitrogen that has accumulated in the first few atomic layers. It would therefore be interesting in future to carry out X-ray photoelectron spectroscopy (XPS) measurements on 400°C-infused samples. Another test with a large-grain sample in a clean oven without an oxygen leak could give information on the role of the grain-boundaries. This would be very interesting for a future research program.

7 Niobium-Carbide formation due to heat treatment and the usage of "line-of-sight" protection

7.1 Introduction

In this chapter, first results of attempting nitrogen infusion on cavities and samples are presented. Fig. 55 (a) shows data [109] in which several cavities were baked at 800°C without post-chemical treatment and tested. Since the cavities were severely degraded, niobium caps at the flanges were used as an protection against particle contamination from the oven surface in the line of sight (LOS) of the cavity inner surface. Using the caps prevented performance degradation as shown in Fig. 55 (b). It was concluded that the furnace was

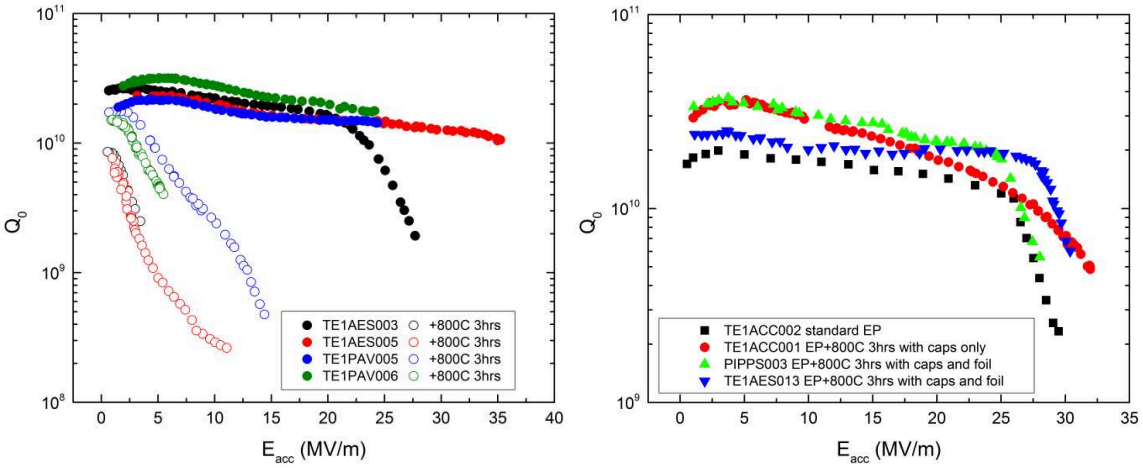

(a) Performance degraded in fine-grain cavities after baking at 800°C for 3 h under vacuum conditions without post-chemical surface-material removal. Solid points are before the bake and open ones of the same color are after the bake for the same cavity.

(b) No performance degredation after 800°C baking with the caps solution.

Figure 55: All curves shown are taken at 2 K. Graphs taken from [109].

contaminated either with carbon or titanium from the cavity Nb-Ti flanges. The usage of niobium protection caps was therefore maintained for the nitrogen-infusion experiments. It has been shown in [110] that subsequent etching removes the performance enhancement from the nitrogen-infusion treatment. The avoidance of subsequent chemical treatment is a crucial factor in the success of nitrogen infusion of a cavity. Cavity performance[3] before and after the first testing of heat treatments at DESY, i.e heating at 800°C for 3 h under vacuum conditions followed by a cooling down to 120°C and hold for 48 h, and without subsequent chemical surface removal led to the results shown in Fig. 56. Except for 1DE18, no nitrogen was used deliberately to test the furnace vacuum environment for high-temperature treatment and whether Q_0 degradation happens after high-temperature treatment without post-chemical surface removal. Cavity 1DE18, received a 120°C nitrogen infusion. However, the nitrogen pressure was one to three orders of magnitude lower than the Fermilab's

[3]Cavities are numbered by 1DE"XX" with "XX" the respective number.

formula suggested due to issues with the nitrogen regulation. Although the Q_0 dependence of the cavity 1DE16 did not degrade after the first attempt, the achievable gradient was reduced. It was then heated once more without any chemical treatment and degraded after the 2nd treatment. 1DE18 and 1DE17 degraded after their first heat treatment. Although

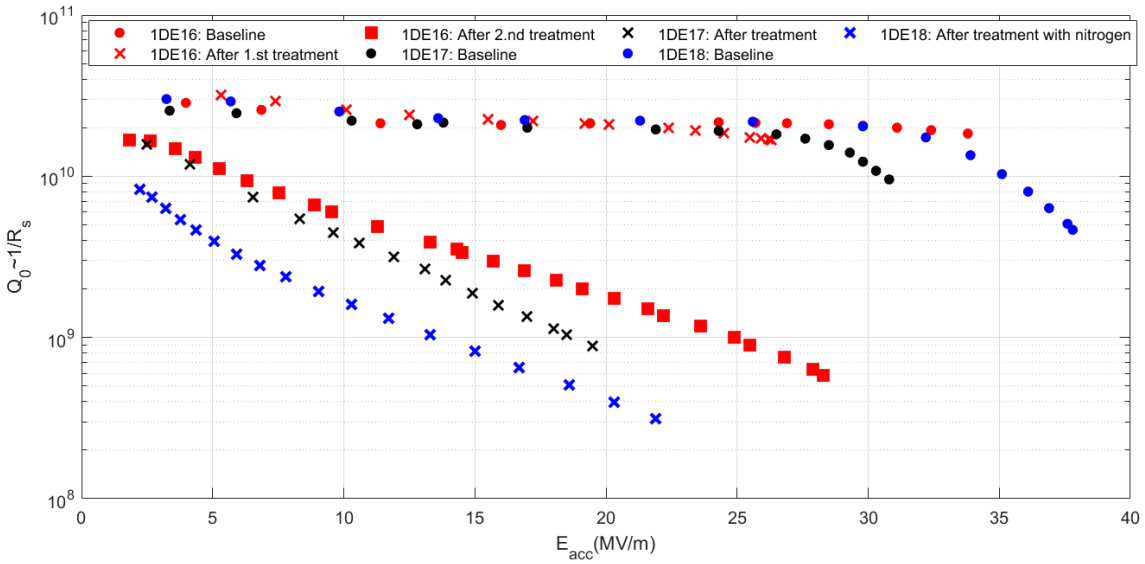

Figure 56: Cavity performance after the first attempts of heat treatment without subsequent chemical surface removal on three single-cell cavities 1DE16, 1DE17 and 1DE18 at DESY. Performance before the treatment is shown in the baseline curve for each cavity. All curves shown are taken at 2 K.

niobium foils were used as a LOS protection during the heat-treatment runs of the cavities labelled as 1DE16, 1DE17 and 1DE18, the cavity performance degraded as shown in Fig. 56 in a similar way to that observed in [109] when no LOS protection was used, as shown in Fig. 55 (a). Investigations on witness samples during our cavity heat treatments are presented in the next section.

7.2 Investigations on niobium witness samples

7.2.1 Usage of HOM coupler as LOS

During the annealing runs shown in Fig. 56, samples were placed under a bcp'ed RRR $\sim$ 300 niobium HOM-coupler housing as shown in Fig. 57 as a protection against particle contamination from the oven surface that is in line of sight (LOS) to the sample surface, similar to the caps that protect the cavity inner surface. Samples of all of these runs showed precipi-

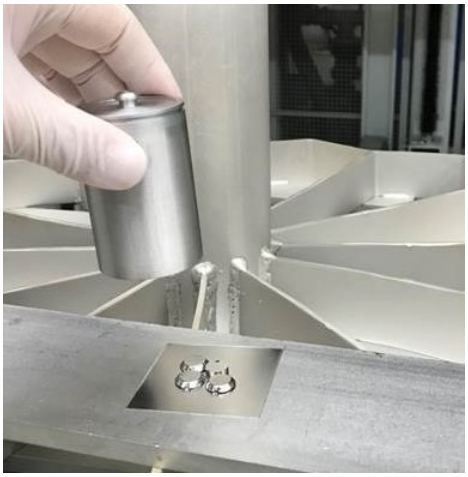

Figure 57: Coverage of cavity witness samples beneath a HOM-coupler housing as an protection against particle contamination from the oven surface in the line of sight (LOS) to the sample surface. In total, four samples are placed on a thin niobium sheet and the HOM coupler placed over them.

tates on the surface as shown for one sample in the SEM image in Fig. 58. Analysis with Energy Dispersive X-Ray Spectroscopy (EDX) on the precipitates shown in Fig. 58 in a transmission electron microscope (TEM) proved those to be carbides as shown in Fig. 60. For TEM, very thin rectangular cross-sectional samples, so-called "lamellas", were cut from the niobium sample surface via a focused ion beam. For the TEM measurement, the FEI Helios NanoLab G3 (DualBeam) instrument at Technical University of Hamburg Harburg, which includes a focused ion beam, was used. The top of the lamella was covered by a protective layer of platinum as shown in Fig. 59 (a). This helps to protect the native niobium surface from Ga ions coming from the Focused Ion Beam (FIB) during the material removal (milling). The material is removed around this area to cut a piece out of the sample. In Fig. 59 (b), a SEM image of the niobium sample surface after the material removal around the platinum layer is shown. With the FIB lift-out technique, the lamella was mounted onto a standard copper TEM half-grid using an Omniprobe micromanipulator as shown in Fig. 59 (c). Care was taken to ensure that the star-shaped precipitates were located within the lamella. The thickness of the lamella at this point was about 120 nm and was cut even thinner to about 5 nm at the near surface for the transmission electron microscopy. A TEM image from the prepared lamella of the sample near the surface is shown in Fig. 59 (d).
The elementary composition of a cross section of the lamella was determined using EDX, as shown in Fig. 60. A clear signal for carbon enrichment of the precipitates can be seen

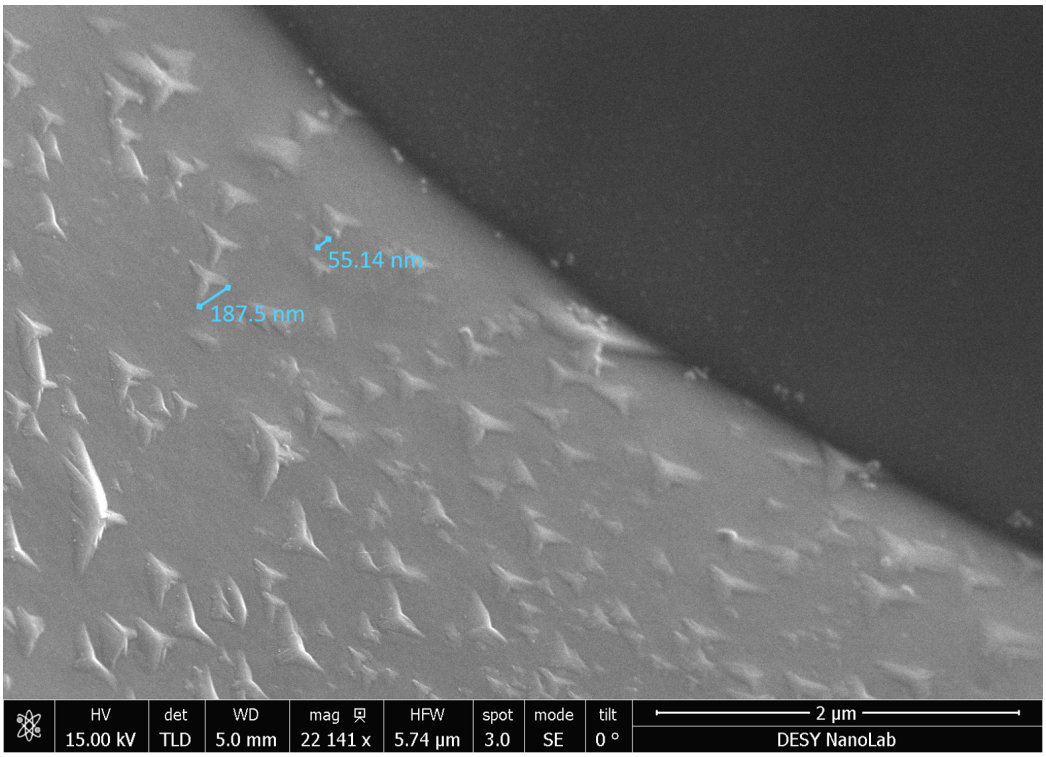

Figure 58: SEM of witness sample from heat treatment with one of the degraded cavities 1DE16 whose properties were plotted in Fig. 56. Precipitates were found on samples of each run and identified as carbides via EDX in a TEM. Two examples were measured to have sizes of 187.5 nm and 55.14 nm, as shown in blue.

in red. A possible phase for these crystalline forms of niobium-subcarbide is Nb_2C which could be detected in [111] by means of spectroscopic studies of cavity cutouts from 1DE16. A oxygen signal is detected for the whole bulk. The nitrogen signal that can be seen in green in Fig. 60 comes from the protective platinum layer that was sputtered on top of the lamella but no nitrogen signal is observed in the niobium sample.

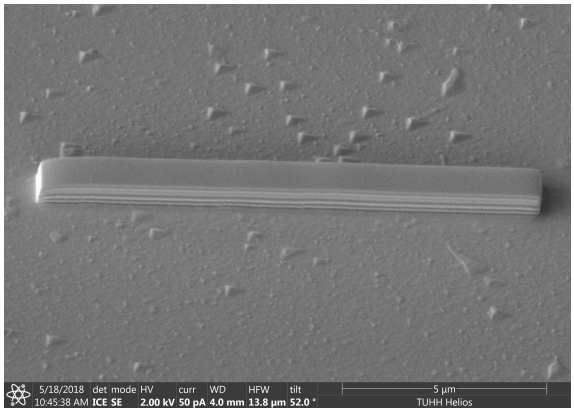

(a) SEM image of protective platinum layer deposited onto the niobium surface of the sample.

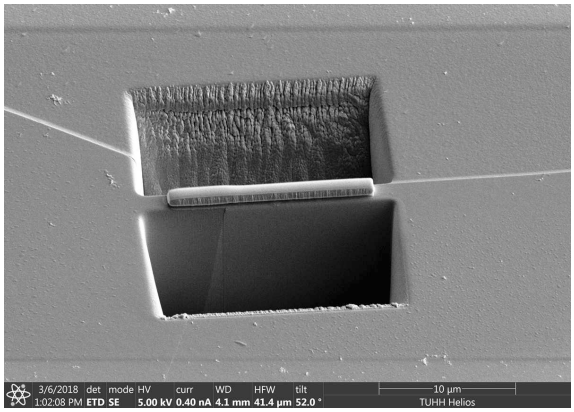

(b) SEM image of niobium sample surface after material removal (milling) around cross-sectional rectangular platinum layer. The lamella then consists of the thin layer that remains after the milling.

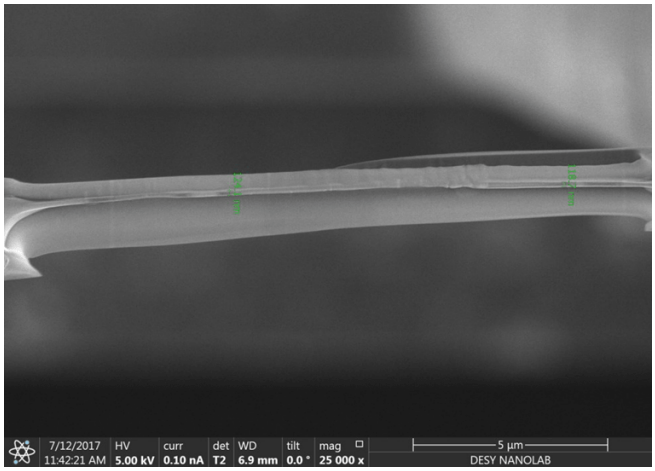

(c) SEM image with top view of the prepared lamella cut with the FIB lift-out technique from the prepared area shown in (b).

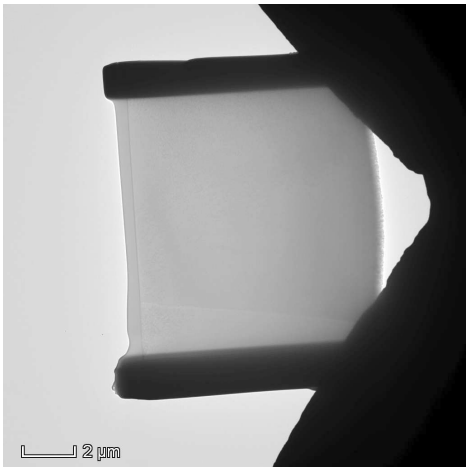

(d) TEM of the lamella.

Figure 59: Process of cross-sectional sample (lamella) preparation via Focused Ion Beam for Transmission Electron Microscopy (TEM) from a niobium sample with star-shaped precipitates on the surface done with a FEI Helios NanoLab G3 (DualBeam) instrument at the Technical University of Hamburg Harburg.

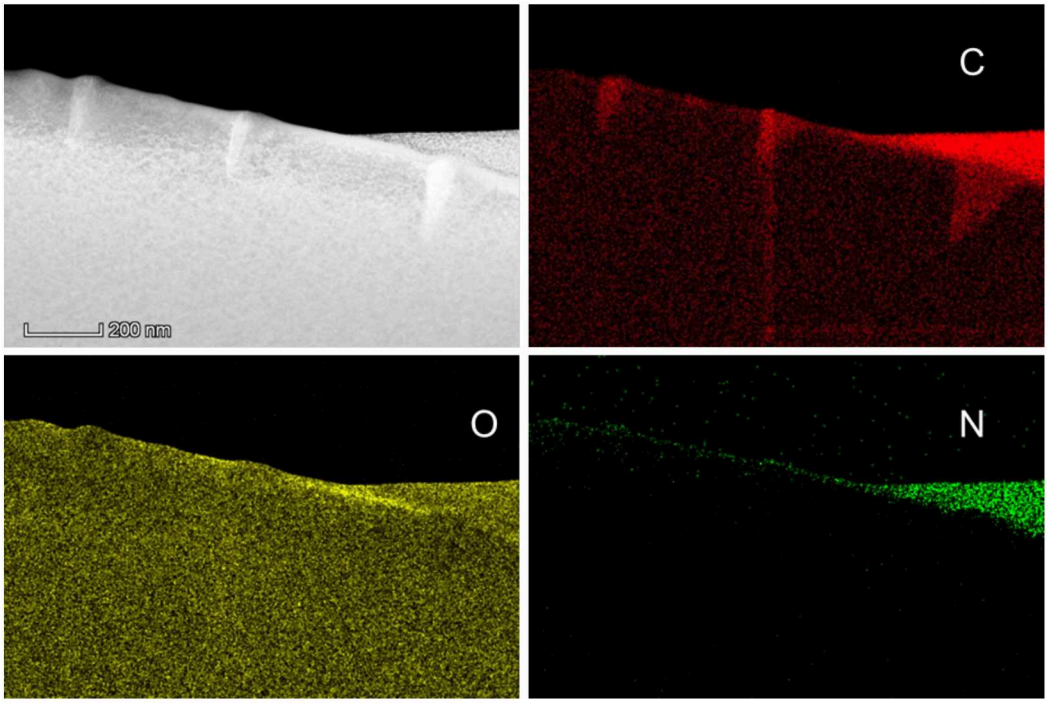

Figure 60: Energy-dispersive X-ray spectroscopy (EDX) in Transmission Electron Micrographs of a vertical cross section from niobium sample (Fig. 59) that grew precipitates during heat treatment from a cavity whose properties were shown in Fig. 56. The upper left images shows an bright-field TEM image of the cross section. The mountain-range-like structures are a profile view from the star-shaped precipitates that were observed on the sample. They intrude about 200 nm deep into the niobium bulk. The other images show elemental maps where an EDX spectrum is taken for each pixel and the intensities converted into brightness, each element being denoted by a certain color. Carbon is shown in red, oxygen in yellow and nitrogen in green.

A carbon-rich atmosphere beneath the HOM-coupler housing might have caused the precipitation of star-shaped Nb_2C during temperature annealing. In order to determine the source of the carbon-rich atmosphere, the caps used in these experiments were analyzed. A different cap cutout that had not previously been used is shown in in Fig. 61 (a). The cap had only been BCP'ed but shows particle contamination by dust when not handled in clean-room conditions, as in this case a piece of the cap was directly cut after the BCP. A SEM image of a cutout from a cap that had been used for the heat treatments of 1DE16, 1DE17 and 1DE18 is shown in Fig. 61 (b). The black spots in Fig. 61 (b) indicate carbon-rich contamination. Fig. 61 (b) shows a very rough surface as this cap had already been used several times.

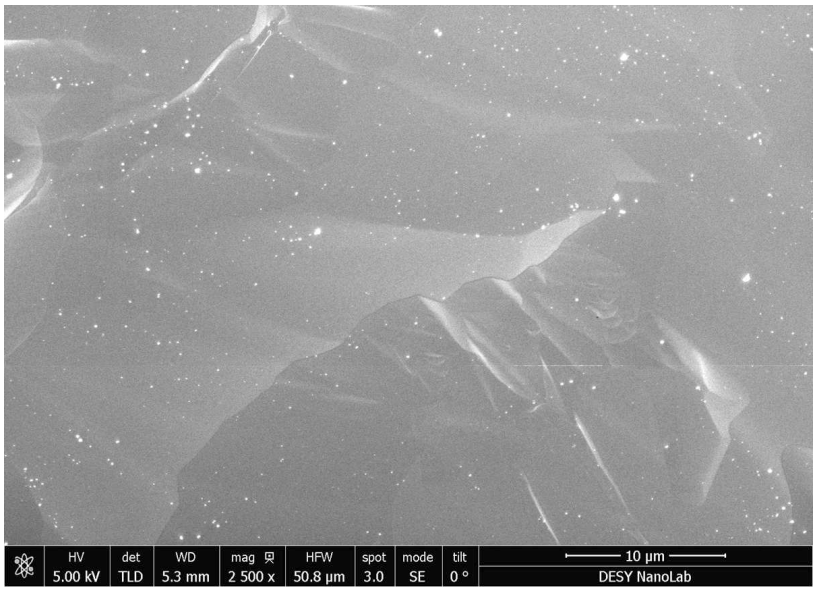

(a) SEM image of a freshly BCP'ed cap cutout.

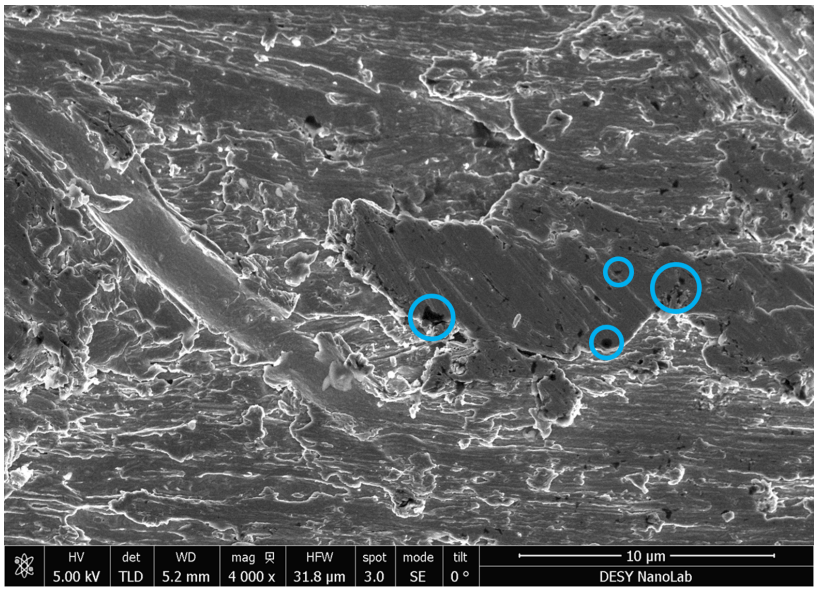

(b) SEM image of a cutout from a cap that was used for high-temperature treatments of the cavities 1DE16, 1DE17 and 1DE18.

Figure 61: Comparison of niobium cap cutouts which are intended to give line-of-sight particle protection during high-temperature treatments of cavities. Image (a) shows a cap cutout that had only been BCP'ed without subsequent cleaning in the clean room. Image (b) shows a cutout from a cap that has been used for the heat treatments of 1DE16, 1DE17 and 1DE18 as LOS protection. The cap always received a short BCP between the treatments. Dark spots (some of which are circled in blue) indicate carbon contamination.

7.2.2 Niobium box as LOS protection

For some of the next nitrogen infusion runs, a niobium box made from the same material as the caps rather than the HOM-coupler housing as shown in Fig. 62 was used as LOS protection of the samples. The niobium box underwent a BCP, ultrasonic cleaning and de-ionized-water rinsing in the clean room before each run. Figure 62 shows cavity 1DE27 with the usual niobium foils wrapped around the flanges. The cavity underwent a nitrogen infusion according to the Fermilab recipe at 120°C and a second one at 160°C without any chemical treatment in between. In those runs, a witness sample was also placed on top of the niobium box, thus directly exposed to the furnace vacuum, in addition to the sample placed inside the box. In total four samples were used together with 1DE27 (two for each infusion run). The performance test results of 1DE27 after the 120°C and 160°C treatments are shown in Fig. 63. There was almost no change after the first nitrogen infusion at 120°C, shown as the blue points. It can therefore be assumed that, although the performance was not improved, the cavity was not contaminated at this point. After the nitrogen infusion at 120°C and the performance testing of this cavity, it was cleaned by high-pressure rinsing in the clean room before it directly went for the second infusion at 160°C. The performance after the second nitrogen infusion shows a degradation in Q_0 at high fields and also a lower Q_0 for low fields but the degradation with voltage is not as strong as the cavities shown in Fig. 56. SEM images of those samples are shown in Fig. 64. In both runs, carbide

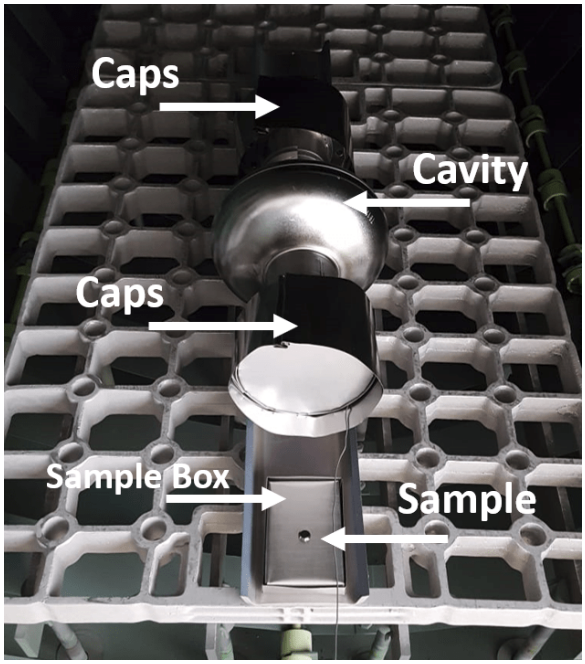

Figure 62: Picture of the interior of the vacuum furnace with the cavity 1DE27. Niobium foils are wrapped around the flanges as protection from LOS particles inside the furnace (labelled "caps"). Two witness sample were also placed inside the furnace. One is within a niobium box to mimic the caps for the samples. One sample is placed outside the box and is thus exposed to the furnace vacuum.

precipitation occurred on samples inside the box only. Samples outside the box and thus

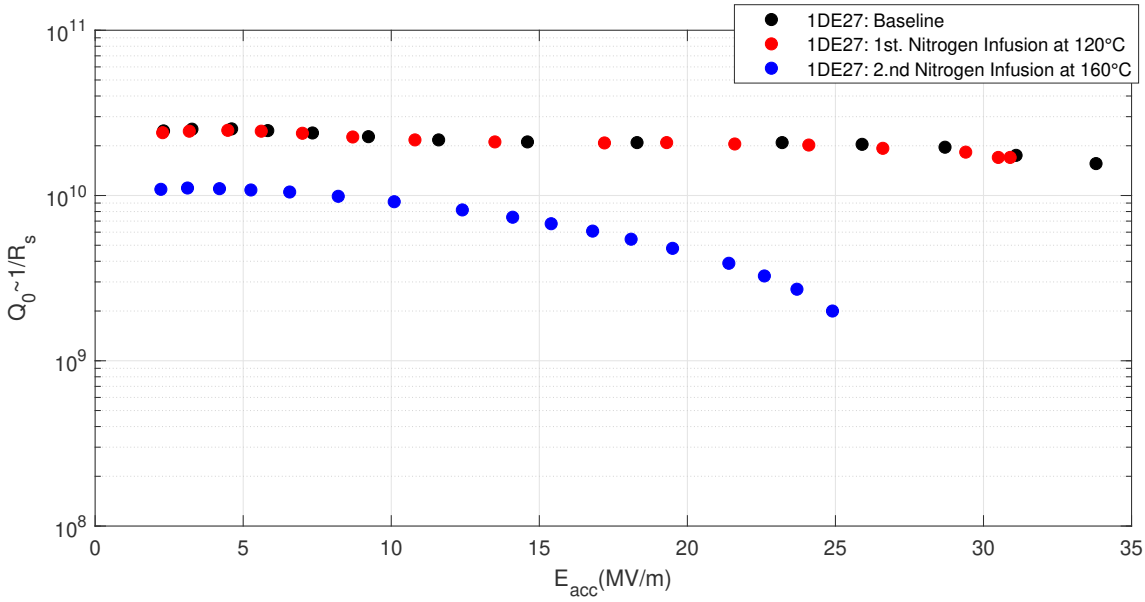

Figure 63: Cavity performance of 1DE27 after a nitrogen infusion attempt at 120°C (red) and a second one at 160°C (blue) without any chemical treatment in between. The performance before the nitrogen infusion is shown in the baseline curve (black). All curves shown were taken at 2 K.

exposed directly to the furnace vacuum during the treatment both show a very clean surface without precipitates except at grain boundaries, as can be seen in Figs. 64 (a) and (c). This indicates that the furnace was not contaminated but the caps were. Some precipitates here are darker, which can be better seen on a larger-scale image in Fig. 65. Increasing the magnification in a region with dark precipitates as for example shown in Fig. 66 causes a small, lighter, box to appear, which is visible in Fig. 64 (b). This could be a charging effect from the SEM. It is well known that if carbon is present in SEM it can cause imaging artefacts [112]. As well as the typical star-shaped phases as in Fig. 58, other forms of precipitation particularly at grain boundaries can be observed.
Samples outside the niobium box showed no carbide precipitation. SIMS data of the samples from the 120°C infusion run are shown in Fig. 67 (a), (b) and (c) and from the 160°C infusion run in Fig. 67 (d), (e) and (f). Although, there is no carbides for samples outside the box, the SIMS data show signals for unattached carbon everywhere. The carbon signal is higher for the sample inside the niobium box compared to the sample outside the box in both cases. The sample outside the box from the 160°C infusion run shows a slightly higher oxygen level then the sample inside the box. The relative difference in the carbon signal between the two samples here is less pronounced compared to the first infusion run. Furthermore, the amount of oxygen is lower for the sample inside the niobium box compared to the sample outside. The other elements show no significant difference between solid line and dashed line. No significant nitrogen signal is observed.
Additionally X-ray photoelectron spectroscopy (XPS) measurements were done from the

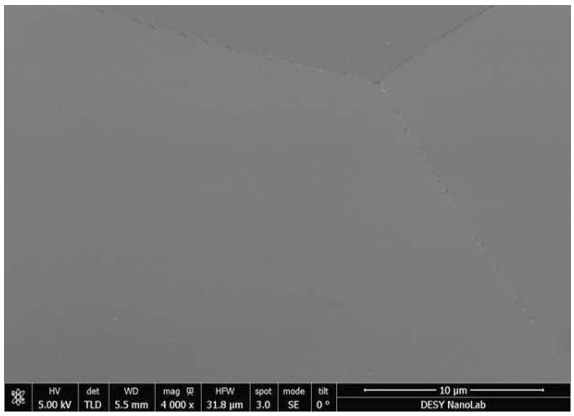

(a) Witness sample from first nitrogen infusion at 120°C outside the niobium box.

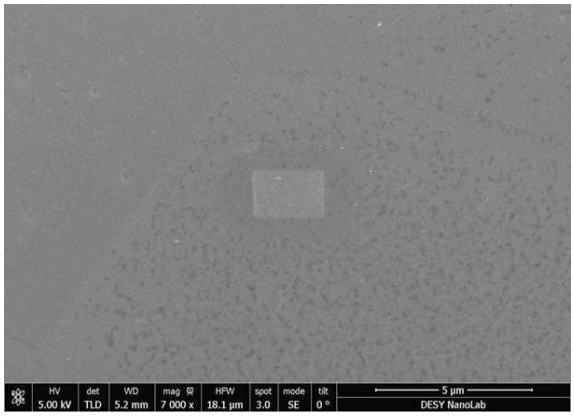

(b) Witness sample from first nitrogen infusion at 120°C inside the niobium box.

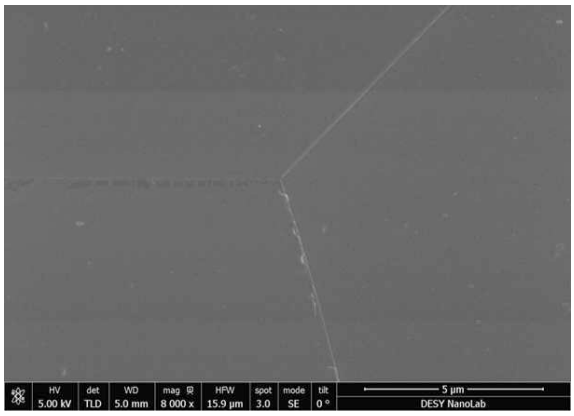

(c) Witness sample from second nitrogen infusion at 160°C outside the niobium box.

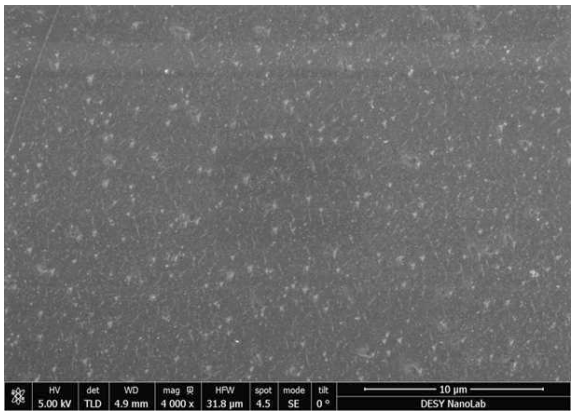

(d) Witness sample from second nitrogen infusion at 160°C inside the niobium box.

Figure 64: SEM images of samples inside and outside a niobium box during the nitrogen infusion treatments of 1DE27. In both cases, no precipitation occurred on grain surfaces on samples outside the box and only on the samples inside the box. However, samples outside the box do show some precipitation at grain boundaries in (c) which is also faintly visible in (a).

samples of both infusion runs that were inside the box. The data is shown in Fig. 68. It shows a higher amount of oxygen and carbon for the sample from the 160°C infusion compared to the 120°C infusion. Another 160°C nitrogen infusion was done with cavity 1DE7. The cavity performance before and after each treatment is shown in Fig. 69. It is similar to the curve of 1DE27 after the second infusion at 160°C. In this run, another cavity instead of a niobium box was used as a LOS protection for the witness samples. The cavity and sample installation inside the furnace is illustrated in Fig. 70. SEM images of the witness samples are summarized in Fig. 71. Precipitation occurred on samples both inside and outside the screening cavity. In this run, two cavities, 1DE7 and the cavity used to screen the samples were treated together, which means more component material and more possible degassing could be present. This could explain the source of the carbon contamination.

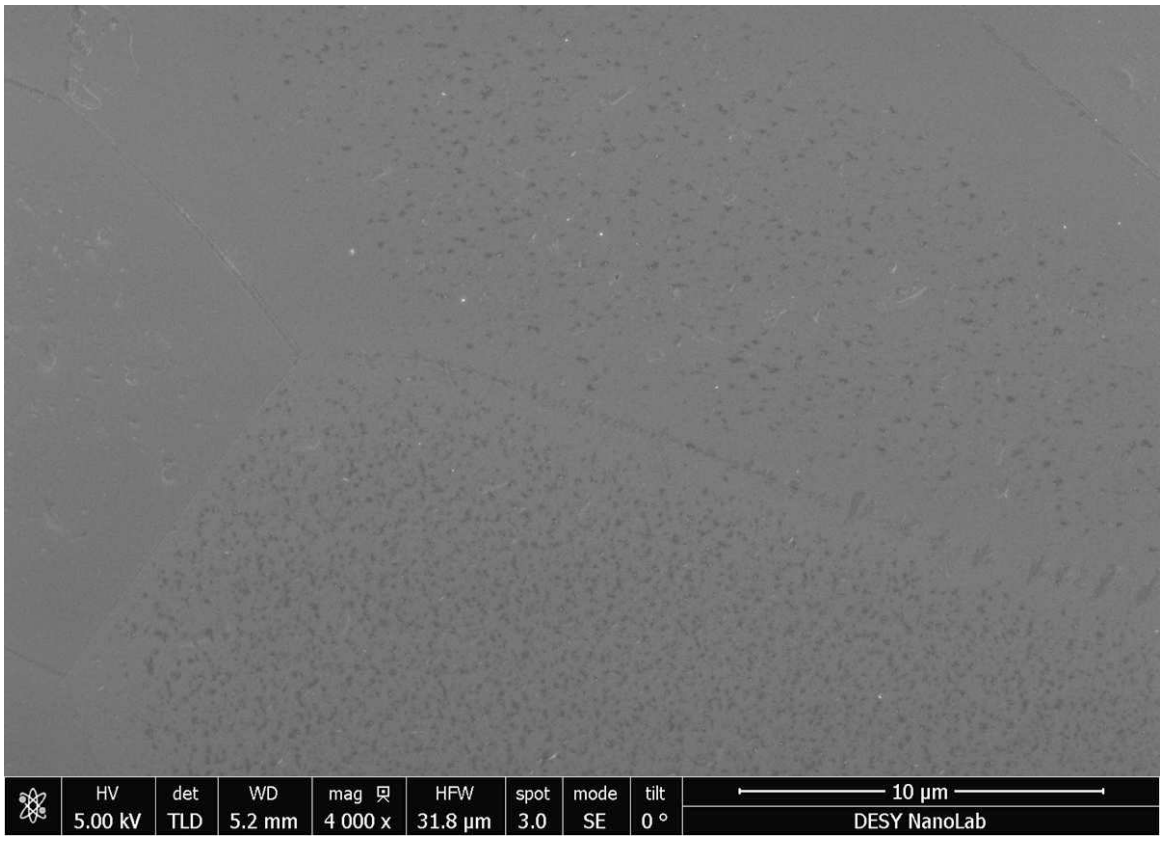

Figure 65: SEM image of witness sample from first nitrogen infusion of cavity 1DE27 inside the niobium box as LOS protection. Precipitation on two grains of the sample surface occurred.

The results presented here appear to contradict A. Grasselino's result [109], in which it was shown that LOS protection using niobium foils wrapped around the cavity flanges before 800°C baking without subsequent chemical surface removal improved performance. Hydrocarbons are very common in vacuum technology which is why each case must be considered individually. It seems likely that Fermilab's furnace was contaminated but the use of very clean caps helped against line-of-sight contamination, while both caps and furnace were contaminated in the present experiment. However, no degradation was observed after heat treatment at 800°C and subsequent 120°C in the first runs of 1DE16 (Fig. 56) and 1DE27 (Fig. 63) with caps. Only after the cavities, which had been BCP'ed before each run, were heat treated a second time without chemical treatment in between, did the performance degrade. Further heating the caps after BCP to between 800°C and 1000°C could help to solve the problem with performance degradation.
The XPS data showed more carbon in the sample from the 160°C infusion run but the SIMS results show a weaker carbon signal for the 160°C sample. However, this only applies to the samples that where within the Nb boxes. It is important to note that the SIMS and XPS analysis were carried out on different parts of the sample and therefore differences can be

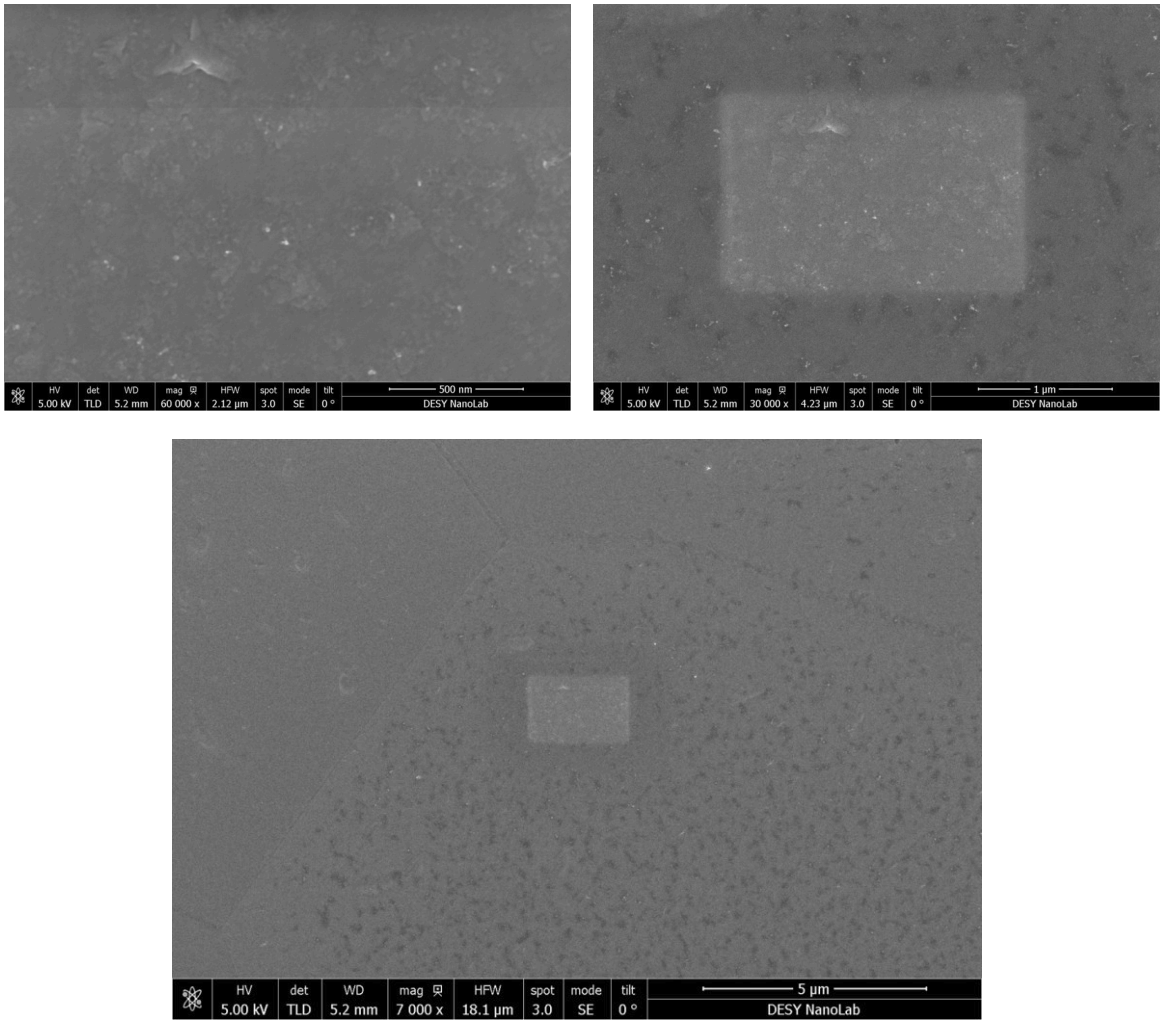

Figure 66: SEM images with different magnifications of a witness sample from the first nitrogen infusion of cavity 1DE27 inside the niobium box used as LOS protection.

expected. SEM images also show how grains differ from one another on the same sample in terms of their number and density of precipitates.

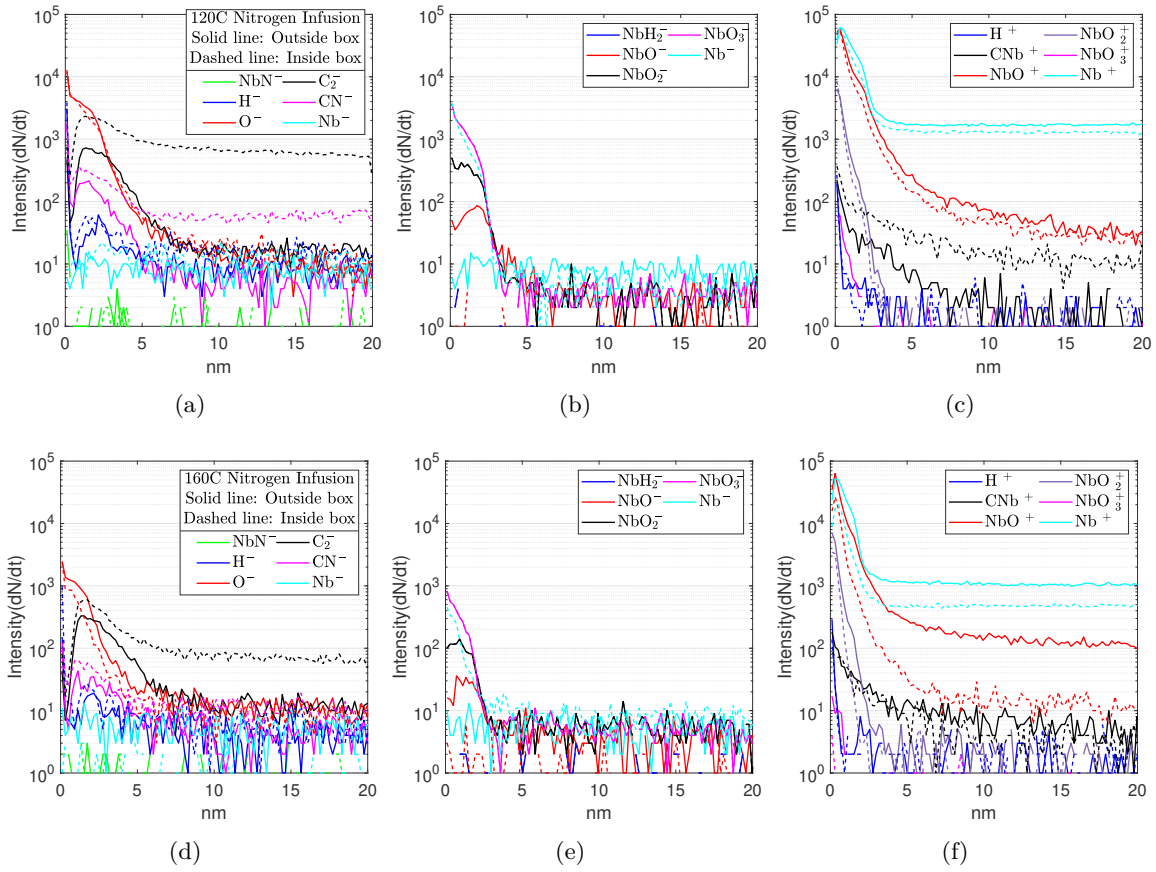

Figure 67: SIMS data of witness samples inside (dashed line) and outside the (solid line) niobium box from the first infusion of cavity 1DE27 at 120°C (a), (b) and (c) and from the 160°C nitrogen infusion (d), (e) and (f). A clear difference in the carbon signal (C_2^-, CN^- and CNb^+) between dashed and solid line is observed. The other elements show negligible difference between solid line and dashed line. No significant nitrogen signal is observed. The oxide and carbon signals from the sample outside the box show a layer of thickness about 6 nm, while for the sample inside the box, the carbon signal remains high also in the bulk.

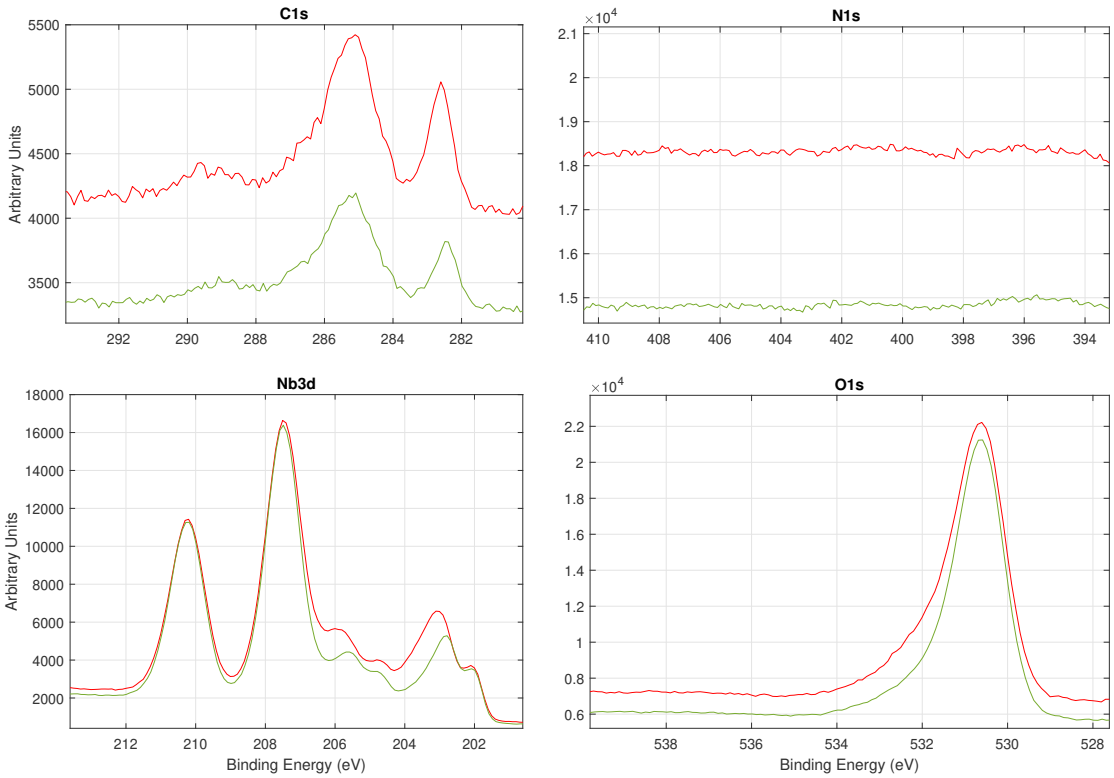

Figure 68: XPS measurement from samples of the 120°C nitrogen infusion (green curve) and of the 160°C nitrogen infusion (red curve) of cavity 1DE27. Both samples were treated inside the niobium box. A higher amount of oxygen and carbon is present for the sample which has been infused at 160°C. No nitrogen signal is present for either sample. The curves of C, N and O are offset in the vertical direction for clearer visibility. The vertical offset is entirely arbitrary and should be ignored since the important point are the positions of the peaks.

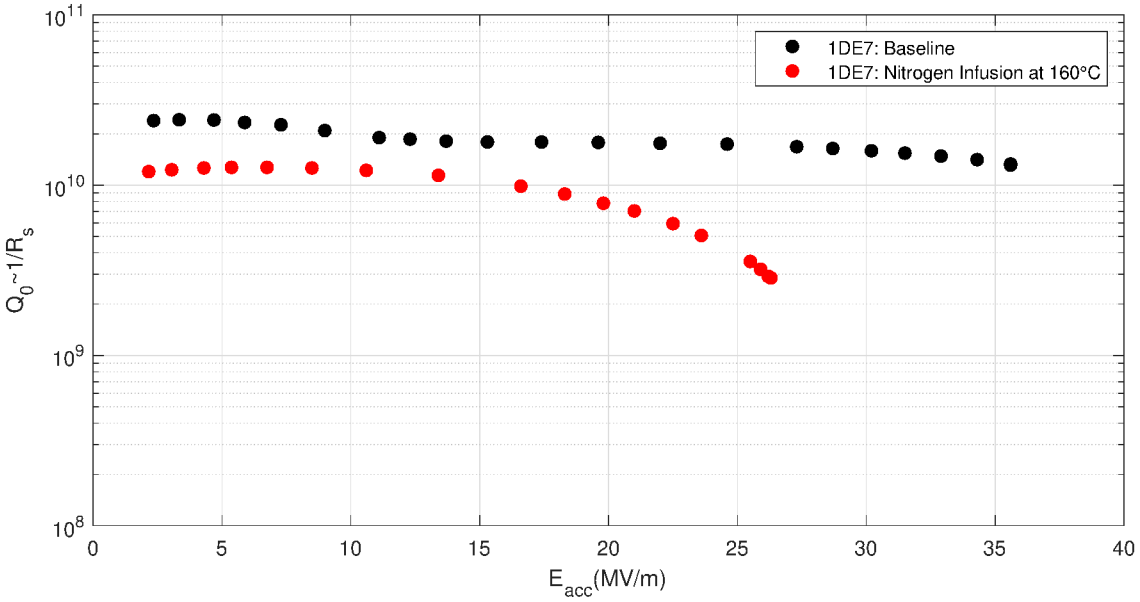

Figure 69: Cavity performance before and after nitrogen infusion at 160°C without post-chemical surface removal for cavity 1DE7. The black curves shows the baseline before the infusion and red shows performance after infusion. A degradation of Q_0 with voltage is observed while a drop in Q_0 is observed also for low fields. The shape of the curve after the infusion exhibits similarities to the 160°C infusion of cavity 1DE27 shown in Fig. 63. All curves shown were taken at 2 K.

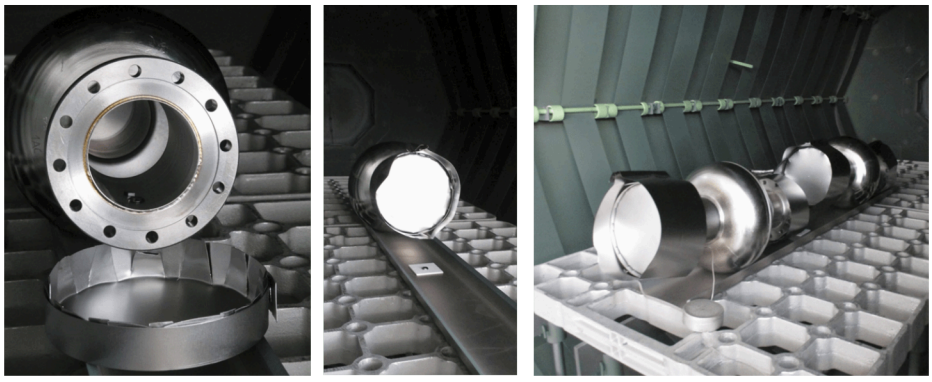

Figure 70: Cavity installation for the nitrogen infusion of 1DE7. For the LOS protection of one witness sample, a cavity (instead of a niobium box) was used, shown on the left picture. A second witness sample for comparison between with and without LOS is placed on a ceramic plate to ensure a clean support for the sample as shown in the middle picture. The picture on the right shows both the shielding cavity and cavity 1DE7 placed inside the furnace.

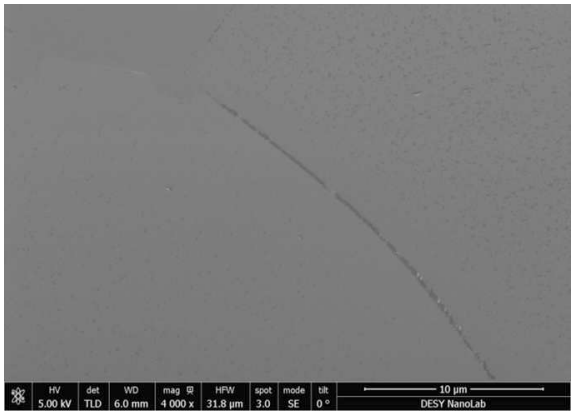

(a) Witness sample inside the screening cavity.

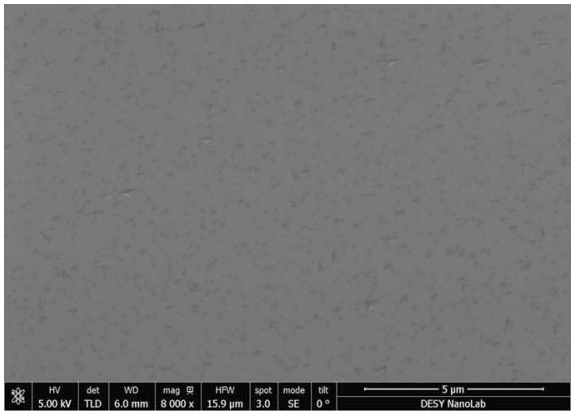

(b) Witness sample inside the screening cavity.

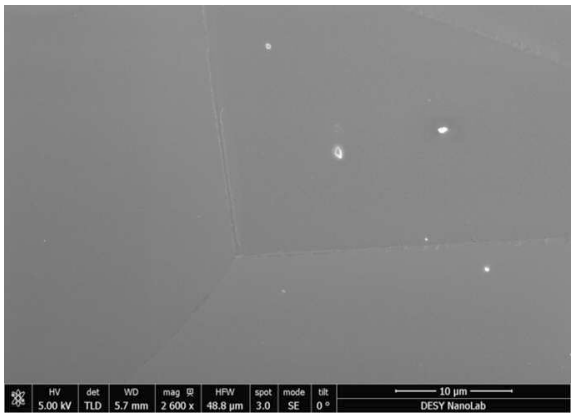

(c) Witness sample on a ceramic plate.

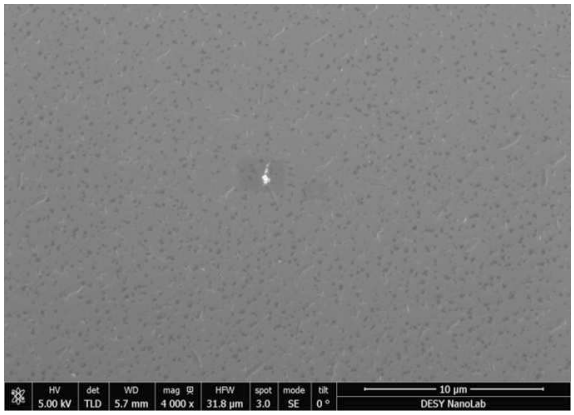

(d) Witness sample on a ceramic plate.

Figure 71: SEM images of two witness samples from 160°C nitrogen infusion of the cavity 1DE7. (a) and (b) are images from the sample infused inside the screening cavity and show precipitates that under higher magnification are star shaped. (c) and (d) show the sample on the ceramic plate which also shows precipitation on some grains but none on others. The bright white points are dust particles.

7.2.3 Carbides as source of contamination

It is still an open question how to correlate sample properties with cavities. Niobium carbides have been found on samples with LOS protection for two heat treatment runs (first run of 1DE16 and first run of 1DE27), after which the cavities did not degrade after the first heat or infusion treatment. For 1DE16, it was decided to cut the cavity open after the second heat treatment when it started to degrade. SEM images taken from the cutout-cavity inner surfaces are shown in Fig. 72. Carbides were found on the surface. It is unclear whether

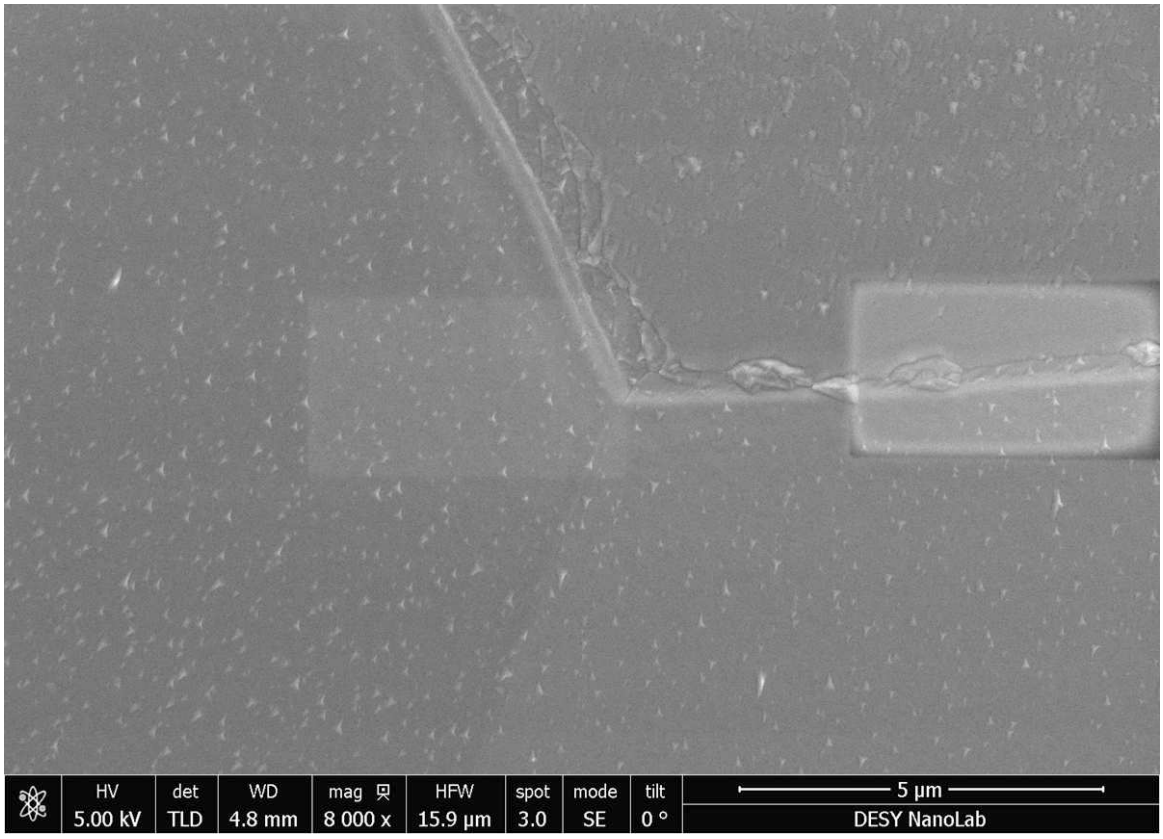

Figure 72: SEM image of the inner surface cutout from cavity 1DE16. The cavity was cut after a second heat treatment, after which the performance degraded as shown in Fig. 56. Very similar star-shaped precipitation to that seen on niobium witness samples is observed.

carbides formed already after the first heat treatment or just after the second. The carbides observed were between $50 - 400$ nm in size and therefore mostly smaller than nitrides after a nitrogen doping-recipe which grow to 2 μm on average in size when baked at 800°C with nitrogen gas for 20 minutes and 0.5 μm when baked for 2 minutes [80].
The cutouts of 1DE16 were examined in detail with respect to the crystal orientation [85] which established a connection between the amount of carbides and the crystal orientation via analysis of SEM images of the surface. For the cutouts of 1DE16, certain regions were selected using temperature sensors. By recording the temperature of the whole surface by

covering it with many temperature sensors (T-map system) during vertical test, regions of high dissipation can be identified. The regions that show local overheating are called hot spots. Other areas with minimal heating are called cold spots. Spots that are suspected to be the quench location by promoting the transition to the normal conducting state either from heating above T_c or due to exceeding the field of first penetration are called quench spots. Hot, quench and cold spots were examined and compared with one another. Carbide precipitation was found on all spots but it was found that the volume and area covered by niobium carbides have a relation to the local heating. Furthermore, XPS analyses of the samples revealed that the niobium-carbide signal was highest in the sample that included the quench spot.
The effects of thermal feedback on niobium carbides were studied. It was concluded that an increase in interstitial carbon can lead to a decrease in T_c, which in turn increases the surface resistance. The Nb_2C has a T_c of 1.98 K and can be superconducting until a certain breakdown field by proximity effect. This phenomenon is similar to Q-Disease caused by niobium hydrides (see sec. 1.5.4). Further investigations on the 1DE16 cutouts were presented in [113] and [111], which showed that more carbides have formed on grain boundaries when comparing quench and hot spots to cold spots. This led to segregation, i.e. enrichment of atoms, at the grain boundary, as the carbides penetrate into the grain boundaries. This could be an explanation for the anomalous Q-losses starting at low E_{acc} resulting from niobium grains decoupling within the RF layer.
These results suggest that niobium carbides are the cause of the performance deterioration. The fact that no improvement of any cavity which underwent infusion with nitrogen is observed, can be understood by the increased carbon contamination. In the bcc lattice of niobium, both interstitial carbon and nitrogen atoms prefer the octahedral configuration, with carbon having a lower binding energy than nitrogen [114]. Thus carbon penetrating the niobium during the 800°C phase will "shut out" nitrogen injection during the subsequent 120°C phase.

7.2.4 Pre-treatment of LOS protection structures

To understand the importance of pre-treatment of the LOS protection structures, another test with niobium boxes was performed in the sample furnace. Both boxes underwent a BCP, while only one was annealed at 1000°C beforehand. The box that was post annealed at 1000°C in the sample furnace under vacuum conditions was kept inside the furnace until it was vented for the experiment. Three BCP'ed niobium samples were used. One sample was placed on a bent piece of niobium so that the bottom of the sample was not touching the sheet over its full area. Another sample was placed inside the "BCP'ed only" niobium box and the third was placed in the "BCP'ed and pre-annealed" box (see Fig. 73). The samples then underwent a baking at 800°C for 2h. SEM images of the three samples are

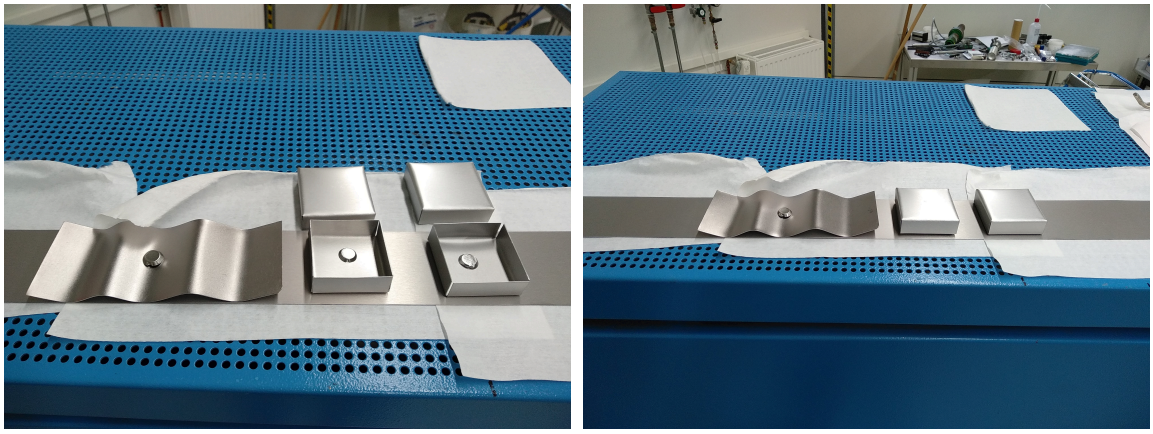

Figure 73: Sample placement for comparison experiment of differently pre-treated LOS protection. The picture on the right side shows the closed niobium boxes. The samples then underwent a baking at 800°C for 2h.

shown in Fig. 74.
The sample outside the boxes shows precipitation similar to previously observed carbides. The sample inside the "BCP'ed only" box shows some precipitation, especially at grain boundaries and on some grains. The sample inside the pre-annealed niobium box is completely free from any precipitation and has a clear smooth surface.

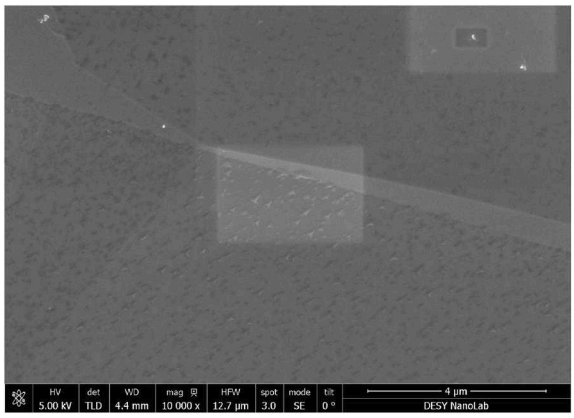

(a) Sample 75 with no LOS protection and thus exposed to the furnace vacuum.

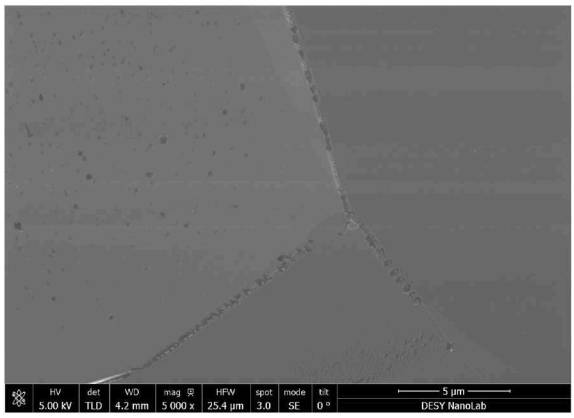

(b) Sample T1 placed under "BCP'ed only" niobium box.

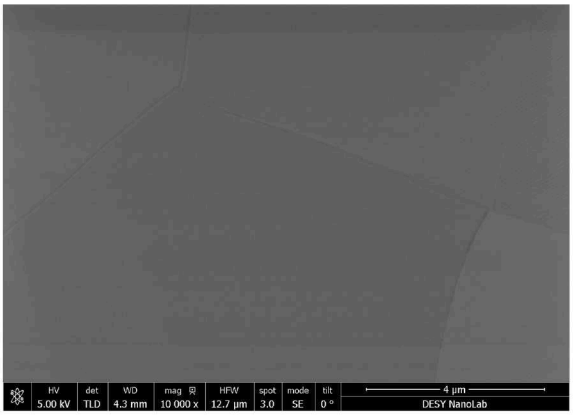

(c) Sample 80 placed under BCP'ed and pre-annealed at 1000°C niobium box.

Figure 74: SEM images of samples from the experiment illustrated in Fig. 73 pre-treated LOS protection. In total three samples were used. The sample without LOS protection (a) shows precipitation on the surface. The sample inside the "BCP'ed only" niobium box (b) shows some precipitates on certain grains and at grain boundaries. The sample inside the pre-annealed at 1000°C niobium box shows no precipitation and a very clean surface.

More EDX analysis has been carried out on the sample treated without LOS protection to gather more information about dark spots that accumulated on some spots of the sample surface. The particular investigated spot is shown in Fig. 75. The results of the EDX linescans are shown in Fig. 76. These investigations show that the dark areas observed on the niobium samples after heat treatment are thin carbon layers deposited on the first layers of the surface. There is evidence that the carbon displaces the oxygen from these areas, leaving less room for regrowth of oxygen layers. This is demonstrated by the oxygen signal. It can also be seen (a better example is shown in Fig. 75 (b)) that the areas avoid grain boundaries and that the carbon signal decreases on approach to a grain boundary

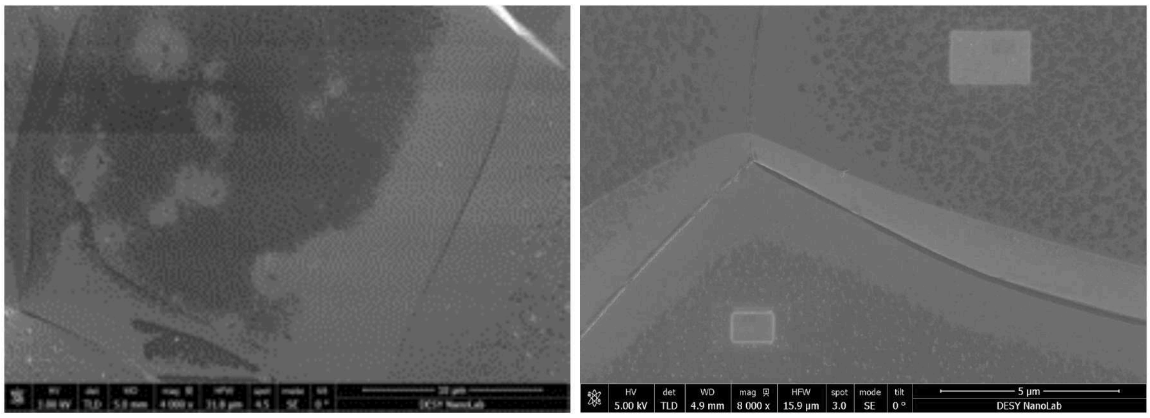

Figure 75: SEM image of sample placed without LOS protection and thus exposed to the furnace vacuum during 800°C baking.

indicating the adsorptive behaviour of these on carbon.
This is an important issue for future research. Further studies, which take these variables into account and apply them to cavities, will need to be undertaken. In summary, it has been shown that samples that have properly treated LOS protection, are protected against contamination.

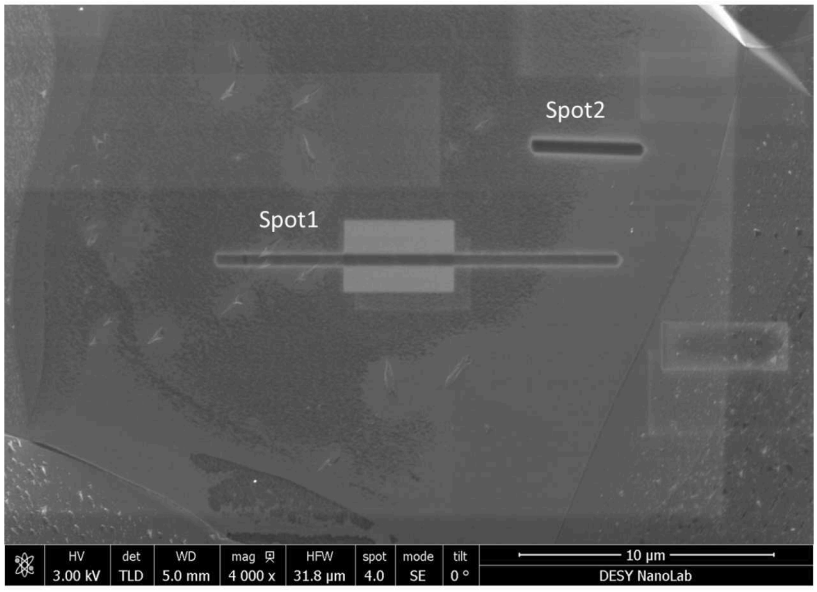

(a) EDX line scan spots of a niobium witness sample. The line scan charges the investigated area leaving visible marks.

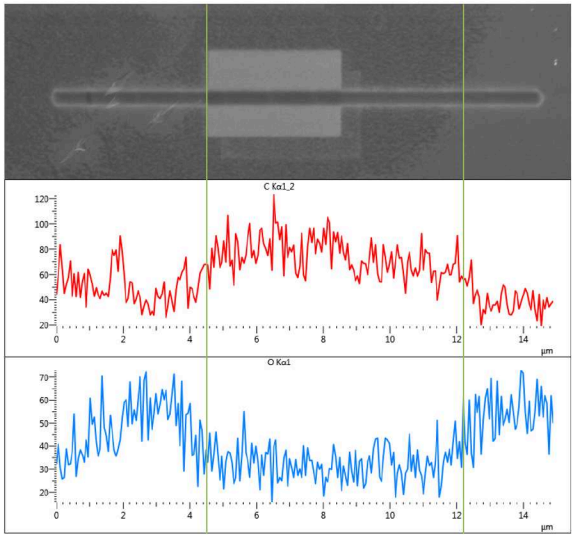

(b) EDX line scan of Spot 1 on a dark area that has been pre focused on which appears as the brighter window in the middle.

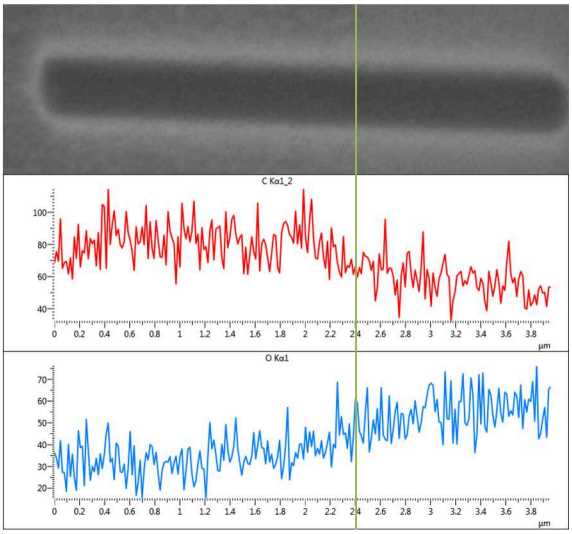

(c) EDX line scan of Spot 2 at the edge of a dark area.

Figure 76: EDX investigation of dark areas on a niobium witness sample after it was heat treated without LOS protection. In the carbon signal, a decrease at the boundary from the dark to the bright area can be seen, indicating a thin carbon layer that accumulated on the surface causing these dark areas. Furthermore, a decrease of the oxygen signal inside the dark area can be seen. This is confirmed by spot 2. This indicates that carbon diffuses into the grain boundaries.

7.3 Summary and conclusion

Several samples have been investigated for surface changes after heat treatments without any subsequent chemical cleaning. Star-shaped precipitates were found on samples as well as cavity cut-outs and are suspected to be the cause of cavity performance deterioration. Additionally, ToF-SIMS and XPS measurements indicated that samples baked in the furnace together with cavities where precipitates were observed by SEM, had a significant increase of interstitial carbon but absence of nitrogen. These precipitates were identified as carbon rich Nb_2C phases by TEM analysis utilizing electron diffraction. Our findings strongly suggest that carbides are the cause for the degradation, provided they are available in sufficient number and concentration, while the precipitation at grain boundaries is the most important factor in producing the degradation [111]. The precipitation of carbides was traced to the "line-of-sight" (LOS) protection that is used in the current nitrogen infusion recipe, but also in the nitrogen doping procedure. Of course, the cleanliness and partial pressure of the furnace vacuum itself also plays a role. Contrary to prior expectations, this study shows a strong correlation between carbide precipitation and the use of LOS protection (e.g. niobium foils or boxes) during heat treatment. However, cases are observed were carbides grew without LOS protection and thus must be attributed to other sources. The LOS protection during treatments can serve as a trap for a carbon-rich atmosphere, which is thus not pumped away. The results presented here emphasise the importance of ensuring that LOS protection caps have been cleaned and heated properly. The results suggest that the formation of carbides depends on the purity of the caps and the interior of furnace and the vacuum conductance, which depends on the tightness between caps and cavity flange. Modifying the caps to prevent LOS contamination while still having a well-defined conductance between furnace and cavity vacuum as a pathway for desorbed gases would be superior to the current system of flanges and cap fingers, which give non-reproducible conditions every time they are installed. Finally, it was clearly shown on the basis of samples that preheating niobium boxes as LOS at 1000°C prevents the occurrence of carbides despite contamination of hydrocarbons in the furnace. It therefore appears, that Fermilab must have succeeded because their caps were uncontaminated. It would therefore be extremely interesting to test this method on a cavity at Desy. The over-riding conclusion of this work is that the cleanliness of everything used in this process, furnace, caps etc. is of the highest importance.

8 Critical magnetic field of niobium samples

8.1 Introduction

Measuring magnetic properties on niobium samples might help to understand the underlying process of the surface treatments that improve cavity performance. As explained in sec. 1.4, for finite superconductors there is a transition to superconductivity even with fields greater than H_{c2}, which is denoted as H_{c3}. According to Saint-James and De Gennes [38] $H_{c3} = r \cdot H_{c2}$, where r is a proportionality factor which depends on the sample surface characteristics. It was shown by Saint-James and De Gennes that superconductivity nucleates at a metal-insulator interface in a parallel field H_{c3} that is higher than H_{c2} by a factor $r_{GL} = 1.695$, according to the Ginzburg-Landau theory [39]. This is obtained by solving the linearized Ginzburg-Landau equation in the presence of a plane boundary that provides a mirror image of a potential. For fields between H_{c2} and H_{c3}, superconductivity appears in a surface sheath of thickness ξ. For pure niobium, surface superconductivity and electromagnetic losses of microwave fields are observed in thin surface sheaths of about the same thickness, since the ratio $\kappa = \lambda_L/\xi$ (see sec. 1.3) between the coherence length ξ and the penetration depth λ_L, is in the order of unity. It is therefore quite conceivable to be able to make statements about correlations between surface superconductivity and cavity performance after different surface treatments.

In [115], experimental studies on the magnetization and susceptibility of niobium samples were carried out to observe the dependence of superconducting properties in this sheath after various treatments that are also applied to cavities, like buffered chemical etching (BCP, sec. 2.1.1), electrolytical polishing (EP, sec. 2.1.2) and low-temperature baking (LTB). It has conclusively been shown that they all have a large impact on H_{c3}, which is associated with a change of electronic mean free path, l, due to impurities in a surface layer. The evidence presented in this study suggests that H_{c3} can be increased by removing a layer of $80 - 160$ μm through EP. A further increase has been achieved by annealing the samples under ultra-high-vacuum conditions (UHV) at 120°C for 48 hours. Furthermore, the variation of annealing temperatures from 100°C to 144°C showed an increase in H_{c3} with higher temperature. Between 100°C to 123°C, H_{c3} increased with longer annealing time between 24 and 96 hours. At 144°C, the increase stopped at 24 hours.

In the current study, measurements were carried out on Nitrogen-infused samples to determine whether nitrogen infusion has an influence on H_{c3}. It is assumed that only the first few nanometers are affected by nitrogen infusion. It is therefore obvious that the nitrogen infusion could also cause a change in the surface superconducting properties.
There are only a few studies to date that have dealt with the influence of nitrogen on H_{c3}. A summary of the current status of the results can be found in [116]. These results actually show changes in the H_{c3} of niobium samples after nitrogen treatment. It is now well established from a variety of experimental studies that the ratio factor $r = H_{c3}/H_{c2}$ for several niobium samples is larger then the predicted theoretical $r_{GL} = 1.695$.

The investigation of the superconducting properties of Niobium samples was carried out in collaboration with TU WIEN (Technischen Universität Wien) [117]. The provided sam-

ples and their treatments are listed in table 9. The samples were rinsed with Ethanol and further rinsed at high pressure with deionized water (see sec. 3) between chemical and heat treatments. All samples were from a leftover European XFEL production sheet provided by Tokyo Denkai Co Ltd. Two of the samples were nitrogen infused at 120°C at DESY together with cavity 1DE10, whose performance after the treatment is shown in sec. 5.2.1 in Fig. 38. Sample U was left completely untreated and serves as a reference for the raw material. The impurity content from the ingot from which the sheet was cut is listed in table 10.

Table 9: Provided samples for superconducting quantum interference device (SQUID) measurements at TU WIEN. Sample U is a raw untreated sample.

Sample No.	**Chemical polishing**	**Pre-Annealing**	**Last treatment**
60	BCP	✗	N-infused
65	EP	800°C(3h)	✗
67	EP	800°C(2h) + 120°C(48h)	N-infused
62	EP	✗	✗
U	✗	✗	✗

Table 10: Impurity contents listed by the manufacturer of the ingot from which the sheets for the samples listed in table 9 have been made. A RRR of 323 is specified for that ingot. The interstitial impurities for O, N, H and C have been specified for one of the sheets cut from that ingot. That particular sheet had a measured RRR of 302 as given on a data sheet.

	ppm $[\mu g/g]$		**ppm** $[\mu g/g]$
Ta	27	O	3.5
W	<10	N	4.4
Ti	<10	H	1.2
Fe	<10	C	0.7
Si	<10		
Mo	<10		
Ni	<10		

8.2 Resistivity measurement

A resistivity measurement was carried out by four-terminal sensing based on Ohm's Law. The electrical resistance R was determined by supplying the samples with a known current I via two outer lines while simultaneously a voltage U across the sample was measured via the two inner lines (see Fig. 44 in sec. 5.3).
This method was used to determine the critical temperature T_c and critical magnetic field H_{c2} for sample 60 and 62 (see table 9), since the phase transition caused by crossing either of these transitions will increase the resistance and hence, the measured voltage. The samples

were cooled by liquid helium inside a cryostat. It was possible to apply a magnetic field using a superconducting 17 T Hybrid Magnet consisting of Nb_3Sn with outer windings made of NbTi. The cryostat had a VTI (Variable Temperature Insert) which was shielded by vacuum from the helium bath. The temperature of the sample chamber could be controlled between 2 and 150 K. For temperatures above the boiling point of liquid helium (4.2 K), a pump generates a negative pressure difference inside the VTI to let liquid helium into the VTI via a needle valve. The liquid helium evaporates and is heated by heating coils to the desired temperature [117]. A dedicated sample holder with spring-loaded gold pins was used to protect the sample surface. As mentioned above, the four-point-probes method (four-terminal sensing) was used, similar to that described in sec. 5.3.
The general measuring procedure consisted of the voltage measurement (and hence resistance measurement) in a so-called delta mode, a current-reversal technique to cancel the effects of thermal electromagnetic fields in the voltmeter test-lead connection. Starting above T_c, the temperature was lowered by intervals of $\Delta T = 0.05$ K until the desired temperature was reached. The desired magnetic field could be applied using the 17 T Hybrid Magnet.

8.2.1 Results

Sample 60 was measured with applied magnetic fields of 0 mT, 100 mT and 250 mT at a current of 100 mA and 50 mA, as shown in Fig. 77. The value for T_c was determined as the

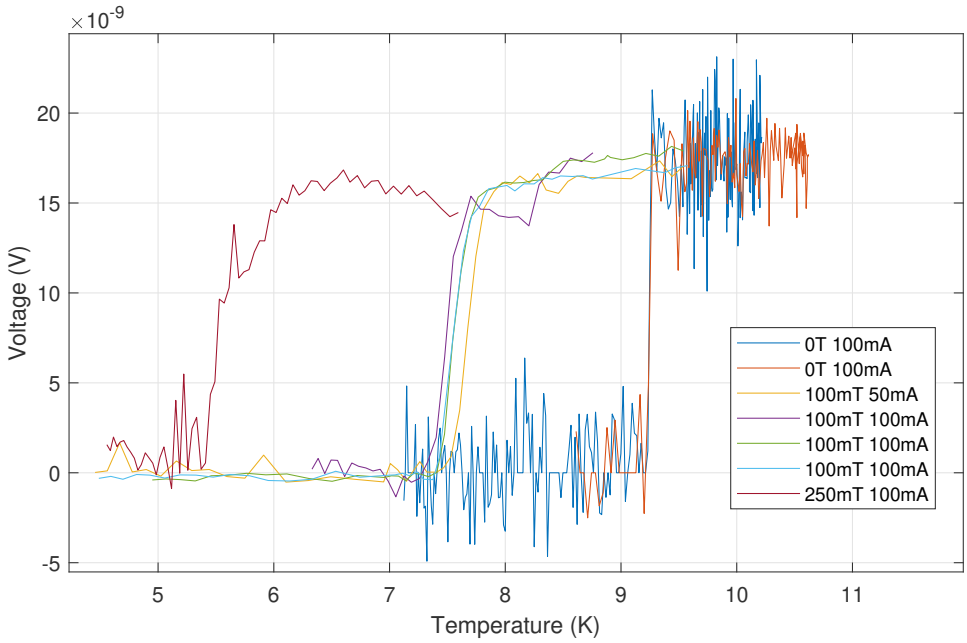

Figure 77: Transport flow measurement of Sample 60 at applied current of 100 mA and 50 mA and magnetic fields of 100 mT and 250 mT.

mid-point of the resistivity transition from the normal to the superconducting state. In the resistance vs. temperature curve, a tangential line to the normal state region can be drawn as shown in Fig. 78. The temperature at 50% height of the tangential line is defined as T_c. The difference ΔT_c between 90% and 10% of the tangential lines denotes an estimate for the error for T_c [118].

From the measurements in Fig. 77, a critical temperature T_c of (5.51 ± 0.27) K at 250 mT,

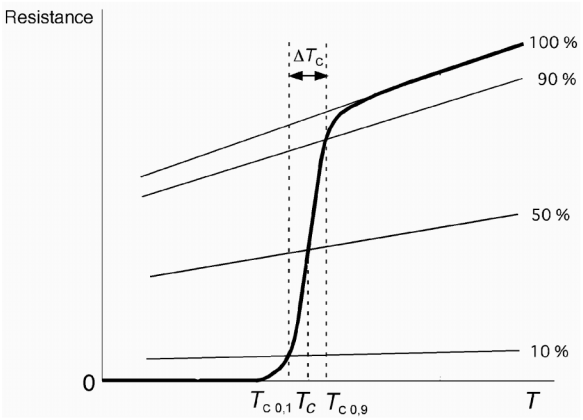

Figure 78: Determination of T_c [118].

of (7.58 ± 0.08) K at 100 mT and of (9.245 ± 0.011) K without field are determined. This allows the temperature-dependent critical magnetic field $H_{c2}(T)$ to be estimated via

$$H_{c2}(T) = H_{c2}(0) \cdot \frac{1 - (T/T_c)^2}{1 + (T/T_c)^2}. \tag{16}$$

The measured critical magnetic fields and the empirical fit from eq. 16 was shown in Fig. 80. The resistivity measurements with a field of 100 mT have been repeated to reduce the statistical uncertainty, giving a $H_{c2,\#60}(0) = (511 \pm 21)$ mT.

Since sample 60 has already received a heat treatment by the nitrogen infusion, a further sample (62) which only received an EP was measured for comparison. Since H_{c2} is a bulk property, it should be verified whether the treatment at such a high temperature has any influence on it. Sample 62 was measured with applied magnetic fields of 0 mT, 100 mT, 150 mT, 250 mT and 250 mT at a current of 100 mA as shown in Fig. 79. The values for the critical field H_{c2} with a empirical fit is shown in Fig. 80 and give a $H_{c2,\#62}(0) = (528 \pm 26)$ mT. This value agrees with that of the sample 60 within the measuring accuracy, which indicates that the heat treatment during an infusion does not drastically change the H_{c2}. It is therefore assumed that approximately the same H_{c2} can be expected for all samples. The mean of the two measured samples is used for further calculations henceforward, with $H_{c2} = (518 \pm 16))$ mT.

8.3 AC-susceptibility measurement

The AC magnetic-susceptibility measurement was used to characterize superconducting parameters in the niobium samples mentioned in table 9. A Quantum Design MPMS-XL Magnetometer based on a superconducting quantum interference device (SQUID) Detector

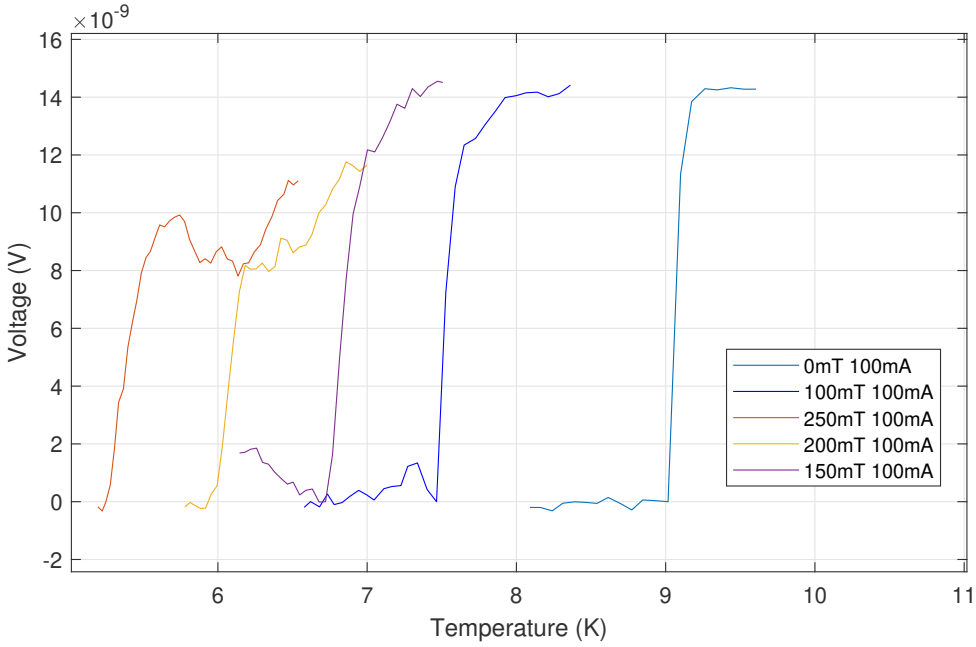

Figure 79: Transport flow measurement of Sample 62 at applied current of 100 mA and 50 mA and magnetic fields of 100 mT and 250 mT.

was used. The magnetic moment can be measured with a sensitivity of $1 \cdot 10^{-10}$ Am^2. According to [117], the alternating-field susceptibility measurement is carried out by superimposing a DC magnetic field with a small AC magnetic field $H = H_{AC}\cos(wt)$ (where $w = 2\pi f$ corresponds to the angular frequency), which causes a time-dependent magnetic moment in the sample. The sample is placed in the center of a detection coil. The magnetization M of the sample changes due to the periodically changing magnetic field. Thus the measured signal is sensitive to the change in $M(H)$ and hence the AC susceptibility $\chi_{AC} = dM/dH$ gives an indication of the slope of the magnetization curve. The time-dependent magnetization M of the sample can be described by the harmonic sum

$$M = H_{AC} \sum_{n=1}^{n=\infty} (\chi'_n \cdot \cos(nwt) + \chi''_n \cdot \sin(nwt)),$$

where χ'_n and χ''_n correspond to the in-phase (real) and out-of-phase (imaginary) parts of the AC susceptibility and H_{AC} is the amplitude of the applied AC magnetic field. The integer n is the harmonic order. However, the magnetometer device used here applies a Fast Fourier Transformation (FFT) and uses the fundamental oscillation only ($n = 1$). Therefore χ'_n and χ''_n are denoted as χ' and χ''. The real part χ' corresponds to the dispersive magnetic reaction while the imaginary part χ'' corresponds to the energy dissipation. Together they form the complex magnetic susceptibility, $\chi = \chi' + i\chi''$, which is nearly zero for the normal conducting state. However, in the superconducting state, the superconductor behaves like an ideal diamagnet, which corresponds to a susceptibility of $\chi = -1$.
The conical sample (see sec. 3) is too large for the magnetometer. Therefore the samples

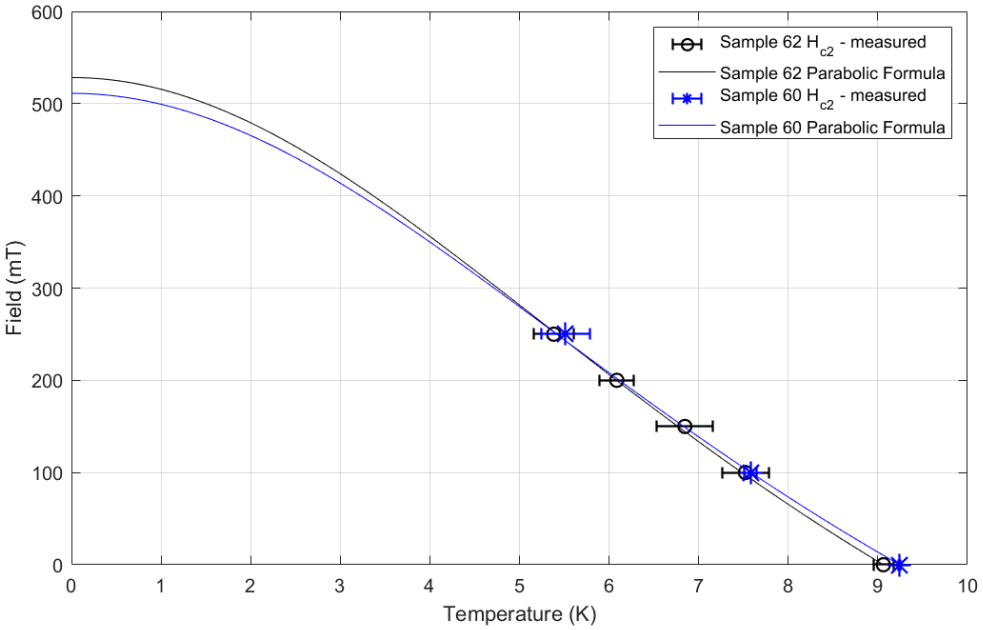

Figure 80: Measured H_{c2} from transport flow measurement of Sample 60 and 62 and the fit by eq. 16.

were cut by a diamond saw into $(2.5 \cdot 2.5 \cdot 2.5)$ mm^3 cubes. This means that the samples only have one side with a treated surface. Two samples were cut in half again to have a comparison between the surface-treated upper (Sample 60-u and 67-u) and the untreated lower (60-l und 67-l) half side of the sample.
The sample masses produced are listed in table 11.

Table 11: Masses of the samples obtained [117].

Sample No.	Mass (g)
U	0.1208
60	0.1441
65	0.1296
67	0.1147
67-u	0.0481
67-l	0.0666

8.3.1 General measuring procedure

After the samples were cooled to the desired temperature, an external magnetic field was applied and the AC susceptibility measurement carried out by gradually lowering the external magnetic field. Therefore, χ' and χ'', and thus also the real and imaginary parts of

the magnetic moment $m' = H_{AC} \cdot \chi' \cdot V$ and $m'' = H_{AC} \cdot \chi'' \cdot V$ can be determined as a function of the external magnetic field, where V is the volume of the sample.
Comparison values are obtained from S. Casalbuoni et al. [115]. Following their interpretation, the critical magnetic field of the surface superconductivity H_{c3} of the sample can be determined using the "onset" of an excess shielding $(\chi' - \chi'_{normal})$. The phase transition from the normal to the superconducting state is indicated by the onset of screening, which is the beginning of a significant change in the measurement signal, of a non-zero $|\chi'|$ above the susceptibility value in the normal state χ'_{normal}; hence the start of the growth of $|\chi'|$ defines H_{c3} [115] [119]. The publication shows results on niobium samples for different surface processes that are also applied on cavities.

8.3.2 Results

The samples 60, 65, 67 and U were measured at a temperature of 5 K. For the alternating-field, an amplitude with $H_{AC} = 1$ μT and frequency $f = 10$ Hz were chosen to create a comparison with [115]. The values m' and m'' obtained by the measurement correspond to the real and imaginary parts of the magnetic moment of the sample. Since the samples have different masses, the results of the measurements were multiplied by a weight factor $g = m_U/m_x$, where m_U corresponds to the mass of the reference sample and m_x to the masses given in table 11.

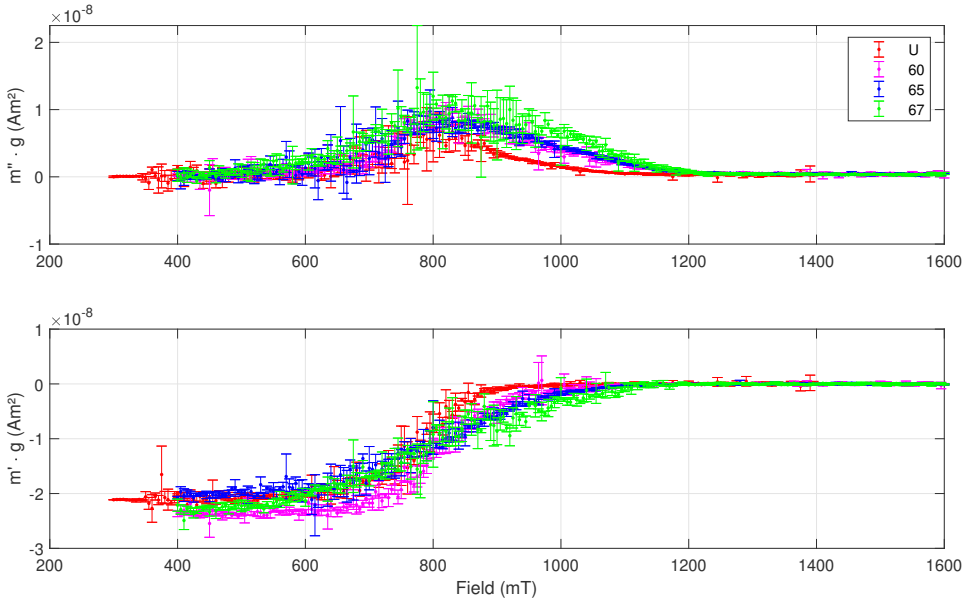

Figure 81: Real (re) and imaginary part (im) of the alternating-field susceptibility measurements of sample 60 compared to the untreated reference sample U. The results are re-normalized by multiplying with a weighting factor $g = m_U/m_x$ with the masses given in table 11.

The treated samples differ significantly from the reference sample U, as shown in Fig. 81.

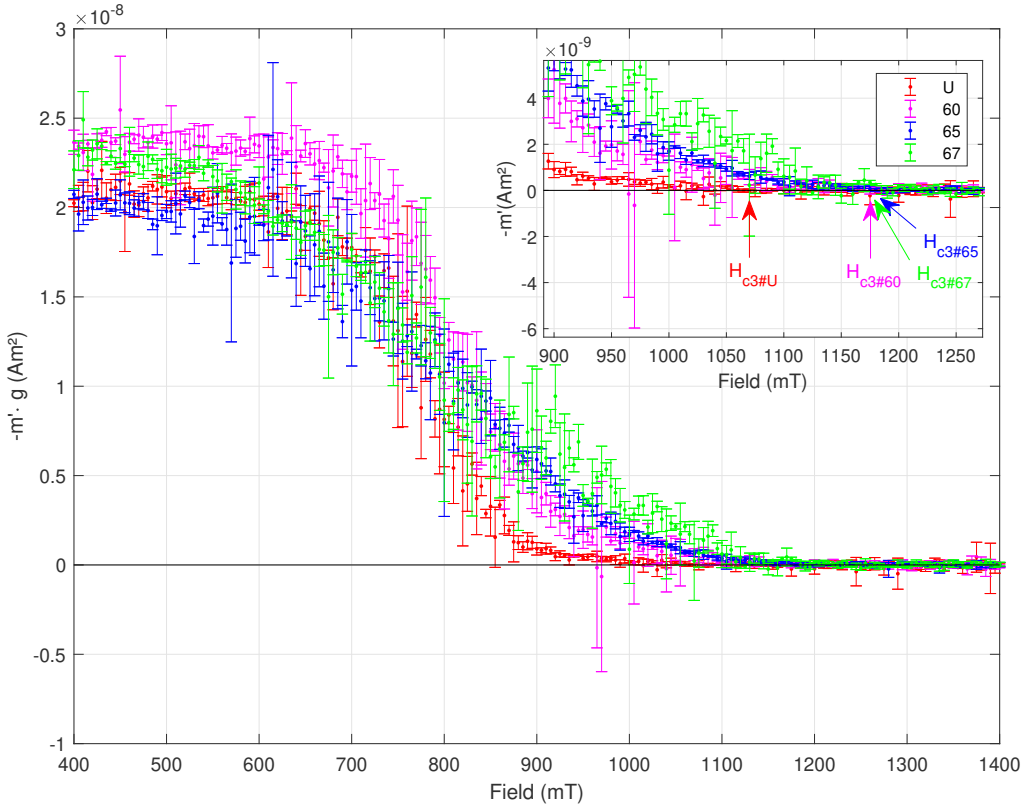

Figure 82: Negative real part of the alternating-field susceptibility measured on samples U, 60, 65 and 67. The surface nucleation field H_{c3} determined by the onset of excess shielding $m' - m'_{normal}$ where m'_{normal} is the real part of m in the normal state, is indicated by the arrows. The results are re-normalized by multiplying with a weighting factor $g = m_U/m_x$ with the masses given in table 11.

However, a direct comparison between the treated samples 60, 65 and 67 shows that the critical magnetic fields H_{c3} defined by the onset of m' are hardly distinguishable. The deviations in the signals for fields below H_{c3} can be due to differences in the geometry (the deviations in the masses in table 11 also indicate deviations in the dimensions of the cutouts) of the samples, since the magnetic fields can then be distorted. However, this has no effect on the onset of the shielding.
As suggested by [115], the onsets to obtain the values for H_{c3} were estimated by plotting the real parts m' of the measured signal as shown in Fig. 82.
To determine whether the treatment of the surface, or a bulk effect of the superconductor makes a difference, sample 67 was halved. A sample with a treated surface (67-u) and one without (67-l) were thus obtained and could be compared directly with one another.
As can be seen in Fig. 83 and 84, there is no significant difference in the critical magnetic field H_{c3} defined by the onset of m', although the overall shape of the two curves is clearly different for m''. The results of H_{c3} for all samples are listed in table 12.
In order to show H_{c3} as a function of temperature, further measurements of the upper half

Table 12: Obtained values for the surface nucleation field H_{c3} from susceptibility measurement for all the samples as shown in Fig. 82 and 84. An error of ±50 mT is estimated for the determination of H_{c3} via the onset of m'.

Sample	$H_{c3}(T = 5\ \mathrm{K})$ in mT
U	1055
60	1165
65	1175
67	1200
67-l	1077
67-u	1032

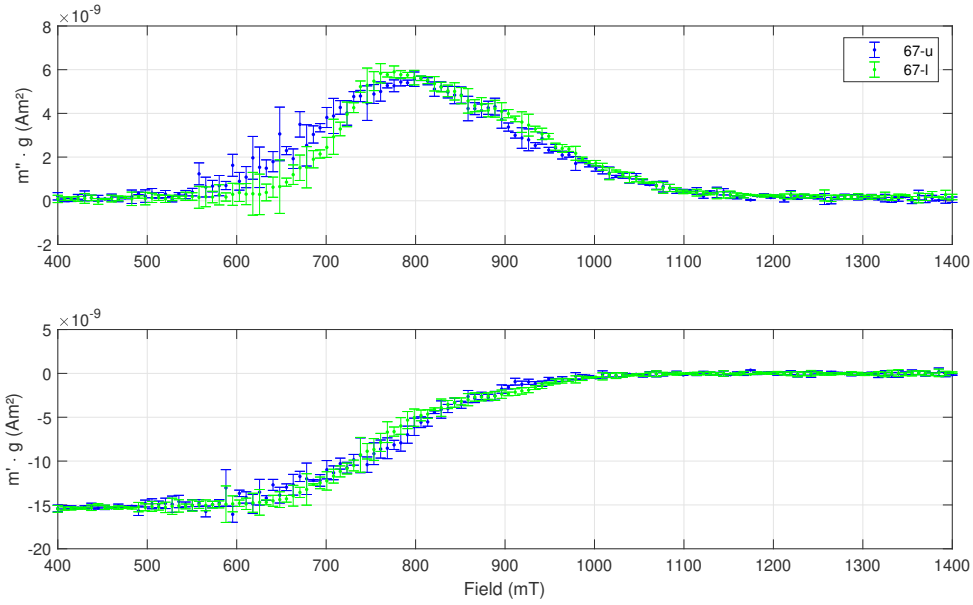

Figure 83: Real (m') and imaginary part (m'') of the alternating-field susceptibility measurements of the upper half (u) and the lower half (l) of sample 67. The results are re-normalized by multiplying with a weighting factor $g = m_U/(2 \cdot m_{67-u/l})$ with the masses given in table 11.

of sample 67 (67-u) at temperatures of 6, 7 and 8.5 K were made. The remaining parameters of the measurement and the general measurement procedure were retained.
For temperatures below the superconducting transition temperature (T_c) in homogeneous superconductors, electric current flows without any resistance. In spite of that, if a magnetic field is present inside the superconductor, an applied electric current can interact with quantized magnetic fluxons, giving rise to flux dynamics which will lead to energy dissipation, resulting in electrical resistivity. If the flux lines can move freely, so called reversible behaviour occurs. If many strong flux-pinning centers are present within the supercon-

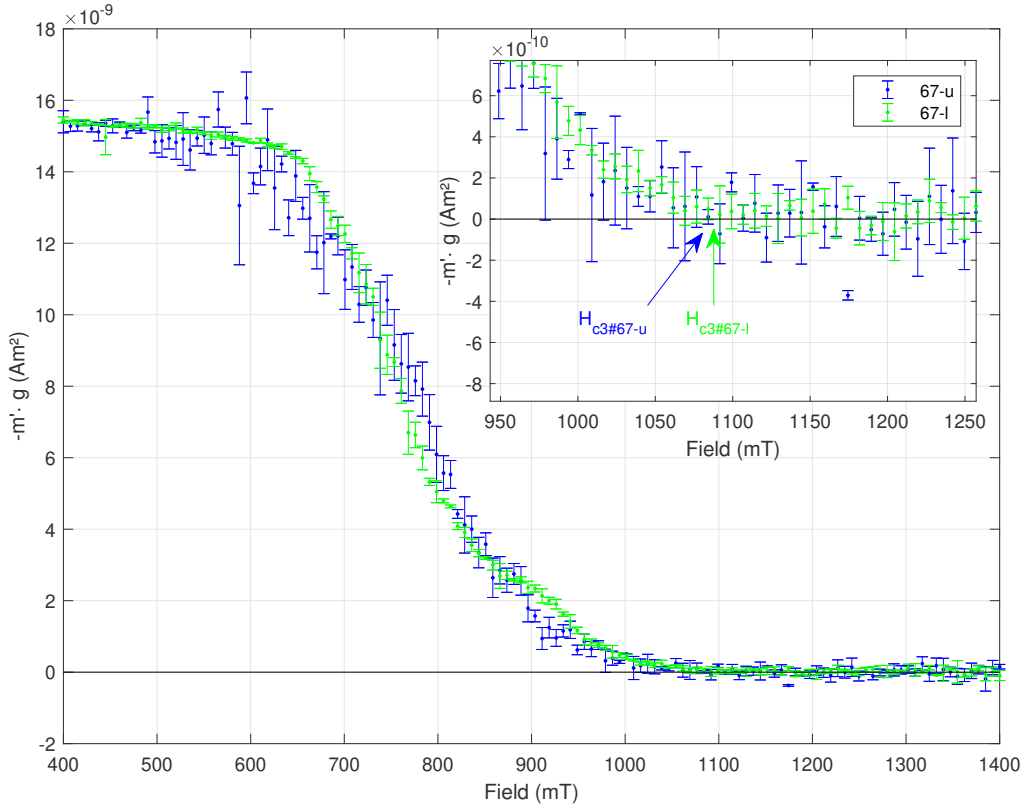

Figure 84: Negative real part of the alternating-field susceptibility measured on samples 67-u and 67-l. The surface nucleation field H_{c3} determined by the onset of excess shielding $m' - m'_{normal}$ where m'_{normal} is the real part of m in the normal state, is indicated by the arrows. The results are re-normalized by multiplying with a weighting factor $g = m_U/(2 \cdot m_{67-u/l})$ with the masses given in table 11.

ductor, the flux dynamics can be suppressed by flux pinning, enabling the flow of electric current without dissipation. However, for temperatures just below T_c, the pinning is too weak to suppress flux dynamics. This is only accomplished along a boundary in the field temperature plane $H - T$ at a certain range below T_c known as the magnetic irreversibility line, $T_{irr}(H)$, which divides the $H - T$ phase diagram into two regions. Above the line, the magnetic moment of the superconductor shows reversible behaviour. Below the line, due to the anchorage of the magnetic flux, it is in an irreversible phase as long as $H > H_{c1}$ applies. A type II superconductor below its irreversibility temperature T_{irr} shows a irreversible magnetic moment. For very small superconducting volumes close to the surface with a layer thickness $d \leq \xi$ (as is the case with surface superconductivity), an irreversible magnetic moment may also be involved.
To determine whether surface or whether volume superconductivity contributes to the magnetization hysteresis, $M(H)$ of sample 67-u was measured. Figure 85 shows the magnetic moment as a function of increasing and decreasing field. The course of the curve as shown in Fig. 85 indicates magnetization of the bulk of the superconductor roughly up to the

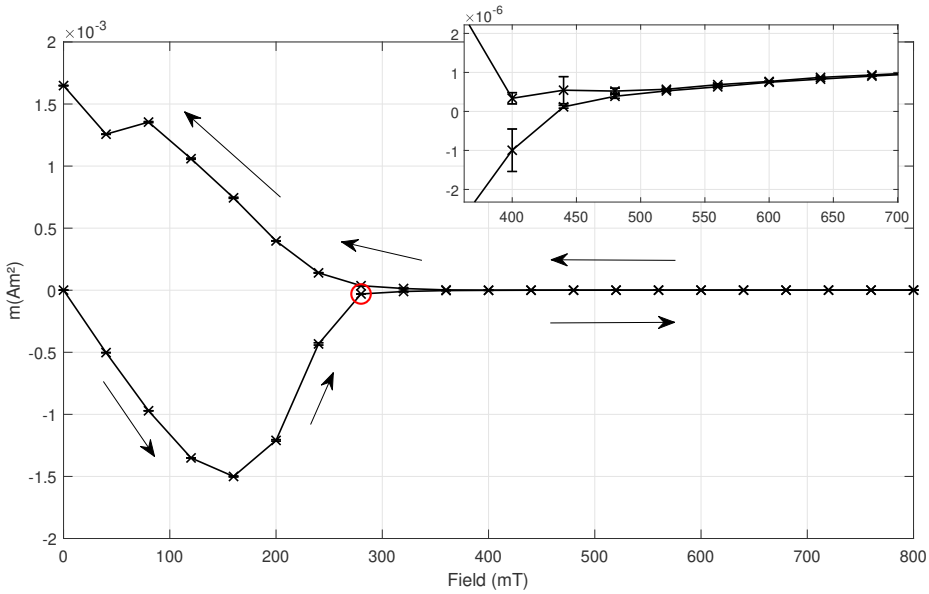

Figure 85: Measured hysteresis loop of the magnetic moment of sample 67-u as a function of the applied field at 5 K. The arrows show the direction of field variation. The zoomed-in region in the inset shows that a small magnetic moment above H_{c2} persists that cannot be explained by volume superconductivity. The point at which the slope seems to change abruptly is at 280 mT (circled in red) and therefore the critical point is approximately $H_{c2,\#67-u}(5\text{ K}) = 280$ mT. The equation 16 then implies $H_{c2,\#67-u}(0\text{ K}) \approx 512$ mT. Error bars are mostly smaller than the symbol size.

data point at 280 mT due to the change of slope, which is suspected to corresponds to $H_{c2}(5\text{ K})$. This is not an exact measurement to determine H_{c2} but gives us a comparison value to our already measured H_{c2} of the other samples. Thus, equation 16 implies $H_{c2,\#67-u}(0\text{ K}) \approx 512$ mT. Observing a non-zero magnetic moment for fields above 280 mT i.e. H_{c2}, cannot be explained with a reversible magnetization caused by bulk superconductivity. A continuous transition from bulk to surface superconductivity, which ends at H_{c3}, is necessary to explain this observation [117]. Although this is a rough approximation, the value obtained for the upper critical field $H_{c2,\#67-u}(0) = 512$ mT agrees with the value obtained from the resistivity measurements $H_{c2,\#60}(0) = (511 \pm 21)$ mT from sample 60 and with $H_{c2,\#62}(0) = (528 \pm 26)$ mT from sample 62. Figure 86 shows the measured values obtained for the sample 67-u and the curves of H_{c2} and H_{c3} determined by equation 16. This gives a proportionality factor of $r = 3.6 \pm 0.18$.

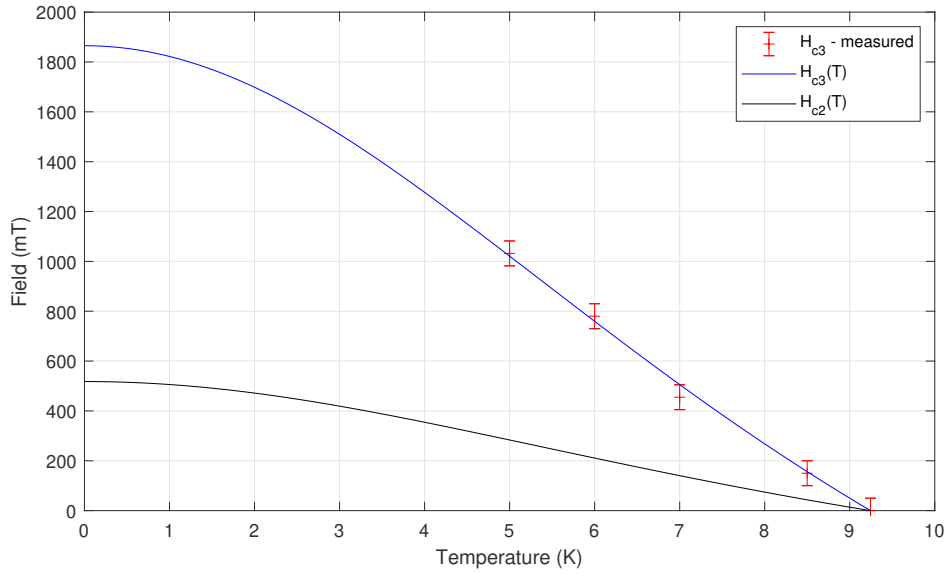

Figure 86: Measured H_{c3} of sample 67-u as a function of the temperature. Also shown is equation 16 (blue and black line) following $H_{c2}(T)$ with $H_{c2}(0\ \mathrm{K}) = (518 \pm 16))$ mT from the resistivity measurement and $H_{c3}(T)$ with $H_{c3}(0\ \mathrm{K}) = (1870 \pm 70)$ mT from the values obtained by the susceptibility measurement; $H_{c3} = r \cdot H_{c2}$ gives $r = 3.6 \pm 0.18$.

8.4 Discussion and Conclusion

Measurements were carried out on niobium samples whose surface has been treated with a buffer chemical polishing (BCP) or electropolishing (EP).
The nucleation field H_{c2}, has been determined for sample 60 and 62 via four terminal sensing to be $H_{c2,\#60}(0) = (511 \pm 21)$ mT and $H_{c2,\#62}(0) = (528 \pm 26)$ mT. A value of $H_{c2,\#67-u}(0) = 512$ mT can be estimated by field variation magnetization measurement as a very rough approximation through the slope of the curve in Fig. 85.
It is not surprising that the values for samples 60 and 67 agree with each other, despite their different surface treatment, since H_{c2} is a bulk property.
It was shown by [115] that low-temperature baking in the range of 100°C to 144°C has no significant influence on H_{c2}.
Here the only treatment step that could have influenced H_{c2} is the 800°C baking. However, since a 800°C baking in vacuum conditions is included in the nitrogen-infusion treatment, it is not expected that any difference in bulk properties between sample 60 and 67 would occur. Therefore, sample 62 was additionally measured via four terminal sensing since it only received an EP but again, the values of H_{c2} agree with each other. Furthermore the result from sample 67 shows that there is no significant difference in H_{c2} if an additional pre-treatmant of baking at 800°C and 120°C before the nitrogen infusion is applied.
With the help of the alternating-field susceptibility measurement, it can be shown that superconducting effects can be detected even with magnetic fields $H > H_{c2}$ and from this the superconducting properties of a surface layer within a thickness of order of the coherence length can be inferred. This corresponds to the ratio of $H_{c3} = r \cdot H_{c2}$ predicted by St. James and De Gennes [38] by solving the Ginzburg-Landau equation as already described in sec. 1.4. The comparison of the untreated sample with the differently treated samples (Fig. 82) shows that the treatment of the samples visibly increases the surface superconductivity critical field H_{c3}. The proportionality factor obtained for sample 67-u, $r = 3.6 \pm 0.18$ (Fig. 86) is much larger than was predicted by St. James and De Gennes $r_{GL} = 1.695$ and also exceeds the factors obtained from S. Casalbuoni et al. [115]. Note that, for the samples 67-u and 67-l which were cut from 67, the H_{c3} went below that of the untreated sample U, which might suggest that the treated surface was damaged during the cutting procedure. S. Casalbuoni et al. [115] found the ratios $r_{BCP} = 1.86 \pm 0.03$ for BCP and $r_{EP} = 2.1 \pm 0.03$ for EP samples. Our measurements do not confirm this observation as can be deduced from table 12. However, also the ratio $r = 3.6 \pm 0.18$ for sample 67-u far exceeds their values of which the highest value was 2.64 ± 0.05 observed for a sample that received a BCP, a 40 μm EP and 48h baking at 123°C.
Two of the samples underwent a nitrogen infusion together with a cavity. However, the nitrogen infusion was not successful so that the cavity performance did not improve. Furthermore, carbides were observed on the sample surfaces as was discussed in sec. 7.2.
It is suggested in [115] that the increased proportionality factor $r > r_{GL}$ is to be combined with an increased H_{c2} to the surface so that $H_{c2}^{surf} > H_{c2}^{bulk}$ and H_{c3} is related as $H_{c3} = r_{GL} H_{c2}^{surf}$. This increase might be related due to a reduction in the coherence length due to a higher concentration of impurities at the surface.
Since our measured bulk nucleation field H_{c2} is higher than [115] which was $H_{c2}(0) = (410 \pm 5)$ mT, one would expect a higher H_{c3} as well. It can be assumed that our starting material has a higher critical field, since even that of the untreated sample exceeds all of

the values from [115]. The impurity levels listed in table 10 given by the manufacturer from the leftover European XFEL production sheet from which the samples were cut have significantly lower limit values than given for the sheets used for the samples in [115]. Therefore, a significantly purer material can be assumed for our samples. It is possible, therefore, that the higher bulk critical field H_{c2} can be attributed to the purer starting material. Hence, it can be hypothesized that the surface superconductivity is also affected and thus the ratio factor.

A model by Shmidt [120] based on the Ginzburg-Landau theory assumes that there are impurities in a surface layer of thickness d smaller than the coherence length of the superconductor so that $d < \xi$. According to this model, the proportionality factor $r = 1.67(1 + (1 - \chi(\xi_0/l)\sqrt{1.7}d/\xi(T))$, with the two unknowns l (mean free path length) and d (layer thickness of the impurities) and the Gor'kov function [121] $\chi(\xi_0/l) = \kappa/\kappa_{surf}$ which relates the ratio of the GL parameters of the bulk and the surface. Since $(1 - \chi(\xi_0/l)) \leq 1$ and $d/\xi \leq 1$, the proportionality factor has a maximum of $r_{max} = 3.8$. Hence our result is still consistent with this model.

9 Summary

In this thesis, several investigations related to the nitrogen-infusion phenomenon have been examined. The goal has been to find approaches to understand nitrogen infusion and to make it reproducible. Hence a reproducible recipe for a successful infusion treatment had to be found and the key parameters had to be identified. All this research has been based on material sample studies.
An existing ceramic sample furnace has been improved accordingly in the scope of this work and new equipment has been provided and installed to meet the demanding requirements of successful nitrogen infusion. The final pressure of the sample furnace could be extremely reduced and almost reached the minimum possible using the existing equipment. A residual gas analysis showed hardly any remaining contamination. The oven has then mainly been used for sample treatments for the experiments of this research.
The first aim of the research was to examine correlations between the nitrogen infusion temperature and the RRR of niobium samples. The alternating field approach, which measures variations in the induced magnetic field, was utilized on a SRF cavity. The cavity was measured before and after an Infusion treatment with nitrogen injection at 120°C and showed a deterioration in RRR. This result could be confirmed by a 4-pt measurement on samples. One goal of the RRR investigation was to examine the effect of temperature between 120°C and 400°C on nitrogen infusion on samples. Another goal was to distinguish from diffusion mechanisms that involved nitrogen to those that involved other residual gases from inside the oven. Therefore, treatments were also carried out at the same temperatures without nitrogen, i.e. in a vacuum. A deterioration of RRR for all treated samples has been found, whether or not nitrogen was used. The difference in RRR between before and after treatment does not increase beyond a certain threshold temperature. This observation contradicts the expectation that, ΔRRR increases with temperature as the higher the temperature, the more nitrogen atoms are absorbed in the lattice, which although it cannot be ruled out, is disfavoured by the data. This, together with the additional comparison to vacuum-treated samples, leads to the conclusion that other processes take place in addition to the diffusion of nitrogen. It also means that no further residual gases have been absorbed by the sample beyond the threshold temperature. It had previously been suspected that the surface oxide reduces upon heating so that oxygen can diffuse into the bulk [104] [105]. The oxygen redistribution could have made a important impact on the RRR observations. It should be noted that fine-grain material has been used, which means that a lot of grain boundaries exist on the samples. The diffusion of nitrogen at grain boundaries has not yet been investigated extensively for pure niobium. Finally, it can be said that the bulk RRR value of samples infused with nitrogen is more reduced compared to those without nitrogen infusion but subjected to the same temperature treatment. However, the difference in ΔRRR between treated with and without nitrogen does not increase beyond the threshold temperature. For the samples treated with nitrogen, although there is a tendency for ΔRRR to decrease with temperature after the threshold temperature, the data are insufficiently precise to establish this. This is difficult to understand if only nitrogen diffusion played a part, as the addition of nitrogen to the lattice must decrease RRR and hence increase ΔRRR.
The next section of this thesis focuses on a different measurement method. Secondary ion mass spectrometry (SIMS) is the standard method to resolve the actual components of a

sample surface in the first few nanometers. Unfortunately, measuring the nitrogen content of niobium samples is difficult using SIMS. Nonetheless, incorporation of nitrogen in niobium after the nitrogen infusion has been reported by SIMS measurements. The first SIMS measurement reported in this thesis of a fine-grain sample infused at 180°C showed no nitrogen signal at all. The 400°C Infusion could more likely produce a signal, in case enough interstitial nitrogen diffused into the material and not much nitride crystallisation took place on the surface. To investigate the effect of grain boundaries, a large-grain and a fine-grain sample were treated at 400°C. In the large-grain sample, no nitrogen was detected while a weak signal was detected for the fine-grain sample. It appears therefore that grain boundaries favour diffusion.
The next section of the presented work deals with the formation of carbides on cavity and sample surfaces. Results of attempted nitrogen infusions in cavities at DESY are presented. The usage of line-of-sight protection led to the discovery that carbides were formed which was traced to the insufficient cleanliness of the line-of-sight boxes and caps. These carbides led to cavity-performance deterioration. A successful approach to avoid carbides has been made with the help of the sample furnace. It could be proven that it helps to anneal the line-of-sight protection at 1000°C beforehand. This fact has been confirmed several times on samples. The overall conclusion is that cleanliness of all components in the process is essential if infusion is ever to be understood.
In the last part of this study, measurements of the bulk property H_{c2} on niobium samples by "four-terminal sensing" are presented. Utilizing a superconducting quantum interference device (SQUID), the surface nucleation field H_{c3} on samples has been measured. The measured H_{c3} values of the niobium samples are very high compared to previously reported results. This could be due to the purer starting material, which also shows higher bulk H_{c2} values than previously reported. Unfortunately, the accuracy of the measurement is not sufficient to determine differences in surface treatments such as nitrogen infusions with different parameters. Until now, results on H_{c3} have not been reported in much detail in association with the nitrogen-infusion treatment. Since the measurement of H_{c3} is surface-sensitive and particularly interesting for the relation to RF properties of cavities, it is a suitable method for further research dealing with nitrogen treatments of samples.
In order to be able to understand the complete mechanism of nitrogen infusion, it is necessary to reproduce the recipe in a stable manner. This goal could not be realized for cavities at DESY. However, in the scope of this thesis, a sample furnace vacuum could be technically improved to such an extent that the purity is sufficient to do nitrogen infusion without contaminating the sample with carbon which gives the necessary preconditions for successful infusion of cavities. The failure of nitrogen infusion on cavities at DESY is related to carbide contamination. The conditions under which carbides are formed have been investigated in connection with line-of-sight protection. Furthermore, approaches have been developed on how to carry out the nitrogen infusion in cavities with line-of-sight protection. SQUID measurements have been investigated on various niobium samples. The niobium material, provided by manufacturers who have been also used for European XFEL cavities, showed particularly high values for H_{c3}. The sample furnace is available for further experiments on nitrogen infusion and similar cavity-surface processes, which could be fruitful in the future. The most important message of this thesis is that cleanliness is the essential prerequisite for all experimentation in these areas.

References

[1] H. Padamsee, J. Knobloch, and T. Hays. *RF Superconductivity for Accelerators*. Wiley Series in Beam Physics and Accelerator Technology. Wiley, 1998. 9, 13, 15, 28, 43, 46

[2] Ties Behnke, James E. Brau, Brian Foster, Juan Fuster, Mike Harrison, James McEwan Paterson, Michael Peskin, Marcel Stanitzki, Nicholas Walker, and Hitoshi Yamamoto. The International Linear Collider Technical Design Report - Volume 1: Executive Summary. 2013. See also http://www.linearcollider.org/ILC/TDR . The full list of contributing institutes is inside the Report. 9

[3] XFEL: The European X-Ray Free-Electron Laser. Technical design report. 7 2006. 9

[4] The International Linear Collider Technical Design Report - Volume 3.II: Accelerator Baseline Design. 6 2013. 9

[5] A Grassellino, A Romanenko, Y Trenikhina, M Checchin, M Martinello, O S Melnychuk, S Chandrasekaran, D A Sergatskov, S Posen, A C Crawford, S Aderhold, and D Bice. Unprecedented quality factors at accelerating gradients up to 45 MVm-1 in niobium superconducting resonators via low temperature nitrogen infusion. *Superconductor Science and Technology*, 30(9):094004, aug 2017. 9, 41, 42, 69, 70, 75

[6] Hasan Padamsee. Future prospects of superconducting rf for accelerator applications. *Reviews of Accelerator Science and Technology*, 10(01):125–156, 2019. 9

[7] D. Reschke, V. Gubarev, J. Schaffran, L. Steder, N. Walker, M. Wenskat, and L. Monaco. Performance in the vertical test of the 832 nine-cell 1.3 ghz cavities for the european x-ray free electron laser. *Phys. Rev. Accel. Beams*, 20:042004, Apr 2017. 9

[8] M. Wenskat, D. Bafia, A. Grassellino, O.S. Melnychuk, A.D. Palczewski, D. Reschke, J. Schaffran, L. Steder, and M. Wiencek. A Cross-Lab Qualification of Modified 120C Baked Cavities. In *Proc. SRF'19*, number 19 in International Conference on RF Superconductivity, pages 90–94. JACoW Publishing, Geneva, Switzerland, aug 2019. 9

[9] G. Ising. *Prinzip einer Methode zur Herstellung von Kanalstrahlen hoher Voltzahl*. Arkiv för Matematik, Astronomi och Fysik. Almqvist & Wiksells Boktryckeri-A.B., 1924. 10

[10] Rolf Wideröe. Über ein neues prinzip zur herstellung hoher spannungen. *Archiv für Elektrotechnik*, 21(4):387–406, Jul 1928. 10

[11] Frank Gerigk. Cavity types. *CAS 2010 - CERN Accelerator School: RF for Accelerators, Proceedings*, 11 2011. 10, 11

[12] K. Blasche and H. Prange. Die gsi in darmstadt (i): Ein laboratorium für die schwerionenforschung. *Physikalische Blätter*, 33(6):249–261, 1977. 10

[13] Frank Hinterberger. *Physik der Teilchenbeschleuniger und Ionenoptik*, volume 2. Springer, 2008. p. 40. 10

[14] Luis W Alvarez. The design of a proton linear accelerator. In *Physical review*, volume 70, pages 799–800. AMERICAN PHYSICAL SOC ONE PHYSICS ELLIPSE, COLLEGE PK, MD 20740-3844 USA, 1946. 10

[15] M. Pekeler. *Untersuchungen der feldbegrenzenden Mechanismen in supraleitenden Niob-Resonatoren*. PhD thesis, Universität Hamburg, 1996. 12

[16] A.A. Abrikosov. *Fundamentals of the Theory of Metals*. Fundamentals of the Theory of Metals. North-Holland, 1988. 12

[17] A P Banford and G H Stafford. The feasibility of a superconducting proton linear accelerator. *Journal of Nuclear Energy. Part C, Plasma Physics, Accelerators, Thermonuclear Research*, 3(4):287, 1961. 12

[18] J. K. Sekutowicz. Superconducting elliptical cavities. In *CERN Accelerator School: Course on RF for Accelerators*, 1 2012. 13

[19] H Kamerlingh Onnes. research notebooks 56, 57. *Kamerlingh Onnes Archive, Boerhaave Museum, Leiden, the Netherlands*, 1911. 15

[20] W. Meissner and R. Ochsenfeld. Ein neuer effekt bei eintritt der supraleitfähigkeit. *Naturwissenschaften*, 21:787–788, 01 1933. 15

[21] F. London, H. London, and Frederick Alexander Lindemann. The electromagnetic equations of the supraconductor. *Proceedings of the Royal Society of London. Series A - Mathematical and Physical Sciences*, 149(866):71–88, 1935. 15, 16

[22] M. Tinkham. *Introduction to Superconductivity*. Dover Books on Physics Series. Dover Publications, 2004. 15, 18, 19, 20, 24, 39

[23] Alfred Brian Pippard and William Lawrence Bragg. An experimental and theoretical study of the relation between magnetic field and current in a superconductor. *Proceedings of the Royal Society of London. Series A. Mathematical and Physical Sciences*, 216(1127):547–568, 1953. 15

[24] Leon N. Cooper. Bound electron pairs in a degenerate fermi gas. *Phys. Rev.*, 104:1189–1190, Nov 1956. 16

[25] H. Fröhlich. Theory of the superconducting state. i. the ground state at the absolute zero of temperature. *Phys. Rev.*, 79:845–856, Sep 1950. 16

[26] C. A. Reynolds, B. Serin, W. H. Wright, and L. B. Nesbitt. Superconductivity of isotopes of mercury. *Phys. Rev.*, 78:487–487, May 1950. 16

[27] Emanuel Maxwell. Isotope effect in the superconductivity of mercury. *Phys. Rev.*, 78:477–477, May 1950. 16

[28] J. Bardeen, L. N. Cooper, and J. R. Schrieffer. Theory of superconductivity. *Phys. Rev.*, 108:1175–1204, Dec 1957. 16

[29] D. C. Mattis and J. Bardeen. Theory of the anomalous skin effect in normal and superconducting metals. *Phys. Rev.*, 111:412–417, Jul 1958. 16

[30] VL Ginzburg and LD Landau. Phenomenological theory. *J. Exp. Theor. Phys. USSR*, 20:1064, 1950. 17

[31] A. A. Abrikosov. On the Magnetic properties of superconductors of the second group. *Sov. Phys. JETP*, 5:1174–1182, 1957. [Zh. Eksp. Teor. Fiz.32,1442(1957)]. 17

[32] Irwin Yousept. Optimal control of non-smooth hyperbolic evolution maxwell equations in type-ii superconductivity. *SIAM Journal on Control and Optimization*, 55:2305–2332, 01 2017. 17

[33] Lev Petrovich Gor'kov. Microscopic derivation of the ginzburg-landau equations in the theory of superconductivity. *Sov. Phys. JETP*, 9(6):1364–1367, 1959. 18

[34] B. Aune, R. Bandelmann, et al. Superconducting tesla cavities. *Phys. Rev. ST Accel. Beams*, 3:092001, Sep 2000. 18, 43

[35] N. R. A. Valles and M. U. Liepe. Temperature dependence of the superheating field in niobium, 2010. 18

[36] Nicholas Walker, Laura Monaco, Detlef Reschke, Joern Schaffran, Lea Steder, and Marc Wenskat. Performance Analysis of the European XFEL SRF Cavities, From Vertical Test to Operation in Modules. In *28th International Linear Accelerator Conference*, 5 2017. 18

[37] D. Reschke, S. Aderhold, A. Gössel, J. Iversen, S. Karstensen, D. Kostin, G. Kreps, A. Matheisen, W.-D. Möller, F. Schlander, W. Singer, X. Singer, N. Steinhau-Kühl, A. Sulimov, K. Twarowski, and DESY. Update on Large Grain Cavities with 45 MV/m in a Nine-Cell Cavity at DESY. *TESLA Report*, 2011. 18

[38] Daniel Saint-James and PG de Gennes. Onset of superconductivity in decreasing fields. *Phys. Letters*, 7, 1963. 19, 100, 112

[39] P.G. de Gennes. Vortex nucleation in type ii superconductors. *Solid State Communications*, 3(6):127 – 130, 1965. 19, 100

[40] K. Saito. Basic principles of srf. In Proceedings of SRF2005, page Tutorial at the SRF Workshop 2005. KEK, 2005., 2005. 21

[41] Sarah Aull, Tobias Junginger, Jens Knobloch, and Holger Neupert. Secondary electron yield of SRF materials. In *Proceedings, 17th International Conference on RF Superconductivity (SRF2015): Whistler, Canada, September 13-18, 2015*, page TUPB050, 2015. 22, 23

[42] Alexander Wu Chao and Maury Tigner. *Handbook of Accelerator Physics and Engineering*. World Scientific, Singapore, 1999. 22

[43] U Klein and D Proch. Multipacting in superconducting rf structures. In *Proceedings of the Conference of Future Possibilities for Electron Accelerators, Charlottesville, WU B*, pages 78–34, 1979. 23

[44] B. Bonin and R. W. Roth. Q degradation of niobbium cavities due to hydrogen contamination. *Part. Accel.*, 40:59–83, 1992. 23

[45] J. Knobloch. The "q disease" in superconducting niobium rf cavities. *AIP Conference Proceedings*, 671(1):133–150, 2003. 23, 25

[46] C. Z. Antoine and S. Berry. H in niobium: Origin and method of detection. *AIP Conference Proceedings*, 671(1):176–189, 2003. 23

[47] A Romanenko, F Barkov, L D Cooley, and A Grassellino. Proximity breakdown of hydrides in superconducting niobium cavities. *Superconductor Science and Technology*, 26(3):035003, jan 2013. 24

[48] G. Ciovati, G. Myneni, F. Stevie, P. Maheshwari, and D. Griffis. High field Q slope and the baking effect: Review of recent experimental results and new data on Nb heat treatments. *Phys. Rev. ST Accel. Beams*, 13:022002, 2010. 24, 68, 69, 70

[49] H. Padamsee. Influence of thermal conductivity on the breakdown field of niobium cavities. *IEEE Transactions on Magnetics*, 21(2):149–152, 1985. 25

[50] H. Safa. An analytical approach for calculating the quench field in superconducting cavities. Technical report, France, 1996. CEA-DAPNIA-SEA–96-05. 25

[51] R.W. Cahn and P. Haasen. *Physical Metallurgy*. Number Bd. 1 in Physical Metallurgy. Elsevier Science, 1996. 25

[52] W. Singer, A. Ermakov, and X. Singer. RRR-Measurement Techniques on High Purity Niobium. *TTC*, 2010. 25, 47, 48, 49, 59

[53] Klaus Schulze. Preparation and characterization of ultra-high-purity niobium. *Journal of Metals*, 33:33–41, 05 1981. 25, 28

[54] M Peiniger, M Hein, N Klein, G Müller, H Piel, and P Thuns. Proceedings of the third workshop on rf superconductivity. 1988. 26

[55] Wolfgang Weingarten. Field-dependent surface resistance for superconducting niobium accelerating cavities. *Phys. Rev. ST Accel. Beams*, 14:101002, Oct 2011. 26

[56] Gianluigi Ciovati, Pashupati Dhakal, Peter Kneisel, and Ganapati R. Myneni. Summary of performance of superconducting radio-frequency cavities built from cbmm niobium ingots. *AIP Conference Proceedings*, 1687(1):030001, 2015. 26

[57] A. R. Jana, V. Kumar, A. Kumar, and R. Gaur. Electromagnetic design of a $\beta_g = 0.9$ 650-mhz superconducting-radio-frequency cavity. *IEEE Transactions on Applied Superconductivity*, 23(4):3500816–3500816, 2013. 26

[58] Arup Ratan Jana, Abhay Kumar, Vinit Kumar, and Sindhunil Barman Roy. Influence of material parameters on the performance of niobium-based superconducting radiofrequency cavities. *Pramana*, 93(3):51, Jul 2019. 27

[59] W Singer. SRF Cavity Fabrication and Materials. pages 171–207. 37 p, Jan 2015. Comments: 37 pages, contribution to the CAS-CERN Accelerator School: Superconductivity for Accelerators, Erice, Italy, 24 April - 4 May 2013, edited by R. Bailey. 28

[60] W. Singer, S. Aderhold, A. Ermakov, J. Iversen, D. Kostin, G. Kreps, A. Matheisen, W.-D. Möller, D. Reschke, X. Singer, K. Twarowski, H. Weise, and H.-G. Brokmeier. Development of large grain cavities. *Phys. Rev. ST Accel. Beams*, 16:012003, Jan 2013. 28

[61] *XFEL: The European X-Ray Free-Electron Laser - Technical Design Report*. DESY, Hamburg, 2006. 28, 29

[62] B. van der Horst, A. Matheisen, B. Petersen, M. Schmoekel, N. Steinhau-Kuehl, and H. Weitkaemper. Experiences on improved cavity preparation cycles with a vision on industrialization of the xfel cavity preparation. In *Proc. 14th Int. Conf. RF Superconductivity (SRF'09)*, pages 791–793. JACoW Publishing, Sep. 2009. 28

[63] P. Kneisel, Gianluigi Ciovati, Pashupati Dhakal, K. Saito, W. Singer, X. Singer, and Ganapati Myneni. The rise of ingot niobium as a material for superconducting radiofrequency accelerating cavities. *Nuclear Instruments and Methods in Physics Research Section A Accelerators Spectrometers Detectors and Associated Equipment*, 774, 04 2013. 28

[64] W. Singer, A. Brinkmann, R. Brinkmann, J. Iversen, A. Matheisen, W.-D Moeller, A. Navitski, Detlef Reschke, Jörn Schaffran, A. Sulimov, N. Walker, Hans Weise, Paolo Michelato, L. Monaco, C. Pagani, and M. Wiencek. Production of superconducting 1.3-ghz cavities for the european x-ray free electron laser. *Physical Review Accelerators and Beams*, 19, 09 2016. 28

[65] W. Singer, A. Brinkmann, D. Proch, and X. Singer. Quality requirements and control of high purity niobium for superconducting rf cavities. *Physica C: Superconductivity*, 386:379–384, 04 2003. 28

[66] L. Lilje, C. Antoine, C. Benvenuti, D. Bloess, J.-P. Charrier, E. Chiaveri, L. Ferreira, R. Losito, A. Matheisen, H. Preis, D. Proch, D. Reschke, H. Safa, P. Schmüser, D. Trines, B. Visentin, and H. Wenninger. Improved surface treatment of the superconducting tesla cavities. *Nuclear Instruments and Methods in Physics Research Section A: Accelerators, Spectrometers, Detectors and Associated Equipment*, 516(2):213–227, 2004. 29, 30

[67] J Guerin. Etude du bain de polissage chimique de niobium. Technical report, Technical Report TE/LC/157/89, CERN, 1989. 29

[68] B Hillenbrand, N Krause, K Schmitzke, and Y Uzel. Abschlussbericht-supraleitende resonatoren. Technical report, Technical Report NT 2024 7, Siemens AG, 1982. 29

[69] R Röth. *Untersuchungen zu anomalen Verlusten in Niobresonatoren*. PhD thesis, 1993. 29

[70] W. C. Elmore. Electrolytic polishing. *Journal of Applied Physics*, 10(10):724–727, 1939. 29

[71] W. C. Elmore. Electrolytic polishing. ii. *Journal of Applied Physics*, 11(12):797–799, 1940. 29

[72] M P Kelly and T Reid. Surface processing for bulk niobium superconducting radio frequency cavities. *Superconductor Science and Technology*, 30(4):043001, feb 2017. 30

[73] K. Saito, H. Inoue, E. Kako, T. Fujino, S. Noguchi, M. Ono, and T. Shishido. Superiority of electropolishing over chemical polishing on high gradients. 1998. 30

[74] Detlef Reschke, Lutz Lilje, and Hans Weise. Analysis of RF results of recent Nine-Cell cavities at DESY. Technical Report TTC-Report 2009-01, 2009. 31

[75] M Schalwat, K Escherich, N Krupka, A Matheisen, Brigitte Petersen, A Schmidt, and N Kuehl. Update of the desy infrastructure for cavity preparation. In *TUPO018*, pages 401–404, Chicago, IL, USA, 7 2011. Proc. 15th Int. Conf. RF Superconductivity (SRF'11). 32

[76] A Grassellino, A Romanenko, D Sergatskov, O Melnychuk, Y Trenikhina, A Crawford, A Rowe, M Wong, T Khabiboulline, and F Barkov. Nitrogen and argon doping of niobium for superconducting radio frequency cavities: a pathway to highly efficient accelerating structures. *Superconductor Science and Technology*, 26(10):102001, aug 2013. 39

[77] J Stohr. Linac coherent light source ii (lcls-ii) conceptual design report. Technical report, SLAC National Accelerator Laboratory (United States). Funding organisation, 2011. 39

[78] A. Romanenko, A. Grassellino, O. Melnychuk, and D. A. Sergatskov. Dependence of the residual surface resistance of superconducting radio frequency cavities on the cooling dynamics around tc. *Journal of Applied Physics*, 115(18):184903, 2014. 40

[79] B. Scheerer. Preparation of nbn single crystals. *Journal of Crystal Growth*, 49(1):61 – 66, 1980. 40

[80] Yulia Trenikhina, Anna Grassellino, Oleksandr Melnychuk, and Alexander Romanenko. Characterization of Nitrogen Doping Recipes for the Nb SRF Cavities. In *17th International Conference on RF Superconductivity*, 12 2015. 41, 93

[81] A Grasselino. New insights on the physics of rf surface resistance and a cure for the medium field q-slope. In *TUIOA03*, Paris, France, 2013. 16th International Conference on RF Superconductivity. 41

[82] Pashupati Dhakal, Santosh Chetri, Shreyas Balachandran, Peter J. Lee, and Gianluigi Ciovati. Effect of low temperature baking in nitrogen on the performance of a niobium superconducting radio frequency cavity. *Phys. Rev. Accel. Beams*, 21:032001, Mar 2018. 42, 67, 69, 75

[83] PN Koufalis, F Furuta, M Ge, D Gonnella, JJ Kaufman, M Liepe, JT Maniscalco, and R Porter. Low temperature nitrogen baking of an srf cavity. *Proceedings of LINAC2016, East Lansing, MI*, 2016. 42, 67

[84] Kensei Umemori, Eiji Kako, Taro Konomi, Shinichiro Michizono, H Sakai, J Tamura, and T Okada. Study on nitrogen infusion using kek new furnace. In *Proceedings of the International Conference on RF Superconductivity SRF*, 2019. 42

[85] Marc Wenskat, Christopher Bate, Arti Dangwal Pandey, Arno Jeromin, Thomas F Keller, Jens Knobloch, Julia Köszegi, Felix Kramer, Oliver Kugeler, Satish Kulkarni, Detlef Reschke, Jörn Schaffran, Guilherme Dalla Lana Semione, Sven Sievers, Lea Steder, Andreas Stierle, and Nicholas Walker. Nitrogen infusion r&d at DESY a case study on cavity cut-outs. *Superconductor Science and Technology*, 33(11):115017, oct 2020. 42, 93

[86] B. W. Maxfield and W. L. McLean. Superconducting penetration depth of niobium. *Phys. Rev.*, 139:A1515–A1522, Aug 1965. 43

[87] Marc Wenskat. Automated Optical Inspection and Image Analysis of Superconducting Radio-Frequency Cavities. *JINST*, 12(05):P05016, 2017. 43

[88] Helmut Mehrer. *Diffusion in Solids. Fundamentals, Methods, Materials, Diffusion-Controlled Processes.* Springer, Berlin, Heidelberg, 2007. 44

[89] Adolf Fick. Ueber diffusion. *Annalen der Physik*, 170(1):59–86, 1855. 44

[90] Runzhe Tao, Ruzica Todorovic, Jingjing Liu, Randall J. Meyer, Andrew Arnold, Weronika Walkosz, Peter Zapol, Alexander Romanenko, Lance D. Cooley, and Robert F. Klie. Electron energy-loss spectroscopy study of metallic nb and nb oxides. *Journal of Applied Physics*, 110(12):124313, 2011. 44

[91] A. Joshi and Myron Strongin. Surface segregation of oxygen in nb-o and ta-o alloys. *Scripta Metallurgica*, 8(4):413–424, 1974. 45

[92] I. Arfaoui, J. Cousty, and H. Safa. Tiling of a nb(110) surface with nbo crystals nanosized by the nbo/nb misfit. *Phys. Rev. B*, 65:115413, Mar 2002. 45

[93] Z.P. Hu, Y.P. Li, M.R. Ji, and J.X. Wu. The interaction of oxygen with niobium studied by xps and ups. *Solid State Communications*, 71(10):849–852, 1989. 45

[94] M. Delheusy. *X-ray investigation of Nb/O interfaces.* PhD thesis, Univ. Paris-Sud XI UFR Scientifique d'Orsay und an der Univ. Stuttgart Fakultät Mathematik und Physik, France, Jul 2008. 45

[95] G. D. L. Semione, A. Dangwal Pandey, S. Tober, J. Pfrommer, A. Poulain, J. Drnec, G. Schütz, T. F. Keller, H. Noei, V. Vonk, B. Foster, and A. Stierle. Niobium near-surface composition during nitrogen infusion relevant for superconducting radio-frequency cavities. *Phys. Rev. Accel. Beams*, 22:103102, Oct 2019. 45, 60, 64, 75

[96] A. Daccà, G. Gemme, L. Mattera, and R. Parodi. Xps analysis of the surface composition of niobium for superconducting rf cavities. *Applied Surface Science*, 126(3):219–230, 1998. 45

[97] B.R. King, H.C. Patel, D.A. Gulino, and B.J. Tatarchuk. Kinetic measurements of oxygen dissolution into niobium substrates: In situ x-ray photoelectron spectroscopy studies. *Thin Solid Films*, 192(2):351–369, 1990. 45

[98] Qing Ma, P. Ryan, J. W. Freeland, and R. A. Rosenberg. Thermal effect on the oxides on nb(100) studied by synchrotron-radiation x-ray photoelectron spectroscopy. *Journal of Applied Physics*, 96(12):7675–7680, 2004. 45

[99] O. Hellwig and H. Zabel. Oxidation of nb(110) thin films on a-plane sapphire substrates: an x-ray study. *Physica B: Condensed Matter*, 283(1):228–231, 2000. 45

[100] W. Singer, A. Brinkmann, A. Ermakov, J. Iversen, G. Kreps, A. Matheisen, D. Proch, D. Reschke, X. Singer, M. Spiwek, H. Wen, P. Kneisel, and M. Pekeler. Advances in large grain/single crystal sc resonators at desy. In *2007 IEEE Particle Accelerator Conference (PAC)*, pages 2569–2571, 2007. 46

[101] Felix Schlander. *Study of Quality and Field Limitation of Superconducting 1.3 GHz 9-Cell RF-Cavities at DESY*. PhD thesis, Hamburg U., Hamburg, 2012. 46

[102] Shuji Hasegawa, Ichiro Shiraki, Takehiro Tanikawa, Chris Petersen, Torben Hansen, Peter Bøggild, and Francois Grey. Direct measurement of surface-state conductance by microscopic four-point probe method. *Journal of Physics: Condensed Matter*, 14:8379, 08 2002. 58

[103] H. M. Wen, W. Singer, and D. Proch. Some results about RRR distribution in Nb of superconducting cavities for the TESLA test facility. 2 1998. 61

[104] Gianluigi Ciovati. Improved oxygen diffusion model to explain the effect of low-temperature baking on high field losses in niobium superconducting cavities. *Applied Physics Letters*, 89(2):022507, 2006. 64, 67, 114

[105] Sergio Calatroni, Cristoforo Benvenuti, and V Ruzinov. Diffusion of oxygen in niobium during bake-out. page 3 p, Jul 2002. 64, 114

[106] Gianluigi Ciovati. Effect of low-temperature baking on the radio-frequency properties of niobium superconducting cavities for particle accelerators. *Journal of Applied Physics*, 96(3):1591–1600, 2004. 67

[107] PB Wilson. Slac technical note no. Technical report, SLAC-TN-71-7, 1971. 69

[108] Ki Hyun Kim, Zentaro Akase, Toshiaki Suzuki, and Daisuke Shindo. Charging effects on sem/sim contrast of metal/insulator system in various metallic coating conditions. *MATERIALS TRANSACTIONS*, 51(6):1080–1083, 2010. 71

[109] A. Grassellino et al. Fermilab experience of post-annealing losses in SRF niobium cavities due to furnace contamination and the ways to its mitigation: a pathway to processing simplification and quality factor improvement. 2013. 76, 77, 87

[110] Mattia Checchin, Anna Grassellino, Martina Martinello, Oleksandr Melnychuk, Sam Posen, Alexander Romanenko, and Dmitri Sergatskov. New Insight on Nitrogen Infusion Revealed by Successive Nanometric Material Removal. In *9th International Particle Accelerator Conference*, 6 2018. 76

[111] A. Dangwal Pandey, T. F. Keller, M. Wenskat, A. Jeromin, S. Kulkarni, H. Noei, V. Vonk, W. Hillert, D. Reschke, N. Walker, H. Weise, and A. Stierle. Grain boundary segregation and carbide precipitation in heat treated niobium superconducting radio frequency cavities. *Applied Physics Letters*, 119(19):194102, 2021. 79, 94, 99

[112] A Vladar and M Postek. Electron beam-induced sample contamination in the sem. *Microscopy and Microanalysis*, 11(S02):764–765, 2005. 85

[113] Arti Dangwal Pandey. Grain boundary segregation and precipitation of carbides in heat treated nb. TTC 2021 TESLA Technology Collaboration Virtual Meeting, 2021. 94

[114] Denise C. Ford, Peter Zapol, and Lance D. Cooley. First-principles study of carbon and vacancy structures in niobium. *The Journal of Physical Chemistry C*, 119(26):14728–14736, 2015. 94

[115] S. Casalbuoni, E.A. Knabbe, J. Kötzler, L. Lilje, L. von Sawilski, P. Schmüser, and B. Steffen. Surface superconductivity in niobium for superconducting rf cavities. *Nuclear Instruments and Methods in Physics Research Section A: Accelerators, Spectrometers, Detectors and Associated Equipment*, 538(1):45 – 64, 2005. 100, 106, 107, 112, 113

[116] Pashupati Dhakal. Nitrogen doping and infusion in srf cavities: A review. *Physics Open*, 5:100034, 2020. 100

[117] Florian Semper. Messung des oberen kritischen magnetfelds von oberflächenbehandeltem niob. Master's thesis, TU Wien, Wien, 2020. 100, 102, 104, 105, 110

[118] S. Murase, K. Itoh, H. Wada, K. Noto, Y. Kimura, Y. Tanaka, and K. Osamura. Critical temperature measurement method of composite superconductors. *Physica C: Superconductivity*, 357-360:1197 – 1200, 2001. 103

[119] J. R. Hopkins and D. K. Finnemore. Surface superconductivity in niobium and niobium-tantalum alloys. *Phys. Rev. B*, 9:108–114, Jan 1974. 106

[120] V. Shmidt. Third critical field of a superconductor with a film on the surface. 1970. 113

[121] Lev Petrovich Gor'kov. Theory of superconducting alloys in a strong magnetic field near the critical temperature. *Soviet Physics JETP*, 10:998, 1960. 113

Acknowledgements

Die letzte Seite in diesem Manuskript widme ich all denen, die mir in den letzten Jahren zur Seite gestanden haben und ohne die ich niemals an diesem Punkt angelangt wäre.
Beginnen möchte ich mit meinem Doktorvater **Prof. Dr. Brian Foster**, dem ich dafür danken möchte, dass er mir jederzeit mit Ratschlägen sowie konstruktiver Kritik zur Seite stand. Dafür, dass er mir in der Zeit meiner Betreuung viele Freiheiten ermöglicht und sowohl Korrektur gelesen als auch bei meiner englischen Grammatik geholfen und trotz aller Strapazen an meine Fähigkeiten geglaubt und mich weiter ermutigt hat. Ich bedanke mich auch bei meinem Zweitgutachter **Dr. Hans Weise** für die anregenden und konstruktiven Gespräche sowie für das herzliche Willkommenheißen am Desy. Auch von **Dr. Marc Wenskat**, **Dr. Lea Steder** und **Jörn Schaffran** wurde ich in meinem ersten Jahr sehr herzlich aufgenommen und in die Gruppe integriert. Dafür, sowie für auch ihre Betreuung, ohne die ich nicht hier wäre, gebührt ihnen mein Dank. Besonderer Dank gilt desweiteren **Dr. Marc Wenskat**, der mich die ganze Zeit über mit Ideen, Diskussionen und natürlich auch Ablenkungen versorgt und in die Welt der SRF Technologie eingeführt hat. Insbesondere die Begeisterung für die Forschung hat mich immer wieder aufs neue fasziniert. Als nächstes möchte ich mich bei **Dr. Lea Steder** für die zusätzlichen Tipps und Anregungen bedanken sowie bei **Jörn Schaffran**, der mir überhaupt den Weg ins Labor eröffnet hat und von dem ich sehr viel Neues lernen konnte, ohne dieses Wissen wäre diese Arbeit nicht möglich gewesen.
Weiterer großer Dank gilt **Dr. Detlef Reschke**, der auch an vielen Stellen die Mitbetreuung übernommen hat und immer ein offenes Ohr für mich hatte sowie meinen Mentor **Dr. Nicholas John Walker**, der mich auf meine Ziele vorbereitet und bei der inhaltlichen Ausrichtung mitgewirkt hat.
Für seine experimentelle Hilfe bei den zahlreichen Stunden zusammen im Labor möchte ich mich besonders bei **Alexey Ermakov** bedanken. Auch **Nicolay Krupka**, der sich im Reinraum oftmals meiner angenommen hat, möchte ich meinen Dank aussprechen. Desweiteren gilt mein Dank **Dr. Sven Sievers**, **Nico Steinhau-Kühl**, **Marco Schalwat**, **Manuela Schmoekel** und **Birte van der Horst**. Würdigen möchte ich auch **Christian Hagedorn**, der meine vielen kleinen Aufträge für die Werkstatt angenommen hat, selbst wenn es mal schnell gehen musste, sowie **Daniel Klinke**, der mir bei sehr vielen Anfertigungen geholfen hat. Als nächstes würde ich gerne **Denis Kostin**, **Stefan Holm**, **Uwe Cornett**, **Andrea Muhs**, **Jürgen Eschke** und **Carsten Müller** samt Kollegen dankend erwähnen, welche mir bei Aufbauten, Fragen und Einrichtungen für Messungen zur Seite standen. Ein weiterer großer Dank gilt **Mario Lengkeit**, der mir oftmals bei Vakuum-Problemen geholfen, mir dadurch sehr viel beigebracht hat und ohne dessen Hilfe diese Arbeit weitaus länger gedauert hätte.
Bei den Kollegen bei Nanolab bedanke ich mich dafür, dass ich das SEM benutzen durfte und bei **Dr. Arti Dangwal Pandey** dafür, dass sie Messungen an meinen Proben durchgeführt, aber auch zu vielen wissenschaftlichen Diskussionen beigetragen hat. Vielen Dank auch an **Dr.-Ing. Thomas F. Keller** für viele weitere wissenschaftliche Anregungen und an **Prof. Dr. Wolfgang Hillert** für die vielen wissenschaftlichen Beratungen. Für all die produktiven Diskussionen und die Unterstützung beim "Doktoranden-Dasein" möchte ich mich bei meinen Kollegen **Dr. Guilherme Dalla Lana Semione**, **Bosse Kolja Bein**, **Ricardo Monroy-Villa**, **Isabel González Díaz-Palacio**, **Dr. Getnet Kacha Deyu**,

Rezvan Ghanbari und **Jonas Wolff** auch bedanken.
Zu guter letzt gilt großer Dank meinen Eltern, welche mich immer ermutigt haben, auch in schwierigen Zeiten weiter zu machen. Ich konnte mich immer auf sie verlassen und wusste, dass ich bei ihnen einen Rückzugsort hatte, wenn ich ihn brauchte. Daneben bedanke ich mich auch bei allen anderen, die ich hier nicht namentlich erwähnt habe, aber die mir ebenfalls geholfen haben. Die letzten Worte widme ich meiner Freundin Kathi, die mich immer unterstützt hat und trotz meiner vielen schlaflosen Nächten voller Kaffee und Wochenenden, an denen ich die Zeit in diese Arbeit gesteckt habe, an meiner Seite war.